Dissertation
submitted to the
Combined Faculties of the Natural Sciences and for Mathematics
of the Ruperto-Carola University of Heidelberg, Germany
for the degree of
Doctor of Natural Sciences

Presented by
Diplom-Physiker Timo Bastian Ottenstein
Born in Eberbach
Oral examination: February 3rd, 2010

Few-body physics in ultracold Fermi gases

Referees: **Juniorprofessor Dr. Selim Jochim**
Prof. Dr. Matthias Weidemüller

Abstract

This thesis reports on experimental studies of few-body physics in ultracold Fermi gases. The main part is devoted to the first realisation of an ultracold three-component Fermi gas in thermal equilibrium that consists of atoms in the three lowest spin states of ^{6}Li.

In first experiments the collisional stability of the gas was investigated in dependence of the interparticle interaction. The interaction strength was tuned by an external magnetic field employing Feshbach resonances in all three two-body scattering channels. At two magnetic field values a resonant enhancement of three-body loss was observed that can be explained by an Efimov-like trimer consisting of one atom in each of the three states which crosses the continuum twice in the studied magnetic field region. The behaviour of three-body loss rates could be understood by taking into account a variation of the lifetime of the trimer with the magnetic field.

These experiments were performed with large ensembles of atoms. A finite deeply degenerate Fermi gas consisting of a controlled number of atoms may serve as a clean model for finite Fermi systems as for example atomic nuclei. An approach for the preparation of such a gas is discussed and first experimental steps are presented.

Zusammenfassung

Diese Arbeit behandelt experimentelle Untersuchungen von Wenigteilchen-Phänomenen in ultrakalten Fermigasen. Der Schwerpunkt liegt auf der ersten Realisierung eines dreikomponentigen Fermigases im thermischen Gleichgewicht, welches aus ^{6}Li Atomen in den niedrigsten drei Zeeman Zuständen besteht.

Feshbach-Resonanzen erlaubten es, durch Anlegen eines äusseren Magnetfeldes die Stabilität des Gases in Abhängigkeit der Wechselwirkung zwischen den Atomen zu untersuchen. Für zwei Magnetfeldwerte wurde eine resonante Überhöhung des Dreikörperverlustes beobachtet, was durch einen universellen Trimerzustand erklärbar ist, der bei diesen Magnetfeldwerten das Kontinuum kreuzt. Ein komplettes Verständnis für den Verlauf der auftretenden Verlustraten konnte durch Berücksichtigung einer magnetfeldabhängigen Lebensdauer des Trimers gewonnen werden.

Diese Experimente wurden in grossen Ensembles ultrakalter Atome durchgeführt. Ein endliches Fermigas bestehend aus einer kontrollierbaren Anzahl von Atomen wäre ein ideales Modellsystem für endliche fermionische Systeme, wie zum Beispiel Atomkerne. Eine Methode zur Präparation eines solchen endlichen Fermi Gases wird vorgestellt und die ersten bereits durchgeführten Schritte präsentiert.

Contents

Chapter 1

Introduction

The fundamental constituents of known matter are particles with half-integer spin. These so-called fermions, for example quarks in nucleons or electrons in the shells of atoms, have to obey the Pauli principle that forbids two identical fermions to reside in the same quantum state. The ground state of a system consisting of several identical fermions in the absence of interactions at zero temperature is simple. Each state up to the so-called Fermi energy is occupied by exactly one particle while all states with higher energy are empty. This is a special case of the Fermi-Dirac distribution that describes the occupation probability of energy states in fermionic systems in terms of chemical potential and temperature.

Samples of ultracold Fermi gases provide a magnificent playground to study fermionic systems under well defined and controllable conditions. One of the most important properties of ultracold gases is that the interaction between the particles can be described by one single parameter, the so-called s-wave scattering length. Due to the low temperatures in the nanokelvin regime all scattering processes involving angular momentum are frozen out as the kinetic energy of the particles is too low to overcome the centrifugal barrier. Thus, the interparticle interaction is dominated by isotropic s-wave scattering. In a sample of identical fermions s-wave scattering is not possible due to symmetry reasons which means that interaction effects can only be studied in a mixture of at least two distinguishable fermions, for example two atoms of the same species but in different internal states. The strength of the interaction between these two components is then parametrized by the scattering length a which is related to the phase shift, the wavefunction of the particles acquires during the scattering process. This implies that the effects of the short-range details of the scattering potential are comprised in the scattering length and do not have to be precisely known. This is a manifestation of a general concept in physics which is called universality. It allows to express the consequences of complex short-range physics on macroscopic observables by a few universal parameters.

Moreover, in ultracold gas ensembles the s-wave scattering length has not a fixed value but can be tuned over a wide range by employing Feshbach resonances [Chi09]. These resonances allow to vary the interaction strength by applying an external magnetic field and are accessible for a variety of atomic species. In that respect, fermionic ^{6}Li is an exceptionally good choice for experiments with ultracold fermions, as broad Feshbach resonances occur in this system.

The first experimental breakthrough in the field of ultracold Fermi gases was made in the group of D. Jin [DeM99b] in 1999 by observing the onset of Fermi degeneracy in a sample of evaporatively cooled ^{40}K atoms in two different internal states. A degeneracy of $T/T_F \approx 0.5$ was reached before evaporative cooling became inefficient due to Pauli blocking.

Deeper degeneracies were achieved in 2001 by using an additional bosonic species as a cooling agent during evaporation. This sympathetic cooling technique allowed for the preparation of a degenerate Fermi gas on the order of $T/T_F \approx 0.2$ [Tru01, Roa02, Sch01, Had02].

While these experiments were performed in a magnetic trap, John Thomas and coworkers developed an all optical approach for evaporative cooling of ^{6}Li atoms and succeeded in preparing a degenerate Fermi gas of atoms in the two lowest Zeeman substates of ^{6}Li in 2002 [Gra02]. As this approach did not involve a magnetic trap it allowed for the use of an external magnetic field to tune the interaction by means of the Feshbach resonance that was predicted for this two-component mixture in 1998 by Houbiers et al. [Hou98]. This resulted in the preparation of a strongly interacting degenerate Fermi gas also in the group of John Thomas [O'H02a].

Depending on the sign of the scattering length the ground state of the system is fundamentally different. When the scattering length is tuned to large positive values a weakly bound dimer state exists that can be populated by collisions between the atoms. These dimers consist of two fermionic atoms forming a bosonic molecule. In 2003 three groups reached Bose-Einstein Condensation of these molecules [Joc03b, Gre03, Zwi03]. For negative scattering lengths no dimer state is present and the system is in a BCS like state, as it is known from the theoretical description of superconductors [Bar57]. The Feshbach resonance connects both regimes via a divergence of the scattering length which allows to study the so called BEC-BCS crossover [Bar04, Reg04b, Bou04] by adiabatically sweeping the magnetic field over the resonance. During this magnetic field sweep the molecules are smoothly transformed into weakly bound pairs which are similar to Cooper pairs in a superconductor. Indeed, experiments performing radio frequency spectroscopy were able to observe the so-called pairing gap in the crossover region [Chi04a] and to infer information about the size of the pairs [Sch08]. Pairing is a necessary condition for superfluidity whose occurrence in the resonance region was proven by the observation of vortices [Zwi05].

Experiments also studied imbalanced samples with an unequal atom number in both components. They observed a breakdown of superfluidity above a critical imbalance and a spatial separation of a superfluid core in the center of the trap and a surrounding cloud of unpaired atoms [Par06, Shi06, Shi08a, Shi08b]. In general, ultracold two-component Fermi gases offer a clean and easy accessible model system to study the emergence of superfluidity and may help to get a better understanding of resistanceless flow of electrons in solid state superconductors.

The experiments described so far worked with mixtures of fermionic atoms in two different internal states. When a third distinguishable component is added, the interaction properties of the system change fundamentally. In a two-component system only one scattering length is sufficient to describe the interaction, but in a mixture of three components three different scattering lengths in each of the three two-body scattering channels have to be taken into account. For the case of three equal scattering lengths the system has a SU(3) symmetry which reminds of color and flavour symmetry in high energy physics [Wil07].

An interesting question concerns the ground state of this system. Will two of the components pair while the other one remains as a spectator after a spontaneous breaking of the symmetry or is the ground state a phase of trimers consisting of one atom of each component? In the case of three unequal scattering lengths this symmetry is initially broken and pairing will depend on the relative strength of the two-body interactions. By varying the scattering lengths quantum phase transitions between different pairing channels should be observable [Paa06, Hon04, Sil09, Err09, Che07, Zha07, Bed09]. In this thesis the first steps towards the observation of these many-body phenomena are done by studying few-body physics in a three-component Fermi gas consisting of atoms in the three lowest Zeeman-substates of ^{6}Li. As already mentioned above, ^{6}Li is a good choice for these experiments as the two-body interaction between all three scattering channels can be tuned over a wide range by three wide and overlapping Feshbach resonances.

The physical phenomena discussed so far can be studied in large ensembles of ultracold fermions that can be described in the thermodynamic limit. In contrast to that, most fundamental Fermi systems in nature consist of a small number of fermions as for example atomic nuclei. For their description the interaction between single constituents has to be taken into account which is still a challenging task for current research. Thus, it would be intriguing to prepare a simple and easily accessible model system in the laboratory, where not only the particle number can be controlled but also the interaction between the constituents. We believe that the techniques developed for large ensembles of fermionic atoms allow for the preparation of a deeply degenerate Fermi gas consisting of a controlled number of ^{6}Li atoms in an optical dipole trap. The later chapters of this thesis are devoted to the experimental challenges that have to be overcome for the preparation of such

a system and report on our current experimental progress.

This thesis is organized as follows: Chapter 2 gives a brief introduction into the physics of ultracold Fermi gases in an optical dipole trap. After a discussion of the ideal Fermi gas, it is explained that s-wave scattering is the dominant interaction process in ultracold gases and how the interaction strength can be tuned by means of Feshbach resonances. In the last section of this chapter the concepts of universality and unitarity are discussed. Chapter 3 summarizes textbook results on the quantum mechanical three-body problem which are necessary to understand the experiments and their interpretation described in the later course of this thesis. Efimov's scenario which predicts an infinite number of bound states for resonant two-body interactions is discussed and important results on three-body recombination in ultracold gases is presented. Chapter 4 gives an overview of the experimental setup that was built during the first year of this PhD project and describes all experimental tools necessary for the preparation and manipulation of ultracold atoms. The construction phase ended with the first successful preparation of a Bose-Einstein condensate of $^6Li_2$ molecules which is described in chapter 5. The preparation of this BEC was an important milestone demonstrating that we have gained control over our experimental setup and that we were now ready for experiments. Chapter 6 is devoted to our experiments on three-component Fermi gases consisting of atoms in the three-lowest Zeeman substates of ^{6}Li. A short motivation depicts what encouraged us to work on this topic. Then our scheme for the preparation of the three-component sample and our first experiments studying the collisional stability of the gas in dependence of the interparticle interaction are described in detail. The interaction between the constituents was tuned by applying an external magnetic field and a resonant enhancement of atomic loss was observed at two field values. It turned out that the observed behaviour of three-body loss can be explained by the presence of an Efimov-like trimer state that crosses the free atom threshold at exactly these two field values. This chapter closes with a summary of predicted and in part already observed Efimov physics in the ^{6}Li system, including the magnetic field regions that were not studied in our experiments so far. Chapter 7 and 8 deal with our efforts for the preparation of a deeply degenerate Fermi gas consisting of a small and defined number of atoms. A couple of experimental challenges have to be overcome on the way towards such a system. Our approach involves a so-called microtrap that is established by a tightly focused laser beam. Due to the large trapping frequencies the energy separation of bound states in the trap is large enough to control the number of atoms by applying an additional magnetic field gradient. This gradient leads to a tilt of the trap and a controlled spilling of atoms. A simple estimation of the necessary experimental parameters based on the one dimensional WKB approximation is presented. Then the experimental progress of this project is reported. A microtrap using an off-the-shelf aspheric lens was implemented into our setup.

By applying an external magnetic field gradient we were able to spill atoms from the trap and prepare a sample of about 120 atoms with an uncertainty of 11 atoms. These atom numbers were determined using absorption imaging and may be affected by systematic errors. A better choice for the determination of small atom numbers is fluorescence imaging. In a benchmark experiment with single atoms in the MOT we demonstrated that we can detect single atoms using this technique in our current setup. Chapter 9 concludes the achievements of this PhD project and gives an outlook over future studies on three-component Fermi mixtures and finite degenerate Fermi gases.

Chapter 2

Ultracold Fermi gases

In our experiments a gas of fermionic ^{6}Li atoms is cooled to a few percent of the Fermi temperature. The atoms are trapped in a potential that can be approximated by a three-dimensional harmonic oscillator. At $T = 0$ the ground state of the system in the absence of interaction is quite simple. The particles fill up the energy levels beginning from the ground state of the harmonic oscillator up to the characteristic Fermi energy which depends on the trapping potential and the number of atoms in the trap. Interactions change this ground state dramatically. Already small attraction between the particles leads to the formation of pairs that can condense into a superfluid. This is comparable to the condensation of cooper pairs in a superconductor.

In general, the theoretical description of interaction effects is rather complicated. Due to the ultralow temperatures of ultracold gases a single number is sufficient to describe the interaction between the constituents. This number is the so-called s-wave scattering length a which corresponds to the lowest term in the partial-wave expansion of the scattering amplitude.

Moreover, ultracold gases offer the unique possibility to change the value of this scattering length by means of Feshbach resonances. These allow to tune the scattering length a to any desired value by applying an external homogeneous magnetic field. In gases of ^{6}Li atoms exceptionally broad Feshbach resonances occur, with a width of a few hundred Gauss.

Of special interest are regimes where the scattering length is larger than the range of the interatomic potential. In this case many properties of the system are universal and do not depend on fine details of the potential at small distances. The so-called unitary regime is reached for $|a| \to \infty$ and can be experimentally accessed by tuning the magnetic field to the value where a Feshbach resonance occurs. In this case the interparticle spacing is the only remaining length scale which means that the properties of the system can be related to the properties of an ideal Fermi gas. An example is the chemical potential which differs from the Fermi energy in

the ideal gas only by a universal factor.

This chapter is organized as follows: The first section is devoted to ideal Fermi gases in traps. Fundamental relations for the Fermi energy and the density distribution in the trap are derived. Afterwards, basic concepts of scattering in ultracold gases are introduced and a proper mathematical definition of the scattering length is given. Then the principles of Feshbach resonances are discussed. The last section is devoted to the concepts of universality and unitarity which have fundamental importance in later parts of this thesis.

2.1 Ideal Fermi gas

Before the effects of interactions in a Fermi gas are discussed, let us consider a sample of non-interacting fermions in a harmonic trap. Although the atoms in the trap are isolated from an external reservoir, it is convenient to study the system in the grand canonical ensemble, that means in terms of temperature T and chemical potential μ. The occupation number of a phase space cell is given by the Fermi-Dirac distribution

$$f(\mathbf{r},\mathbf{p}) = \frac{1}{\exp\left[\left(\frac{\mathbf{p}^2}{2m} + V(\mathbf{r}) - \mu\right)/k_B T\right] + 1}. \tag{2.1}$$

where $V(\mathbf{r})$ is the external trapping potential. The chemical potential is fixed by the constraint that the integral of equation 2.1 over real and momentum space corresponds to the total number of atoms in the trap. Let us first consider the zero temperature case. In this limit the occupation equals one for $\frac{\mathbf{p}^2}{2m} + V(\mathbf{r}) < \mu$ and zero elsewhere. Thus, the chemical potential corresponds to the energy of the highest state that is occupied in the trap, which is the so-called Fermi energy E_F. For a harmonic trap of the form

$$V(x,y,z) = \frac{1}{2}m\left(\omega_x^2 x^2 + \omega_y^2 y^2 + \omega_z^2 z^2\right) \tag{2.2}$$

the Fermi energy is given by

$$E_F = (6N)^{1/3}\hbar\bar{\omega} \tag{2.3}$$

where N is the number of particles in the trap and $\bar{\omega} = (\omega_x\omega_y\omega_z)^{1/3}$ is the mean trapping frequency. The density distribution in the trap is readily calculated by integrating equation 2.1 over momentum space.

$$n(\mathbf{r}) = \int\limits_{|\mathbf{p}|\leq\sqrt{2m(E_F - V(\mathbf{r}))}} \frac{d^3\mathbf{p}}{(2\pi\hbar)^3} = \frac{1}{6\pi^2}\left(\frac{2m}{\hbar^2}\right)^{3/2}(E_F - V(\mathbf{r}))^{3/2} \tag{2.4}$$

A measure for the cloud size is the so-called Fermi radius given by the condition $E_F = V(\mathbf{r})$. It follows $R_{F_i} = \sqrt{\frac{2E_F}{m\omega_i^2}}$.

At finite temperature ($T \lesssim T_F = E_F/k_B$) the integration in equation 2.4 is not that straightforward and results in a polylogarithmic[1] function

$$n(\mathbf{r}) = -\left(\frac{mk_BT}{2\pi\hbar^2}\right)^{3/2} Li_{3/2}\left(-\exp\left(\frac{\mu - V(\mathbf{r})}{k_BT}\right)\right). \tag{2.5}$$

To determine the density profile, the chemical potential is needed. One can show that the chemical potential is given by an implicit function of T/T_F which can only be solved numerically. For $T \ll T_F$ the chemical potential can be approximated by an expansion in terms of T/T_F

$$\mu(T) = E_F\left[1 - \frac{\pi^2}{3}\left(\frac{T}{T_F}\right)^2\right] \tag{2.6}$$

which is known as Sommerfeld expansion. A comparison between the exact values of the chemical potential and the Sommerfeld expansion is shown in figure 2.1. The spatial density distribution can be understood qualitatively in the local density approximation (LDA). In this approximation a local Fermi energy $\epsilon(\mathbf{r}) = E_F - V(\mathbf{r})$ is defined. In the inner parts of the cloud the temperature is smaller than the local Fermi temperature, and the density profile is quite well described by equation 2.4. At the edge of the cloud the local Fermi temperature is small and thus the gas obeys classical Boltzmann statistics. The polylogarithm interpolates between both regimes. Following this reasoning it is also clear that thermometry in a Fermi gas is complicated, as information about the temperature is contained only in the wings of the distribution. More about thermometry in ultracold Fermi gases can be found in [Wen09b]. For more details on ultracold Fermi gases in optical traps, see [Ket08, Joc09].

2.2 Elastic collisions

As already mentioned, the scattering length a is of significant importance in the description of interactions in ultracold gases. The scattering of two particles in the center of mass frame can be described by an incoming plane wave and an outgoing spherical wave whose amplitude is modulated by the scattering amplitude $f_k(\theta, \phi)$.

$$\psi(\mathbf{r}) = e^{ikz} + f_k(\theta, \phi)\frac{e^{ikr}}{r} \tag{2.7}$$

[1] $Li_n(x) = \frac{1}{\Gamma(n)}\int \frac{t^{n-1}dt}{\exp(t)/x - 1}$

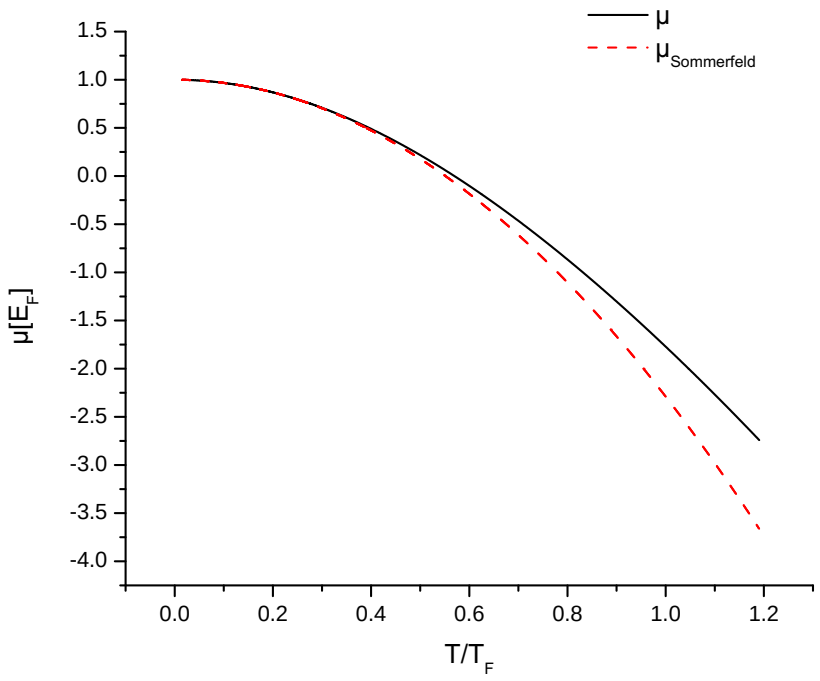

Figure 2.1: Chemical potential of an ideal Fermi gas. The black line shows the exact values obtained in a numerical calculation. The red dashed line shows the Sommerfeld approximation.

For a spherically symmetric interaction potential the scattering amplitude is only a function of the elevation angle θ. Thus, the ϕ dependence is omitted in the following. The scattering amplitude is directly related to the differential scattering cross section via

$$\frac{d\sigma}{d\Omega} = |f_k(\theta) \pm f_k(\pi - \theta)|^2 \tag{2.8}$$

where $\pm$ applies for bosons and fermions respectively. The second term vanishes for distinguishable particles. In order to obtain the total scattering cross section, equation 2.8 must be integrated over half of the solid angle. It is convenient to express the scattering amplitude in terms of angular momentum eigenfunctions

$$f_k(\theta) = \sum_{L=0}^{\infty} \frac{2L+1}{k \cot \delta_L(k) - ik} P_L(cos\theta) \tag{2.9}$$

where $P_L(\theta)$ are Legendre polynomials and $\delta_L(k)$ are the phase shift acquired by each partial wave during the scattering process. The scattering cross section then reads

$$\sigma(E) = \frac{8\pi}{k^2} \sum_{L=0}^{\infty} (2L+1) \sin^2 \delta_L(k). \tag{2.10}$$

For distinguishable particles the prefactor is $\frac{4\pi}{k^2}$ instead of $\frac{8\pi}{k^2}$.

For identical bosons (fermions) the sum only runs over even (odd) L. This is understandable with a simple symmetry argument. In the case of identical bosons the total wavefunction must be symmetric. The total wavefunction is the product of a spin dependent part and a spatial wavefunction whose symmetry is determined by the angular momentum quantum number via $(-1)^L$. For identical bosons the spin wavefunction is obviously symmetric, thus also the spatial wavefunction has to be symmetric and consequently only terms with even L can contribute in the sum of equation 2.10. For fermions the total wavefunction must be antisymmetric and thus the angular momentum quantum number of the spatial wavefunction must be odd.

When the atoms interact via a short range potential the phase shifts $\delta_L(k)$ approach zero like k^{2L+1}, thus in the zero energy limit only s-wave scattering dominates. This is understandable with a simple illustrative argument: angular momentum always involves an angular momentum barrier. When the temperature is low enough the atoms cannot overcome this barrier which leads to a freeze-out of scattering processes with non-zero angular momentum. For ^{6}Li the angular momentum barrier is on the order of $k_B \times 7\,\mathrm{mK}$ [Jul92]. Thus, for temperatures smaller than 7 mK s-wave scattering is the dominant scattering process. P-wave scattering processes are suppressed like $1/E^2$ [DeM99a] where E is the kinetic energy of the atoms.

In this limit the s-wave phase shift can be expressed as a series of powers of k^2

$$k\cot(\delta_0(k)) = -\frac{1}{a} + \frac{1}{2}r_e k^2 + ..., \tag{2.11}$$

which defines the s-wave scattering length a and the s-wave effective range r_e. Plugging the first term of 2.11 into 2.10 and keeping only the $L = 0$ term yields the total scattering cross section in the low energy limit

$$\sigma_{id\ bosons} = \frac{8\pi a^2}{1 + k^2 a^2} \tag{2.12}$$

$$\sigma_{non-id} = \frac{4\pi a^2}{1 + k^2 a^2} \tag{2.13}$$

$$\sigma_{id\ fermions} = 0 \tag{2.14}$$

So far, only elastic scattering was discussed for which the phase shifts have real values. If inelastic channels exist as well, the phase shifts are complex valued with positive imaginary parts. From the discussion above it is clear that at ultralow temperatures identical fermions do not interact due to symmetry reasons. Thus a gas of identical fermions forms an ideal Fermi gas without interactions. For this

reason experiments always work with different internal states of the same atom or with different atomic species. The experiments described in this thesis have been done with the three lowest Zeeman substates of the electronic ground state of ^{6}Li (see figure B.2 in Appendix B).

2.3 Tuning interactions - Feshbach resonance

It is one of the most important properties of ultracold fermionic gases that the value of the scattering length can be tuned to arbitrary values by applying an external magnetic field. This phenomenon is called Feshbach resonance. To understand the underlying physics let us first imagine two atoms interacting via some potential. Assume this potential provides a real bound state below the scattering continuum. From low energy scattering theory, it is known that the scattering length is then positive [Lan81]. Let us now decrease the binding energy of this bound state by for example changing the depth or the shape of the potential. When the bound state approaches the continuum, the scattering length gets larger and diverges when the bound state coincides with the continuum. When the potential is squeezed further, the state emerges into a quasi bound state above the scattering continuum and the scattering length changes sign and becomes negative.

Let us demonstrate the physical origins of a Feshbach resonance at the example of the two lowest spin states of ^{6}Li (see figure B.2 in Appendix B). At sufficiently high magnetic fields ($\gtrsim 100\,G$) a sample of atoms in these two spin states is spin polarized with the electron spin of both states having the same magnetic quantum number of -1/2. Thus, they interact via a shallow triplet potential with some background scattering length. This scattering channel is called the open channel. There is also a second channel, called the closed channel, corresponding to the singlet scattering state, in which both electron spins have opposite magnetic quantum numbers of $\pm$1/2. The scattering continuum of this singlet state is higher in energy than the triplet state continuum and thus not available for the colliding atoms, but it supports a bound state (see figure 2.2 a)). Hyperfine interactions lead to a coupling between both scattering states during a collision. In a simple picture, the two atoms can virtually occupy the bound state of the closed channel, which modifies the scattering phase shift and thus influences the value of the scattering length.

As both scattering states have a different magnetic moment the bound state in the singlet potential can be tuned with respect to the scattering continuum of the triplet state. When it is right above, the scattering length is negative and when it is below the scattering length is positive. If the bound state is tuned to coincide with the scattering continuum, the scattering length diverges. This concept was first studied by H. Feshbach in the framework of nuclear reactions [Fes58]. A rigorous

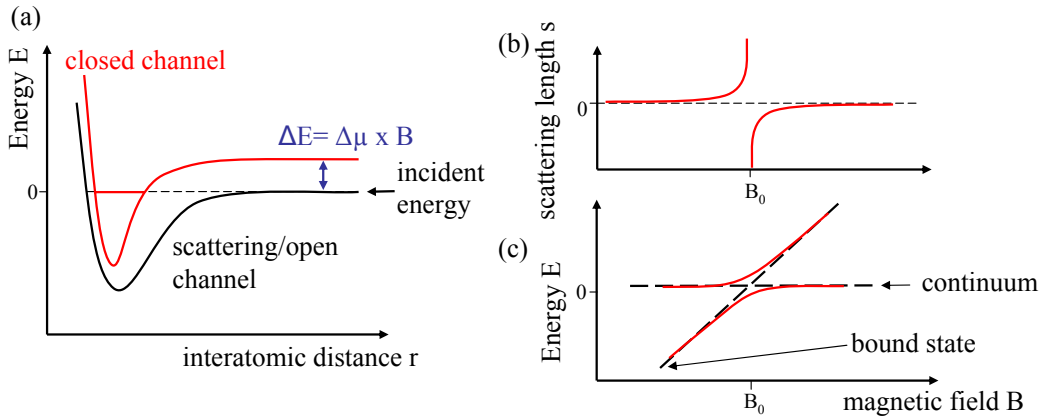

Figure 2.2: a) Principle of a magnetic Feshbach resonance: When the bound state of a closed scattering channel coincides with the continuum of the open channel, the scattering length diverges. Due to different magnetic moments the relative energy of both channels can be tuned with respect to each other. This leads to a magnetic field dependence of the scattering length shown in b). The hyperfine coupling between open and closed channel leads to an avoided crossing between the dressed free atomic state and the bound state depicted in c). This avoided crossing allows for adiabatic conversion of free atoms into weakly bound molecules, by sweeping the magnetic field over the resonance.

treatment [Moe95] shows that the scattering length in the magnetic field region close to resonance behaves like

$$a(B) = a_{bg}\left(1 - \frac{\Delta}{B - B_0}\right) \tag{2.15}$$

where a_{bg} is the background scattering length of the open channel and B_0 is the magnetic field value where the resonance occurs (see figure 2.2 b)). The hyperfine coupling between open and closed channel leads to a dressing of the states in the bare open and closed channels. As a consequence the dressed bound state and the continuum form an avoided crossing (see figure 2.2 c)) that allows for the adiabatic conversion of two free atoms into a bound molecule by sweeping the magnetic field over the Feshbach resonance (see for example [Reg03]).

Feshbach resonances in ^{6}Li

The experiments described in this thesis are performed with atoms in the three lowest Zeeman substates of ^{6}Li. Interaction between particles in these states is

described by three pairwise scattering lengths a_{12}, a_{23} and a_{13}. All binary mixtures exhibit exceptionally broad ($\gtrsim$100 G) and overlapping Feshbach resonances below 1000 G, which allow to tune all pairwise interactions to large values at the same time. In the $|1\rangle - |2\rangle$ scattering channel there is a second, but small resonance with a width of only $\approx 100\, mG$. These resonances are caused by bound states in the singlet potential, corresponding to the highest vibrationally excited level with vibrational quantum number $\nu = 38$. This bound state is split into hyperfine states with $F = 0, m_F = 0$ and $F = 2, m_F = \pm 2, \pm 1, 0$ due to the coupling of two nuclear spins with $I = 1$. The $F = 1$ state is forbidden due to symmetry reasons. Table 2.1 gives an overview over the Feshbach resonances occurring in ^{6}Li. The background scattering length varies for all three pairwise combinations from

Scattering channel	Molecular state	Position[G]	Width[G]
$\|1\rangle\|2\rangle$	$\nu = 38,\ F = 0,\ m_F = 0$	834	-300
$\|1\rangle\|3\rangle$	$\nu = 38,\ F = 2,\ m_F = -1$	691	-122.3
$\|2\rangle\|3\rangle$	$\nu = 38,\ F = 2,\ m_F = -2$	811	-222.3
$\|1\rangle\|2\rangle$	$\nu = 38,\ F = 2,\ m_F = 0$	543	0.1

Table 2.1: Properties of the s-wave Feshbach resonances in the three Zeeman substates of ^{6}Li. The narrow resonance occurs at 543 G. Values taken from [Chi09].

small and positive values in the low field regime to about -2100a_0 for large fields ($\gtrsim$1000 G). This is due to the fact that the scattering states change from a superposition of singlet and triplet states in the Zeeman regime to a pure triplet state in the Paschen-Back regime. The large background scattering length is caused by a virtual bound state just above the scattering continuum of the triplet potential. Figure 2.3 shows the scattering lengths a_{12}, a_{23} and a_{13} as a function of the magnetic field, obtained in a coupled channel calculation [Jul] based on precision measurements[Bar05]. A more detailed discussion of Feshbach resonances can be found in a recent review [Chi09].

2.4 Universality and unitarity in ultracold gases

Universality is a general concept in physics. Its main idea is that macroscopic properties of a system can be expressed by a few universal numbers, without having complete knowledge about the fine details of the system. This means that two different systems that are described by the same universal numbers will have the same macroscopic observables, also when their short-range physics is fundamentally different. In ultracold atoms, universality manifests itself in the fact that

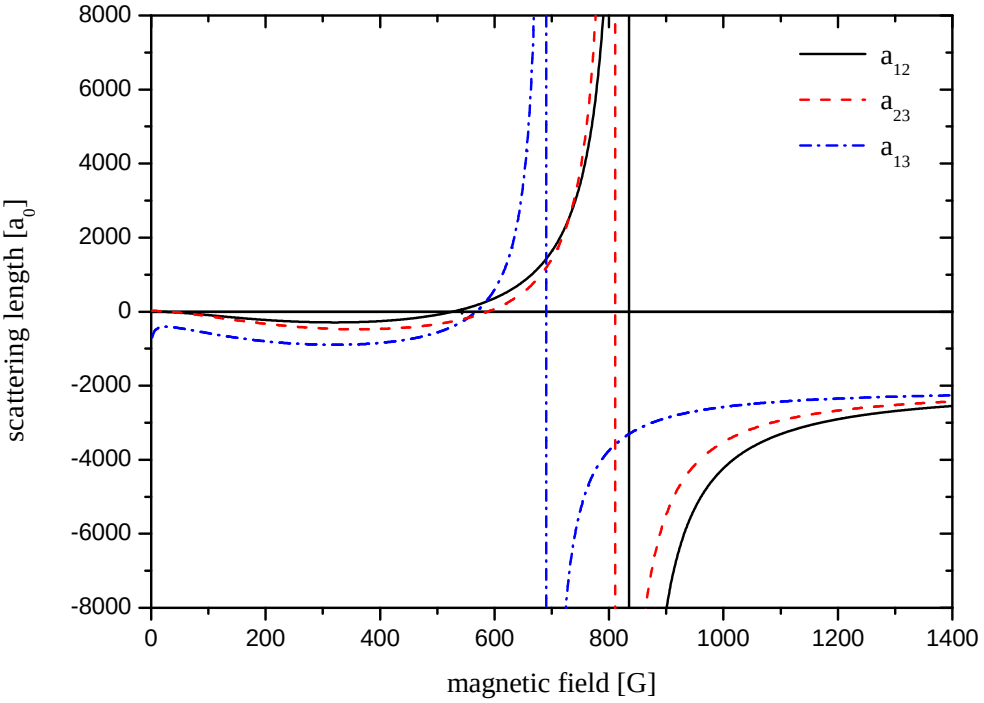

Figure 2.3: Scattering lengths between the three lowest spin states of ^{6}Li in units of Bohr's radius as a function of the magnetic field (from [Jul])

when the scattering length a is larger than the range of the interaction potential r_0, the macroscopic properties of the system depend only on a.

Neutral atoms interact via a van der Waals potential whose attractive part is described via $V = -C_6/r^6$. The range of interaction is given by the van der Waals length

$$l_{vdW} = \left(\frac{mC_6}{\hbar^2}\right)^{1/4} \tag{2.16}$$

which for ^{6}Li has a value of 62.5 a_0 where a_0 is Bohr's radius. For $a \gg l_{vdW}$ the properties of the gas are universal which means that the properties of the gas depend only on the scattering length.[2]

A paradigm example is the binding energy of the weakly bound dimer state that

[2] In chapter 3 it will be shown that for the description of three-body observables an additional three-body parameter is necessary.

is associated with the Feshbach resonance. In the universal regime it is given by

$$E_b = \frac{\hbar^2}{2\mu a^2} \tag{2.17}$$

where μ is the two-body reduced mass. As the experiments described in this thesis are done with atoms of the same mass 2μ will be substituted by the mass m of one atom in the following. Corrections to this universal relation are on the order of $l_{vdW}/\left|a\right|$. The dimer state is a pure two-body effect, but universality also has dramatic consequences for three-body (see chapter 3) as well as many-body physics. In two limiting cases universality is correct

1. The scaling limit: a is fixed and $r_0 \rightarrow 0$
2. The unitary or resonant limit: r_0 is fixed and $|a| \rightarrow \infty$

The scaling limit has proven to be a powerful concept. Simply speaking, the interaction potential between the atoms is substituted by a point-like pseudo-potential involving terms proportional to $\delta^3(\mathbf{r}-\mathbf{r}')$ and $\nabla^2\delta^3(\mathbf{r}-\mathbf{r}')$. The coupling strength is adjusted in a way that the scattering phase shift is the same as for the van der Waals potential. This method is widely used in renormalization group calculations of observables in strongly interacting gases [Bra06].

The scaling limit is connected to a continuous scaling symmetry, in which the scattering length, the spatial coordinates and time are rescaled by powers a positive real number λ.

$$a \rightarrow \lambda a,\ \mathbf{r} \rightarrow \lambda \mathbf{r},\ t \rightarrow \lambda^2 t \tag{2.18}$$

Under these transformation all two-body observables, like the binding energy of the shallow dimer, must be rescaled by appropriate powers of λ.

The unitary limit can be reached in ultracold gases by tuning an external magnetic field to the position of a Feshbach resonance. As the scattering length diverges, the interparticle spacing is the only remaining length scale and all properties of the gas are universally related to the properties of the ideal Fermi gas. An example is the chemical potential at unitarity that differs from the Fermi energy in an ideal gas just by a numerical constant

$$\mu_{unitary} = (1+\beta)E_F. \tag{2.19}$$

β is a universal parameter that cannot be determined analytically. This relation is valid for a bulk medium. In an experiment the atoms are mainly confined in a harmonic trap, which alters equation 2.19 to $\mu_{unitary} = \sqrt{1+\beta}E_F$ in the local density approximation. The size of the cloud with unitary interaction is then a factor of $(1+\beta)^{1/4}$ smaller than in the non-interacting case, assuming the total

atom number is the same. Thus, β is directly accessible in the experiment by measuring the cloud size, but care has to be taken as finite temperature affects the obtained value. The most recent measurement was done in the group of John Thomas at Duke University [Luo09]. They used three different methods, a measurement of the sound velocity ($\beta = -0.565(15)$), extrapolation of $E(S)$ to $S = 0$ ($\beta = -0.59(2)$) and a comparison of the cloud sizes in the strongly and weakly interacting limit ($\beta = -0.61(2)$). All these values agree well within their errors, and also with $T = 0$ Monte-Carlo studies ($\beta = -0.58(1)$) [Car03, Cha04, Ast04], ($\beta = -0.58(1)$) [Bul06] and ($\beta = -0.60(1)$) [Car08].

Chapter 3

Universal few-body physics in ultracold gases

As discussed in the last chapter universality has important consequences for the description of two-body systems. Only one example is the shallow dimer associated to a Feshbach resonance, whose binding energy depends only on the value of the scattering length.

Vitaly Efimov studied the three-body problem in the case of resonant two-particle interactions [Efi71, Efi70, Efi79]. He found that above a critical value of the interaction strength universal three-body bound states are supported. With increasing scattering length their number increases, being infinitely large on resonance with an accumulation point at the scattering continuum. This theory was originally developed for a system of bosonic particles. Although our experiments are performed with three distinguishable fermions, the experimental observations can be interpreted with a straightforward modification of the boson model as discussed in chapter 6.

This chapter summarizes textbook results on the bosonic system and is organized as follows: In the first section of this chapter we will discuss qualitatively the properties of the so-called Efimov trimers. Afterwards, a more thorough treatment of the three-body problem follows, introducing hyperspherical coordinates and the Faddeev equations. So far, Efimov states have only been indirectly observed in a resonant enhancement of three-body recombination, a loss process in which three atoms scatter to form a deeply bound molecule and a free atom. The energy release in this process is sufficiently high, that both the atom and the molecule can leave the trap. Thus, the last two sections of this chapter are devoted to three-body recombination and the experiments that showed evidence for Efimov-states in systems of ultracold atoms.

3.1 Universal trimers - Efimov states

In the 1970's Vitaly Efimov considered an ensemble of spinless identical particles interacting via resonant two-particle interactions. He assumed that the resonance arises due to a bound state in the two-body scattering potential, as it is the case for a Feshbach resonance.

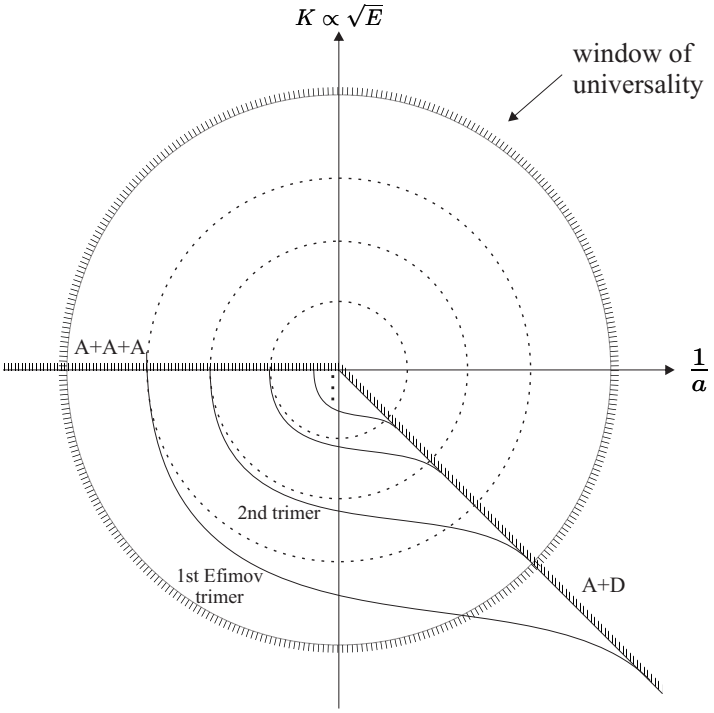

Figure 3.1: Efimov's scenario: A series of universal three-body bound states emerge due to resonant two-body interactions. On resonance ($1/a = 0$) an infinite tower of bound states appears with an accumulation point at zero energy. The binding energy of these trimers shows a logperiodic behaviour and differs by a factor of about 515. The scattering continua of three free particles and a dimer plus a free particle are shown as hatched lines in the plot. The values for the scattering length where a trimer hits the three particle or the dimer-particle scattering continuum are logperiodic with a scaling factor of about 22.7. Also shown is the so-called window of universality, in which the description with a universal theory is a valid approximation. It is defined by $\sqrt{K^2 + (1/a)^2} \leq 1/r_0$, where $K \propto \sqrt{E}$ is the energy variable, a the scattering length and r_0 is the range of the two-particle interactions (more details described in the text).

He predicted that when the scattering length between the particles is sufficiently large a whole series of three-body bound states appears which fulfill a discrete scaling symmetry. Figure 3.1 illustrates the phenomenology. For the application of universal theory two requirements have to be fulfilled. First the kinetic energy of the particles must be low enough such that their thermal de Broglie wavelength is too large to probe the details of the interaction potential. Secondly, the scattering length must be larger than the range of the interaction potential. Thus, a so-called window of universality can be defined by $\sqrt{K^2 + (1/a)^2} \leq 1/r_0$ where K is the wavenumber of the particles and r_0 is the range of the interaction potential. In this window of universality the application of universal theory is a valid approximation.

Starting from small negative scattering lengths within the window of universality, at a certain critical value a_* a bound state of three particles arises, whose binding energy increases with increasing $|a|$. The values of a for which a new trimer state arises show a logperiodic behaviour with a scaling factor of $\exp(\pi/s_0) \approx 22.7$, where $s_0 = 1.00624$ is the scaling parameter. Thus the next trimer appears at $a \approx 22.7 a_*$. The number of bound states for a given scattering length can be estimated to be $N \approx s_0/\pi \ln(|a|/r_0)$. On resonance the number of bound states is infinite with an accumulation point at the scattering continuum. The spectrum is bound from below, by the condition that the binding energy of the trimer is smaller than $\hbar^2/mr_0^2$, in order to be in the universal regime. The binding energy on resonance, denoted by $\hbar^2\kappa_*^2/m$, is also logperiodic with a scaling factor of $\exp(2\pi/s_0) \approx 515.03$ For a single Efimov state, the relation between a_* and κ_* can be shown to be [Bra06]

$$a_* = -1.56(5)\kappa_*^{-1}. \tag{3.1}$$

Crossing the resonance the binding energy decreases again and the trimer emerges into a dimer plus a free particle. This happens when the scattering length reaches the value given by [Bra06]

$$a_{*_{ad}} = 0.071\kappa_*^{-1}. \tag{3.2}$$

Note that $a_{*_{ad}}$ is much smaller than a_* so that the first Efimov trimer, being universal on the negative scattering length side of the resonance, leaves the window of universality on the positive side before it merges with the continuum. From equations 3.1 and 3.2 it follows

$$a_* \approx -22 a_{*_{ad}}, \tag{3.3}$$

which makes clear that the first Efimov trimer will never merge the continuum in the universal regime on the positive side of the resonance. Thus, no prediction

about its behaviour can be made applying universal theory. The value of a_*, or equivalently $a_{*_{ad}}$ or κ_*, depend on the details of the interaction potential and cannot be calculated. Thus an additional three-body parameter enters the problem that can only be determined in an experiment. This new three-body parameter breaks the continuous scaling symmetry known from the two-body problem (see 2.4) to a discrete scaling symmetry:

$$\kappa_* \rightarrow \kappa_*,\ a \rightarrow \lambda_0^m a,\ \mathbf{r} \rightarrow \lambda_0^m \mathbf{r},\ t \rightarrow \lambda_0^{2m} t \tag{3.4}$$

where m is an integer and $\lambda_0 = \exp(\pi/s_0)$ is the discrete scaling parameter. Under this symmetry, observables like scattering cross sections or binding energies scale with appropriate powers of λ_0. This means that along a dashed circle in figure 3.1, these observables have the same value. The values on adjacent rings are determined by rescaling with appropriate powers of λ_0.

3.2 Theory of the three-body problem - The hyperspherical approach

The last section was devoted to a more qualitative description of universal three-body bound states in a system with resonant two-body interactions. Here, a more thorough analysis of the three-body problem will be given. The solution of the three-body problem is one of the notoriously difficult problems in physics. Already the classical problem of three massive particles interacting via gravitational forces is hard to treat. And so is the quantum-mechanical analogue. In principle, one has to solve the Schrödinger equation for three particles interacting via some potential V.

$$\left[-\frac{\hbar^2}{2m}\sum_{i=1}^{3}\nabla_i^2 + V(\mathbf{r_1},\mathbf{r_2},\mathbf{r_3})\right]\psi(\mathbf{r_1},\mathbf{r_2},\mathbf{r_3}) = E\psi(\mathbf{r_1},\mathbf{r_2},\mathbf{r_3}) \tag{3.5}$$

The three-body problem involves nine degrees of freedom, after transformation into the center-of-mass frame six variables are still remaining.

3.2.1 Hyperspherical coordinates

To simplify mathematics it is convenient to express these variables in so called hyperspherical coordinates. In figure 3.2 the vector $\mathbf{r}_{ij}$ and $\mathbf{r}_{k,ij}$ are defined as the separation between a pair and as the separation between the third atom and the center of mass of the pair respectively. The hyperspherical coordinates are a set of variables that are expressed in terms of the relative coordinates defined above.

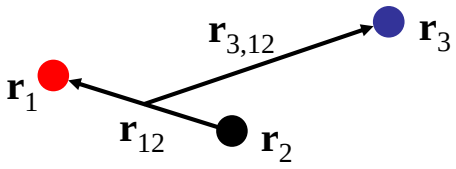

Figure 3.2: Example of the relative coordinates $\mathbf{r}_{ij}$ and $\mathbf{r}_{k,ij}$ in a three-body system.

This set includes the so-called hyperradius

$$R = \sqrt{r_{12}^2 + r_{13}^2 + r_{23}^2}, \tag{3.6}$$

one of the Delves hyperangles [Del60]

$$\alpha_k = \arctan \frac{\sqrt{3} r_{ij}}{2 r_{k,ij}} \in [0, \pi/2) \tag{3.7}$$

and the unit vectors $\hat{r}_{i,j}$ and $\hat{r}_{k,ij}$. α_k is close to zero when the third particle is far away from the center of mass of the pair and is close to $\pi/2$ when it is close by. The hyperangle and the unit vectors are called the hyperangular variables $\Omega = (\alpha_k, \hat{r}_{i,j}, \hat{r}_{k,ij})$. Transformed into the center of mass frame and expressed in hyperspherical coordinates the Schrödinger equation reads

$$\left(T_R + T_{\alpha_k} + \frac{\Lambda_{k,ij}^2}{2mR^2} + V(R, \Omega) \right) \psi(R, \Omega) = E\psi(R, \Omega), \tag{3.8}$$

where T_R and T_{α_k} are the kinetic energy operators associated with R and α_k respectively. $\Lambda_{k,ij}$ is a generalized angular momentum operator including usual angular momentum operators in the $\mathbf{r}_{ij}$ and $\mathbf{r}_{k,ij}$ subsystems. More details about hyperspherical coordinates can be found in [Nie01].

3.2.2 Faddeev equations

The Schrödinger equation in 3.8 does not make use of the fact that the description of the problem becomes easier in the situation where two particles are close together, forming a two-body cluster and one particle being further apart. The Faddeev equations form a set of three coupled differential equations that are equivalent to 3.8 and make use of this simplification. The discussion follows the reasoning in [Bra06]. We assume that the three-body interaction potential can be written as a sum of two-body potentials in the form

$$V(\mathbf{r}_1, \mathbf{r}_2, \mathbf{r}_3) = V(\mathbf{r}_{12}) + V(\mathbf{r}_{13}) + V(\mathbf{r}_{23}). \tag{3.9}$$

In this assumption an intrinsically existing three-body interaction is neglected. This approximation is not as coarse as it appears as at low energy the effects of an intrinsic three-body interaction can be reproduced by a sum of pairwise interactions [Bra06].

The Faddeev equations then read

$$\left(T_R + T_{\alpha_k} + \frac{\Lambda_{k,ij^2}}{2mR^2}\right)\psi^{(k)} + V(\mathbf{r}_{ij})(\psi^{(k)} + \psi^{(i)} + \psi^{(j)}) = E\psi^{(k)}. \tag{3.10}$$

If the functions $\psi^{(k)}$ are solutions of the Faddeev equations, their sum is a solution to the Schrödinger equation 3.8.

$$\psi(\mathbf{r}_1, \mathbf{r}_2, \mathbf{r}_3)) = \psi^{(1)}(\mathbf{r}_{23}, \mathbf{r}_{1,23}) + \psi^{(2)}(\mathbf{r}_{13}, \mathbf{r}_{2,13}) + \psi^{(3)}(\mathbf{r}_{12}, \mathbf{r}_{3,12}) \tag{3.11}$$

In general, the Faddeev wavefunctions $\psi^{(k)}$ can be expanded in a series of spherical harmonics. In the zero energy limit all terms including angular momenta are suppressed, and the wavefunction 3.11 reduces to

$$\psi(\mathbf{r}_1, \mathbf{r}_2, \mathbf{r}_3)) = \psi(R, \alpha_1) + \psi(R, \alpha_2) + \psi(R, \alpha_3) \tag{3.12}$$

in the case of three identical particles. Since the hyperangles α_k are not independent of each other it is possible to reduce the three Faddeev equations to one integro-differential equation for $\psi(R, \alpha)$ [Fed93], resulting in

$$\begin{aligned}(T_R + T_\alpha - E)\,\psi(R,\alpha) = -V(\sqrt{2}R\sin\alpha)\times \\ \left[\psi(R,\alpha) + \frac{4}{\sqrt{3}}\int_{|(1/3)\pi-\alpha|}^{(1/2\pi-|(1/6)\pi-\alpha|)} \frac{\sin(2\alpha')}{\sin(2\alpha)}\psi(R,\alpha')d\alpha'\right],\end{aligned} \tag{3.13}$$

where α is one of the three hyperangles. This equation is called the low-energy Faddeev equation.

To solve this equation $\psi(R, \alpha)$ is expanded in a series of hyperangular functions $\Phi(R, \alpha)$

$$\psi(R,\alpha) = \frac{1}{R^{5/2}\sin(2\alpha)}\sum_n f_n(r)\Phi(R,\alpha). \tag{3.14}$$

The α dependent part of 3.14 yields a integro-differential eigenvalue equation for $\Phi_n(R, \alpha)$ in which R is treated as a parameter. The eigenvalues $\lambda_n(R)$ are thus a function of the hyperradius R. Plugging the series expansion 3.14 into the low-energy Faddeev equation, projecting onto $\Phi_n^*(R, \alpha)$ and neglecting off-diagonal and other small terms yields a Schrödinger equation in the radial coordinate

$$\left[\frac{\hbar^2}{2m}\left(-\frac{\partial^2}{\partial R^2} + \frac{15}{4R^2}\right) + V_n(R)\right] f_n(R) \approx E f_n(R), \tag{3.15}$$

where the hyperspherical potentials $V_n(R)$ are given by

$$[\lambda_n(R) - 4] \frac{\hbar^2}{2mR^2}. \tag{3.16}$$

The neglection of off-diagonal coupling terms between hyperspherical potentials with different n is called adiabatic hyperspherical approximation. This approximation is valid only for values of the hyperradius which are much smaller ($R \ll |a|$) or much larger ($R \gg |a|$) than the absolute of the scattering length [Bra06]. For $R \sim |a|$ and $a > 0$ the coupling between different hyperradial potentials leads to minima in the three-body recombination rate due to destructive interference of two different decay paths (see 3.3).

3.2.3 Hyperspherical potentials

For a two-body potential with large scattering length ($a \gg r_0$), the low-energy Faddeev equation 3.14 can be reduced to an exact transcendental equation for the channel eigenvalues $\lambda_n(R)$ [Fed93, Bra06]. This equation can be solved numerically and the resulting hyperspherical potentials are shown in figure 3.3 as a function of R/a. The two lowest hyperspherical potentials are attractive $\sim 1/R^2$

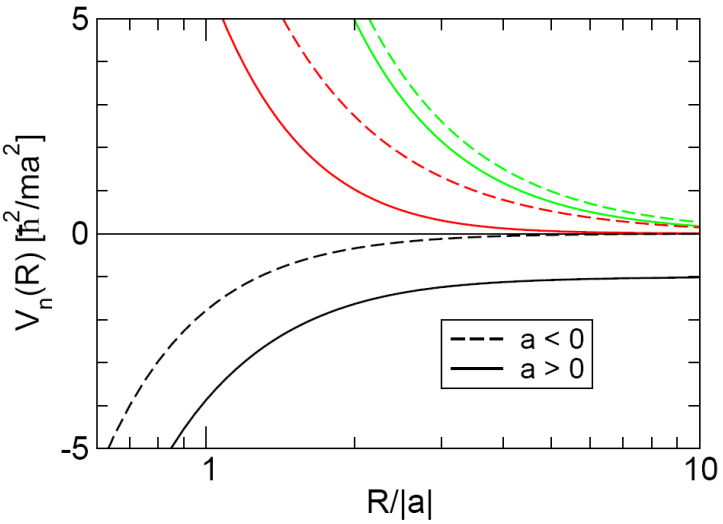

Figure 3.3: Hyperspherical potentials for a two-body scattering potential with large scattering length as a function of R/a. The figure was taken from [Bra06].

potentials for both signs of the scattering length, while all higher potentials are repulsive. For $R \to \infty$ all potentials, except the lowest one for positive scattering length, converge to zero energy. The lowest potential for positive scattering length

converges to $-\hbar^2/2ma^2$, corresponding to the lowest scattering state of a dimer plus a free particle. For $R/a \to 0$ the eigenvalues $\lambda_n(R)$ approach fixed values. For the lowest eigenvalue λ_0, the limiting behaviour is given by

$$\lambda_0(R) \to -s_0^2 \left(1 + 1.897\frac{R}{a}\right) \tag{3.17}$$

where $s_0 = 1.00624$. For $|a| \to \infty$ the hyperradial eigenvalue equation for the lowest hyperspherical potential can thus be written as

$$\frac{\hbar^2}{2m}\left[-\frac{\partial^2}{\partial R^2} - \frac{s_0^2 + 1/4}{R^2}\right] f_0(R) = E f_0(R). \tag{3.18}$$

This equation is the Schrödinger equation for a particle in a $1/R^2$ potential. It is only correct in the so called scale-invariant region $r_0 \ll R \ll |a|$. The wave function for $R \leq r_0$ is very complicated and depends strongly on the details of the interaction potential. It must match the hyperradial wave which can effectively be described by a single number. This number is precisely the three-body parameter, discussed in 3.1. As the scattering length does for the two-body problem , the three-body parameter describes the effects of the short range interaction potential on the long-range wave function by a single number. The attractive $1/R^2$ potential supports an infinite number of bound states, whose binding energies are fixed by the three body parameter. These states are the Efimov states for $|a| \to \infty$. An obvious choice for the three-body parameter is the binding wave number of one of these Efimov states. The binding energies can then be expressed as

$$E_T^{(n)} = \left(e^{-2\pi/s_0}\right)^{n-n_*} \frac{\hbar^2\kappa_*^2}{m}. \tag{3.19}$$

Thus, adjacent Efimov states are separated by a factor of $e^{2\pi/s_0}$ in binding energy.

3.3 Three-body recombination in ultracold gases

So far Efimov states have not been observed directly, for example with a spectroscopic technique or by preparation of a sample of stable trimers. The only experimental evidence is the observation of an enhanced three-body recombination rate (see 3.4). Three-body recombination is a process in which three particles collide to form a dimer and a free atom. The release of the binding energy is in most cases sufficiently high for the dimer and the free atom to leave the trap. The crossing of an Efimov trimer with the three-atom scattering threshold leads to a resonant enhancement of the recombination rate which is observable in the experiment. It

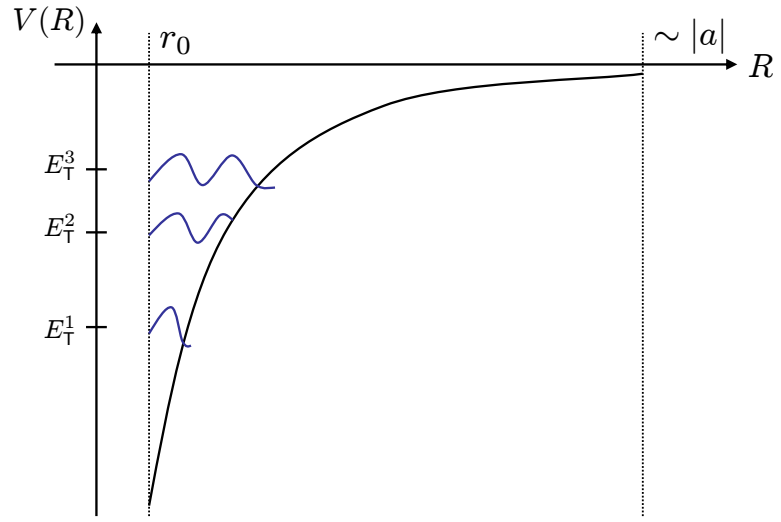

Figure 3.4: Sketch of the lowest hyperspherical potential with the three lowest Efimov states. The $1/R^2$ potential is only valid in the so-called scale-invariant region, $r_0 \ll R \ll a$, and has to be cut off at r_0, r_0 being the range of the two-body potential. The wavefunction in the short range region can be very complex and is unknown in most cases. The effects of this short range part of the interaction potential on the long-range wave function can be expressed by a single number, the three-body parameter.

is worth discussing the theoretical treatment of three-body recombination, as we will use the results to analyse the data presented later in this thesis.

The strength of three-body loss is expressed by the three-body loss coefficient K_3 which is defined by

$$\frac{dn(\mathbf{r})}{dt} = -K_3 n^3(\mathbf{r}). \tag{3.20}$$

It was shown [D'I04, Esr99] that K_3 is proportional to the absolute square of the S-matrix element $S_{AAA\to AD}$ for scattering of three free atoms into an outgoing state of a dimer plus a free atom. Efimov himself gave simple rules based on probability conservation which enable the calculation of S-matrix elements. These rules are called Efimov's radial law [Efi79].

3.3.1 Efimov's radial law

For the following it is useful to define four different regions for the hyperradial variable R.

- short-distance region $R \sim r_0$
- scale-invariant region $r_0 \ll R \ll |a|$
- long-distance region $R \sim |a|$
- asymptotic region $R \gg |a|$

In the asymptotic region the atoms are either in a atom-dimer or three free atom scattering state. The wavefunction in the long distance region may be rather complicated. In the scale-invariant region the wavefunction is a hyperradial wave in the lowest hyperradial potential for $a < 0$ or in the second lowest one for $a > 0$, which both converge to zero for $R \to \infty$ (see figure 3.3). This hyperradial wave is connected to the wavefunction in the short-distance region via the three-body parameter.

The evolution of the asymptotic wavefunction through the long-distance region is described by a unitary 3×3 matrix.

$$s_{i,j} = \langle i\, out|\hat{U}|j\, in\rangle. \tag{3.21}$$

$\hat{U}$ is the evolution operator that evolves the wavefunction through the long-distance region. $|i\, in\rangle$ and $|j\, out\rangle$ where $i = 1, 2, 3$ denote hyperradial waves (1), atom-dimer states (2) and free three atom scattering states (3) flowing into or out of the long-distance region respectively. The hyperradial waves are reflected at the short-distance region and acquire a universal phase $\exp(2i\theta_*)$, in which θ_* is an alternative choice for the three-body parameter introduced above. The S-matrix elements describing the evolution of the incoming asymptotic states into the outgoing ones can then be expressed as follows

$$\begin{aligned} S_{AD,AD} &= s_{22} + s_{21}\frac{e^{2i\theta_*}}{1 - e^{2i\theta_*}s_{11}}s_{12} \\ S_{AAA,AD} &= s_{32} + s_{12}\frac{e^{2i\theta_*}}{1 - e^{2i\theta_*}s_{11}}s_{31} \\ S_{AAA,AAA} &= s_{33} + s_{31}\frac{e^{2i\theta_*}}{1 - e^{2i\theta_*}s_{11}}s_{13}. \end{aligned} \tag{3.22}$$

The considerations leading to these results are depicted in figure 3.5. The first term on the right hand side represents direct reflection from the long-distance region. The second term corresponds to the transition through the long-distance region, followed by continuous reflections at the short- and long-distance regions before transmission into an asymptotic scattering state. Efimov's radial law puts strong constraints on the dependence of physical observables on the scattering length and the energy of the particles. It is useful to define new variables in the

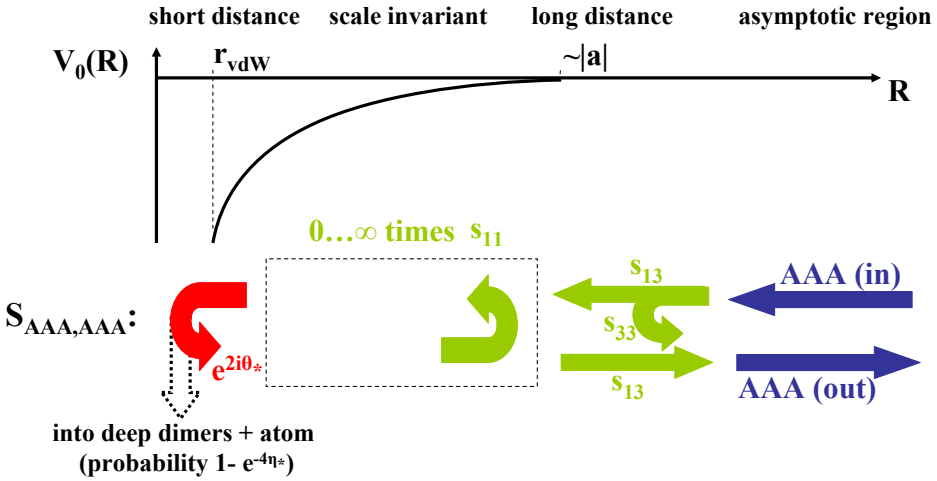

Figure 3.5: Calculation of the S-matrix element $S_{AAA,AAA}$ using Efimov's radial law. At the long distance region, the wave is either transmitted or directly reflected. The reflection gives rise to the first terms in equation 3.22. The transmitted wave is reflected at the short-distance region acquires a phase shift and is again transmitted or reflected at the long-distance region. This can be repeated an arbitrary number of times, leading to a geometric series whose limit gives rise to the second terms in 3.22. When deeply-bound (non-universal) trimers are present, the amplitude of the reflected wave at the short-distance region is $\exp(-2\eta_*)$ times the amplitude of the incoming wave, where η_* is the elasticity parameter, see 3.3.3

(K,$1/a$) plane of figure 3.1. Efimov introduced polar coordinates (H, ξ) where H is a radial variable and ξ is the angle with respect to the positive scattering length axes in figure 3.1. The radial variable H enters the S-matrix only via the phase angle θ_* and the elements of the unitary matrix s_{ij} only depend on the angular variable ξ. At fixed ξ the physical observables are invariant under the discrete scaling transformation introduced in section 3.1. Thus, the calculation of the S-matrix elements can be reduced to the calculation of a few universal functions of ξ, determining the matrix s_{ij}. This radial law allows to express observables like scattering cross-sections as log-periodic functions of the dimensionless variable $\kappa_* a$. Some examples concerning three-body recombination are discussed in the following.

3.3.2 Three-body recombination into a shallow dimer

For large and positive scattering lengths a shallow dimer below the three-atom scattering continuum exists. This dimer is directly associated with the two-body scattering resonance (see 2.3). Nielsen and Macek [Nie99] and Esry et al. [Esr99]

used the hyperspherical framework to derive an approximate expression for the three-body recombination rate into the shallow dimer that is associated with the two-body resonance.

$$K_{3,\text{shallow}} \approx C_{max} \sin^2 \left[s_0 \ln(a/a_{*ad}) + \gamma \right] \frac{\hbar a^4}{m} \tag{3.23}$$

The constants C_{max} and γ can be calculated using field-theoretical methods [Bed00, Bra03]. figure 3.6 shows its dependence on the scattering length in units of a_{*ad}. Note that for certain values of the scattering length a the rate for three-body re-

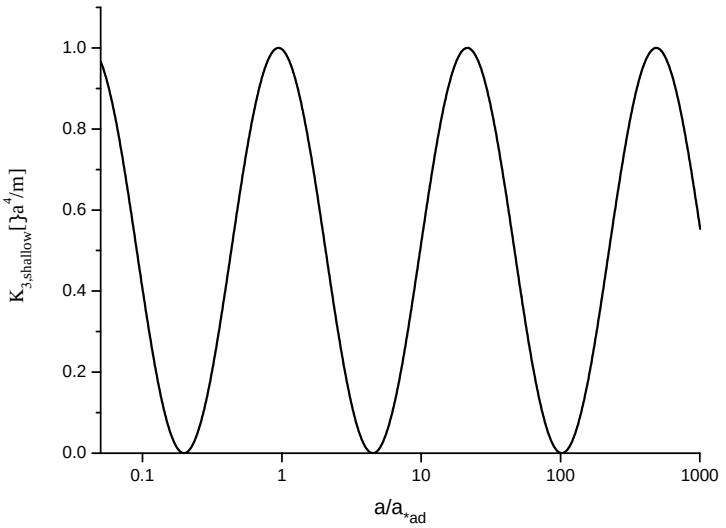

Figure 3.6: Rate coefficient for three-body recombination into the shallow dimer that is associated with the two-body scattering resonance ($a > 0$). At certain values of the scattering length the recombination rate drops to zero which is due to destructive interference between two decay paths. The maxima are reached near the value where an Efimov state merges with the atom-dimer continuum. The a^4 dependence was removed for better visibility and C_{max} was arbitrarily set to one. The value of γ was set to 1.67 which can be calculated using field-theoretical methods [Bed00, Bra03]

combination drops to zero. This remarkable effect arises due to destructive interference between two decay paths. Let us imagine three free atoms in a scattering state approaching the long-distance region. The long distance region acts as a barrier, with reflection and transmission coefficients described by the unitary matrix s_{ij}. Part of the incoming wave is directly reflected as an atom-dimer scattering state while the other part is transmitted into the lowest hyperspheric potential shown as the solid black line in figure 3.3. This transmission corresponds

to a non-adiabatic transition between the two potentials. The resulting hyperradial wave is reflected at the short-distance region and subsequently transmitted at the long-distance region. As the lowest hyperradial potential for positive scattering length converges to $-\hbar/ma^2$, it is highly transmittive for a wave with $E = 0$. This transmitted wave then interferes with the one, that was directly reflected at the long distance-region. The positions of the zeros are at

$$a \approx 4.51(e^{\pi/s_0})^n a_{*ad}, \tag{3.24}$$

the maxima arise close the scattering length value, where an Efimov state merges with the atom-dimer continuum. Depending on the value of the dimensionless variable $\kappa_* a$ this interference can be totally constructive or destructive, leading to the oscillatory behaviour of the three-body recombination rate. These oscillations are also known under the name Stückelberg oscillations [Stü32].

3.3.3 Effects of deep dimers

In his derivation of the scattering S-matrix Efimov neglected the influence of deeply bound (non-universal) dimers below the scattering threshold. The assumption that the hyperradial wave is totally reflected at the short-distance region is only valid if no such deep dimers are present. This is in general not the case, as the van der Waals potential of alkali metals supports many bound states. The effects of deep dimers can be included by adding a complex part to the scattering phase shift $\theta_* \rightarrow \theta_* + i\eta_*$. η_* is called the elasticity parameter and accounts for decay into deep dimers. The S-matrix elements for this case are simply given by the substitution of θ_* by $\theta_* + i\eta_*$. The decay into a deep dimer results in high-energy scattering states consisting of an atom and a dimer with both having large kinetic energy. These states are denoted by X in the following. The S-matrix elements for this process can be determined analogously to the considerations described in 3.3.1 by treating the short-distance region in the same way as the long-distance region before. The wave function in the short-distance region may be very complicated, but the conservation of probability must be fulfilled. The evolution of an incoming radial wave into an outgoing state, which may be a reflected hyperradial wave or a high energy scattering state is described by a unitary matrix t_{ij}. The matrix element for reflection is simply given by

$$t_{11} = \exp(-2\eta_* + 2i\theta_*). \tag{3.25}$$

The probability for the incoming hyperradial wave to evolve into a high energy scattering state is consequently

$$\sum_X |t_x|^2 = 1 - e^{-4\eta_*}. \tag{3.26}$$

The S-matrix elements for the evolution of an incoming atom-dimer or three-atom scattering state in a high energy scattering state are determined in the same way as in 3.3.1. They are

$$S_{X,AD} = t_{X1}s_{12} + t_{X1}\frac{s_{11}e^{-2\eta_*+2i\theta_*}s_{12}}{1-e^{-2\eta_*+2i\theta_*}s_{11}}$$
$$S_{X,AAA} = t_{X1}s_{13} + t_{X1}\frac{s_{11}e^{-2\eta_*+2i\theta_*}s_{13}}{1-e^{-2\eta_*+2i\theta_*}s_{11}} \tag{3.27}$$

It is again possible to derive an approximate analytic expression for three-body recombination into the shallow dimer for positive scattering length in dependence of the elasticity parameter η_* (see figure 3.7) [Bra06].

$$K_{3,\text{shallow}} \approx C_{max}e^{-2\eta_*}(\sin^2[s_0\ln(a/a_{*ad}) + \gamma] + \sinh^2\eta_*)\frac{\hbar a^4}{m}) \tag{3.28}$$

Decay into the deep dimers reduces the visibility of the Stückelberg oscillations discussed above. The deep dimers also open a decay path for the Efimov trimers, resulting in a finite width of these states. For small η_* the width of trimers can be approximated by [Bra06]

$$\Gamma_T \approx \frac{4\eta_*}{s_0}\left(E_T + \frac{\hbar^2}{ma^2}\right) \tag{3.29}$$

where E_T is the binding energy of the trimer.

3.3.4 Three-body recombination for negative scattering lengths

For negative scattering lengths no shallow dimers exist. Thus, only recombination into the deep dimers is possible which is simply proportional to the fourth power of the scattering length

$$K_{3,\text{deep}} \approx 16.7(1-e^{-4\eta_*})\frac{\hbar a^4}{m} \qquad (a>0) \tag{3.30}$$

The crossing of an Efimov state with the free atom-continuum leads to a resonant enhancement of the three-body recombination rate into the deep dimers. In the collision process the trimer is virtually occupied and subsequently decays into a high energy scattering state of a free atom and a deeply bound dimer. Braaten and Hammer [Bra06] give an analytic formula for the three-body loss coefficient K_3

$$K_{3,deep} = \frac{c\sinh(2\eta_*)}{\sin^2(s_0\ln(a/a_*)) + \sinh\eta_*}\frac{\hbar a^4}{m} \tag{3.31}$$

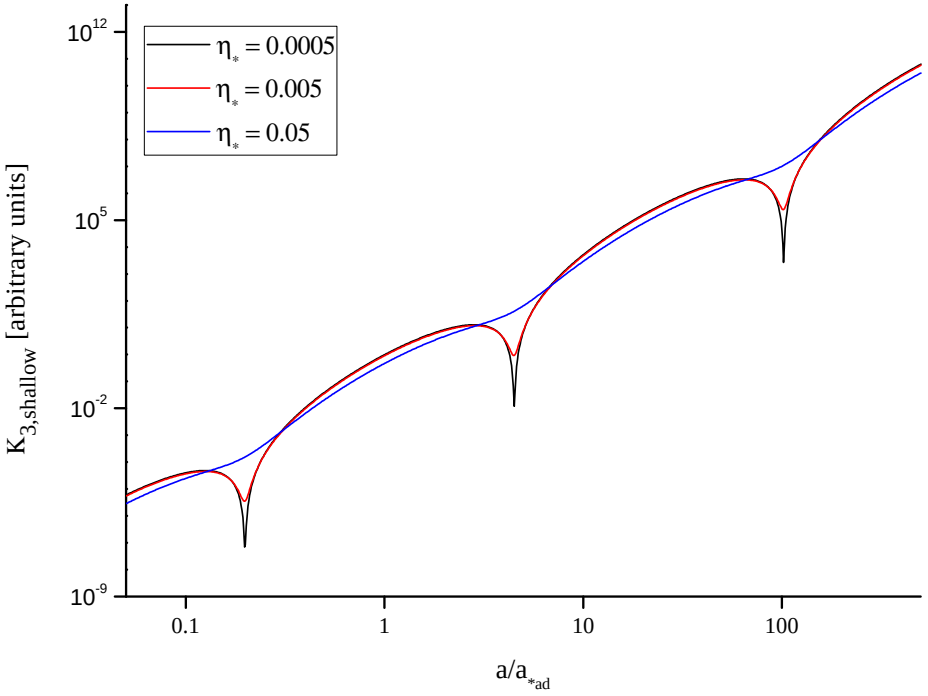

Figure 3.7: Rate coefficient for three-body recombination into the shallow dimer in dependence of the elasticity parameter η_*. Decay into the deep dimer leads to a loss of visibility in the interference between the two decay paths. For the plot C_{max} was arbitrarily set to one and for γ the value 1.67 from field-theoretical methods [Bed00, Bra03] was used. $\hbar$ and m were also set to one. Thus the plot shows only the qualitative behaviour of $K_{3,\mathrm{shallow}}$, the exact value depends strongly on the system under study.

where c is a constant. This formula will be used in chapter 6 for the interpretation of our experimental results. In figure 3.8 the three-body loss-coefficient is shown in dependence of the scattering length and the elasticity parameter η_*. In the experiment only a limited number of resonances can be observed, as the maximum loss rate is limited by unitarity to some temperature dependent value (see 3.3.5). Additionally, the observable spectrum is limited from below by the range of the two-particle interactions r_0.

3.3.5 Thermal effects

In the last section, the influence of deeply bound dimers on the observable three-body recombination rate was discussed. It was shown that for both positive and negative scattering lengths, recombination into such dimers washes out the re-

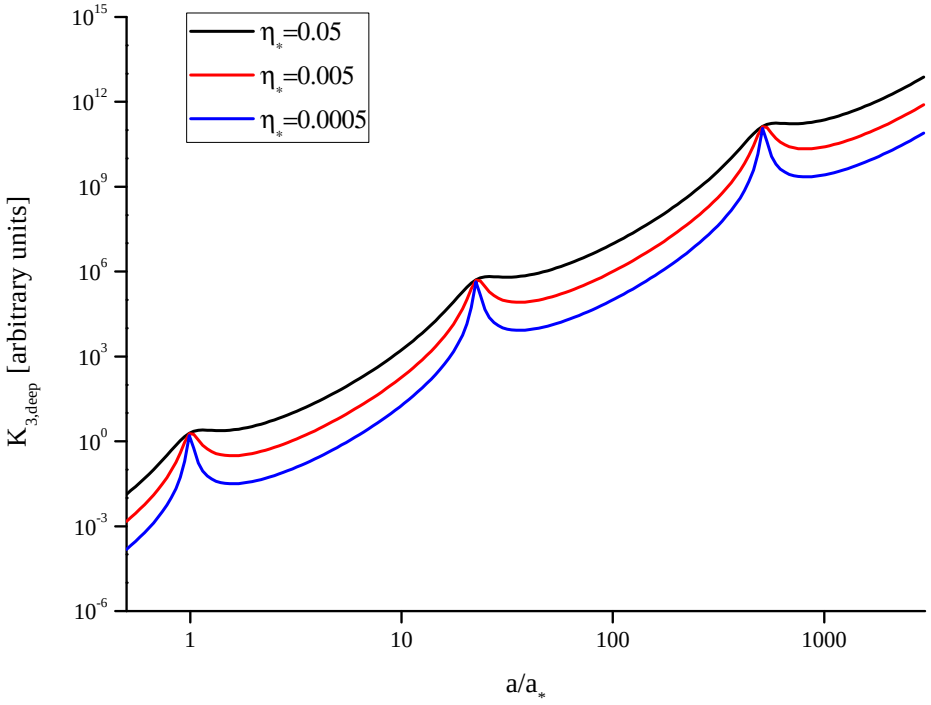

Figure 3.8: Rate coefficient for three-body recombination at negative scattering lengths in presence of Efimov trimers. Every time an Efimov trimer crosses the free atom continuum the three-body loss rate is resonantly enhanced. These resonances are superimposed on the general a^4-scaling. Decay into deeply bound dimers leads to a wash-out of the resonances. For the plot $a_*, c, \hbar$ and m were set to one.

combination minima and maxima respectively. The expressions for the rate of three-body recombination given in the last paragraphs are strictly valid only in the threshold regime, in which the collision energy is the smallest energy in the system. For positive scattering length this regime is naturally bounded by the binding energy of the universal dimer $\hbar^2/ma^2$. For negative scattering length the limit is set by the potential barrier in the lowest three-body entrance potential [Esr99]. The latter constraint is about a factor of three stricter than the condition for positive scattering lengths. The effects of finite temperature on the observable three-body loss were thoroughly discussed in [D'I04].

There are three main effects that influence the observable recombination rate: unitarity, thermal averaging and higher partial waves. The influence of higher partial waves scales with E^2a^8 and is for most experimental parameters negligible. Thermal averaging becomes important for energies on the border of the threshold regime and makes the observation of recombination maxima and minima much

more difficult. Unitarity limits the maximum observable loss rate at finite temperature and leads to a saturation effect at large scattering lengths. The maximum K_3 due to unitarity can be easily derived from the expression in [D'I04][1]

$$K_3 = \frac{1}{2}\sum_{J,\pi}\sum_{i,f}\frac{32N!(2J+1)\pi^2\hbar}{\mu k^4}|S^{J\pi}_{f\leftarrow i}|^2. \tag{3.32}$$

Here N is the number of identical particles involved, J stands for angular momentum, π for the parity of the state, μ is the three-body reduced mass[2] and $k = \sqrt{2\mu E/\hbar^2}$ the thermal wavenumber. i, f denote initial and final states respectively. In the unitary regime the S-matrix element approaches unity and thermal averaging results in an additional factor of one half. In our experiments only the s-wave contribution ($J = 0$) has significant importance. Thus, the observable values for K_3 are limited from above by

$$K_{3,max} = \frac{32\pi^2\hbar}{4\mu k^4} = \frac{2\pi^2\hbar^5}{\mu^3(k_B T)^2} \tag{3.33}$$

D'Incao et al. [D'I04] define a critical scattering length above which the contrast of maxima and minima in the three-body loss coefficient K_3 may be considerable reduced

$$a_c = \frac{\hbar}{\sqrt{mk_bT}}. \tag{3.34}$$

where m is the atomic mass. For scattering lengths larger than a_c thermal effects may considerably affect the observed behaviour of K_3 considerably. In experiments this is a serious concern and must be taken into account.

3.4 Experimental evidence for Efimov states

Although nearly forty years passed since Efimov predicted the existence of universal trimers, it has not been possible to observe them directly in an experiment. Lim et al. [Lim77] proposed that the excited state of the ^{4}He trimer is an Efimov trimer, while the universality of the ground state which was experimentally observed by Schöllkopf and Toennies [Sch96] is still debated.

So far, the only experimental evidence for the existence of Efimov states is the resonant enhancement of the three-body recombination and atom-dimer loss in samples of ultracold gases. The first observation of this kind was made in the group of Rudi Grimm in Innsbruck in 2006 [Kra06], using a sample of ultracold,

[1] The definition of K_3 in [D'I04] differs by a factor of two from the definition used throughout this thesis. Therefore a factor of 1/2 half was introduced in equation 3.32.

[2] $\mu = \sqrt{(m_1m_2m_3)/(m_1+m_2+m_3)}$

but still thermal, bosonic ^{133}Cs atoms. They found a resonant enhancement of three-body loss for negative scattering length and a loss minimum for positive values. The unusual scenario in this experiment is that both regions are not connected via a two-body scattering resonance but a zero crossing of the scattering length. This may be the reason why the location of the maximum and the minimum can not be described by the same three-body parameter. The deviation is about 25%. This may also be caused by non-universal corrections, as the minimum occurs at only twice the van-der Waals length. The application of universal theory in this regime is questionable. Three years later a resonance in inelastic ultracold atom-dimer scattering was observed in the same group [Kno09]. This resonance can be attributed to the merging of an Efimov trimer with the atom-dimer threshold. Unfortunately, it was not possible to connect this resonance to the features observed in the former experiment using universal relations.

The first spectrum of Efimov states was discovered in a sample of ^{39}K atoms by studying three-body loss in dependence of the scattering length [Zac09]. For positive values the scattering length was tuned over more than three orders of magnitude revealing two loss minima and two slight enhancements due to atom-dimer resonances. The enhancement of the loss at atom-dimer resonances is caused by secondary collisions of the highly energetic dimers, produced via three-body recombination in the sample. The negative scattering length regime was studied over nearly two orders of magnitude and one recombination maximum was discovered. While the ratio of the scattering length values where the two minima occur are consistent with universal theory, the other ratios differ from the expected value. For larger scattering lengths the measured values coincide better with the theoretically expected ones, as non-universal corrections become less important.

Gross et al. studied a system of bosonic ^{7}Li atoms close to wide Feshbach resonance [Gro09]. A loss minimum for positive scattering length and an enhancement for negative values were found. The ratio of the scattering lengths where both features occur are in remarkable agreement with universal theory.

Barontini et al. [Bar09] demonstrated for the first time Efimov physics in a hetero-nuclear atomic system. They studied a mixture of ^{41}K and ^{87}Rb in the vicinity of an interspecies Feshbach resonance and observed two loss resonances for negative scattering length, which can be attributed to Efimov resonances in the KRbRb and the RbKK channel. This is the first demonstration that two resonant interactions between the three particles are sufficient for Efimov physics to occur. They also observed an enhancement of inelastic atomic loss at positive scattering lengths, for which an atom-dimer resonance in the KRbRb channel might be responsible.

In a recent experiment Ferlaino et al. [Fer09] found evidence for universal tetramer states in ^{133}Cs tied to the Efimov trimer via universal relations. The existence of these tetramers was theoretically predicted by von Stecher et al. [Ste09],

who found evidence for them in earlier measurements of the same group. The surprising property of these tetramers is that no additional four-body parameter is needed for their theoretical description. This means that for example the scattering length value where the tetramer crosses the free atom continuum differs only by a universal factor from a_*.

Chapter 4

Experimental setup

This chapter gives an overview of the experimental setup, most of which was built during the first year of this PhD project. Main design goals were to keep the setup as simple and reliable as possible. Therefore well-established techniques were used whenever they were available. This enabled fast progress during the building phase which allowed to do experiments very soon.

The chapter is organized as follows: First a description of the vacuum setup is given. Then all parts of the experimental setup necessary for the preparation, manipulation and detection of ensembles of ultracold ^{6}Li atoms are described. This includes the first cooling stages from an atomic beam to a laser-cooled cloud of atoms, as well as the optical dipole trap in which the ultralow temperatures necessary to achieve quantum degeneracy can be reached by evaporative cooling. For efficient evaporative cooling high thermalization rates are necessary which can be reached by tuning the s-wave scattering length to large values. As described in chapter 2 this is accomplished by making use of the broad Feshbach resonances between different spin states of ^{6}Li . Thus, magnetic field coils are needed which are capable of generating a large homogeneous magnetic field at the position of the atoms. Manipulation of the atoms is mainly done by applying radio frequency (RF) fields, with which it is possible to induce transitions between different spin states. This tool is for example essential to prepare a three-component Fermi mixture as described in chapter 6. In the last part of this chapter the real time based control system of the experiment will be described.

4.1 Vacuum chamber

Prerequisite for experiments with ultracold atoms is that they are performed in an ultra high vacuum (UHV) environment with a background pressure of less than 10^{-11} mbar. If the background pressure is too high, large trap losses due to colli-

sions with the residual background gas occur which leads to a dramatic reduction of the lifetime of the atoms in the trap and makes experiments impossible.

In figure 4.1 a cut through the complete vacuum setup is shown. It is divided in two main parts: the oven chamber and the main chamber which are separated by a differential pumping stage and an all metal gate valve (VAT). This valve allows to isolate the oven chamber from the rest of the apparatus and the oven can be refilled without breaking the vacuum in the main chamber. The low background pressure

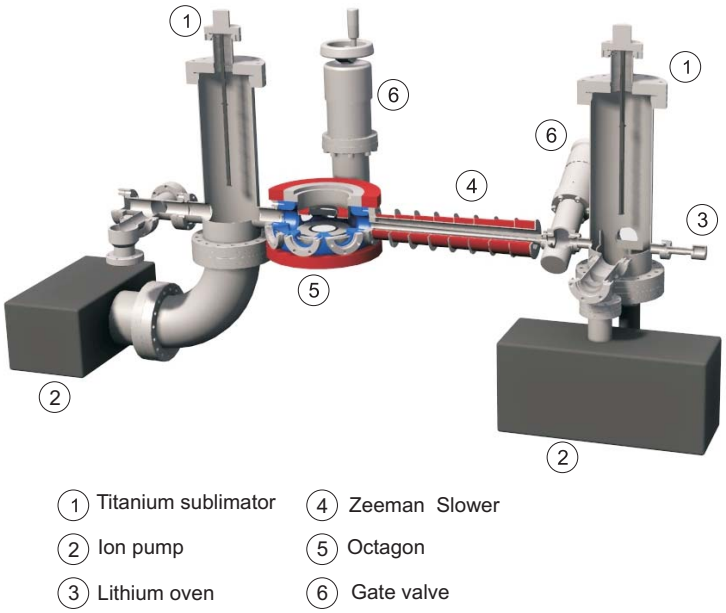

Figure 4.1: Cut through the complete vacuum setup.

is maintained by two ion getter pumps (Varian StarCell 40 l/s H_2, 15 l/s Ar at the oven chamber and Varian Star Cell Vacion Plus75 40 l/s H_2, 20 l/s Ar at the main chamber). Additionally, we use two filament type titanium sublimation pumps (VARIAN) to reduce the background pressure of H_2. In order to reach a high flux of ^{6}Li atoms the oven must be heated to temperatures around 350 °C which limits the pressure in the oven chamber to about 10^{-10} mbar. Thus, a differential pumping stage is necessary which is capable of maintaining a sufficient pressure gradient between main and oven chamber. This differential pumping stage consists of a stainless steel tube with a length of 320 mm which also serves as the drift tube for the Zeeman slower. The inner diameter of the tube increases towards the main chamber from 5 mm to 16 mm allowing for transversal expansion of the atomic beam while the atoms are decelerated.

The main part of the vacuum apparatus is a spherical octagon (Kimball Physics, MFC600-SO200800-A) in which the experiments are performed. The use of the

octagon has several advantages. It provides lots of optical access and the windows can be antireflection coated on both sides, in contrast to glass cells which are often only coated on the outside. On top and bottom of the main chamber two custom made reentrant viewports (special techniques group of UKAEA) are attached. They provide two large windows (40 mm clear aperture) at an inner distance of 17.7 mm away from the center of the octagon. This allows for the use of a large numerical aperture lens (NA ~ 0.65) for collecting light from a large solid angle and thus efficient atom detection. This lens is also used to focus a laser beam to a waist in the micrometer range to form a tight optical dipole trap (see sections 4.2.4 and 4.3.3). Additionally, the reentrant viewports provide enough space for mounting the Feshbach coils. This brings them close to the atoms which reduces the electric current that is needed for the generation of the Feshbach field and thus reduces power consumption inside the coils. Figure 4.2 shows a photograph of the octagon with the reentrant viewports already in place.

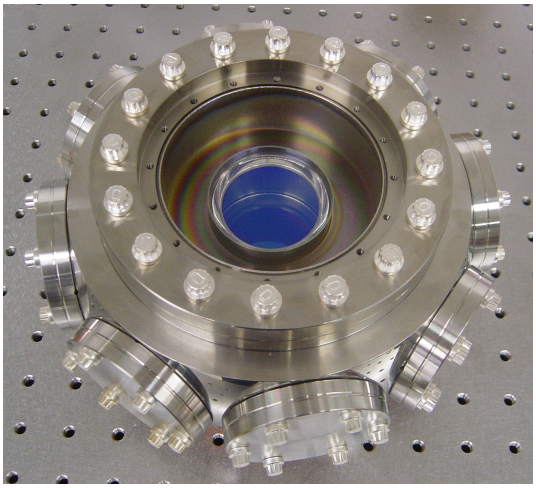

Figure 4.2: Octagon with reentrant viewports. The large viewports close to the atoms allow the collection of light from a large solid angle with high numerical aperture optics. This optics can also be used to focus a laser beam to a waist in the micrometer range, forming a tight optical dipole trap. Furthermore, there is space around the windows to place the Feshbach coils close to the atoms.

In order to assure a good vacuum environment inside the octagon it was coated with a NEG (non evaporable getter) coating at GSI. The coating consists of an TiZrV alloy and does not only prevent outgasing from the underlying substrate but also getters residual gas molecules similar to a titanium sublimation pump. The coating was deposited before the assembly of the chamber and activated during bake-out of the apparatus. Using all these pumping techniques we reach a background pressure around 10^{-12} mbar at the position where the atoms are trapped.

Unfortunately, we cannot directly measure the pressure inside the octagon, but the long lifetime of atoms in the (magneto-optical trap) MOT and the dipole trap (see sections 4.2.3 and 4.3) suggest such a low pressure value. Attached to the octagon is an all metal gate valve (VAT) which allows for future extension of the apparatus. Additional tools for manipulation and detection of atoms could be inserted through this valve into the chamber without breaking the vacuum.

In order to reach high loading rates of the MOT, the flux of atoms from the oven has to be optimized. Our design of the oven is quite simple and turned out to work very well. The oven consists of a small stainless steel cylinder serving as a reservoir for metallic lithium. It is attached to the right hand side of the setup, shown in figure 4.1. A heating wire wrapped around this cylinder heats it up to 360 °C leading to evaporation of lithium atoms into the gaseous phase. The large oven aperture of r = 5 mm leads to a high flux of atoms, resulting in short MOT loading times, see section 4.2.3. More details concerning the design of the vacuum setup and especially the oven can be found in the Diploma thesis of Friedhelm Serwane [Ser07].

4.2 Laser cooling and imaging of ^{6}Li atoms

In this section the parts of the experimental setup used for laser cooling and trapping as well as for imaging of ^{6}Li atoms are discussed. First of all, an overview of the laser system providing the laser light for deceleration in the Zeeman slower and trapping in the MOT as well as for imaging is given. Then basic principles of laser cooling and their implementation in our setup are described. The last part of this section is devoted to the imaging systems with which all quantitative information about the prepared samples is inferred.

4.2.1 Laser system

Two basic requirements have to be met by the laser system providing the near resonant light at 671 nm. On the one hand, the linewidth of the lasers must be significantly smaller than the linewidth of the respective transitions for cooling and imaging, which is $\sim$6 MHz. On the other hand the frequency of the lasers must be easily tunable over a range of up to 1 GHz which is essential for Doppler cooling and imaging of the atoms at high magnetic fields. For these reasons the whole 671 nm laser system is built using grating stabilized diode lasers manufactured by Toptica. Figure 4.3 shows an overview over the laser system, which is set up on a separate optical table in our laboratory. Single mode polarization maintaining fibres are used to transfer the light to the main chamber on the other table.

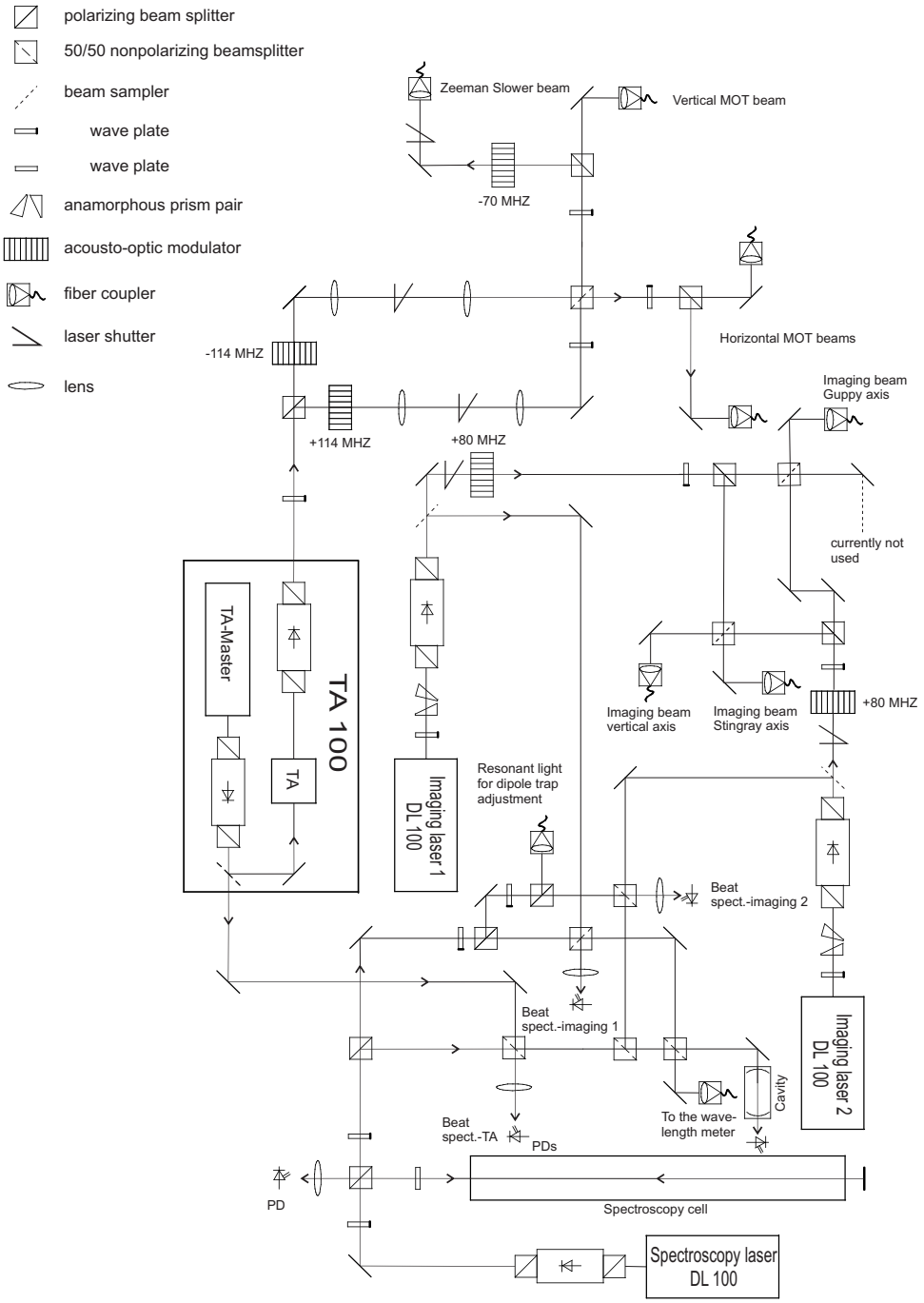

Figure 4.3: Overview of the 671 nm laser system.

The spectroscopy laser (Toptica, DL100) is stabilized to the F = 3/2 transition of the D2-line at 670.977 nm (see figure B.1) using Doppler free frequency modulation spectroscopy in a lithium vapour cell [Ser07]. The cell is evacuated and contains metallic lithium which is heated to 310 °C in order to provide sufficient lithium vapour pressure for spectroscopy. This laser serves as the frequency reference for all other lasers used for laser cooling and imaging. Two additional DL100 lasers are used for absorption imaging (see section 4.2.4) of the atoms. They are stabilized in reference to the spectroscopy laser using a standard offset locking technique [Sch99]. This allows to tune these lasers independently over a wide range which is necessary for absorption imaging at different magnetic field values. As high frequency beat notes have to be recorded in this case we use a special metal-semiconductor metal photodetector (Hamamatsu, G4176-03) with a rise and fall time of typically 30 ps. The use of two independent imaging lasers makes the acquisition of experimental data faster since two spin states can be imaged independently in the same experimental cycle. For fast switching of the imaging pulses the light is fed through AOMs (Crystal Technology, 3080-125) which shift the frequency of the light 80 MHz to the blue. The light for MOT and Zeeman slower is supplied by a tapered amplifier system (Toptica, TA 100) with an output power of $\sim$400 mW behind the optical isolator. The master laser of the tapered amplifier is also stabilized in reference to the spectroscopy laser using the same locking technique as for the imaging lasers. The light is split at a polarizing beam splitter cube in a ratio of 2:1 for the cooling and repumping transitions (see section 4.2.3 and figure B.1). The corresponding frequency shift of $\pm$ 114 MHz is done by two AOMs (AA Optoelectronics, MTS114-B10A3-671) which are also used to control the intensity of the beams. The beams are overlapped on a non-polarizing beam splitter and coupled into optical fibres for transfer to the main chamber. The light for the Zeeman slower is additionally 70 MHz red shifted by an AOM before being coupled into the fibre.

4.2.2 Zeeman slower

As described before, the atoms leave the oven with a thermal velocity distribution with a mean velocity of 1500 m/s. Before they can be trapped in the MOT they have to be slowed down to velocities below the capture velocity of the trap which is on the order of 100 m/s. This is accomplished in a so-called Zeeman-slower. In this slower the atoms are decelerated by scattering photons from a laser beam with propagation direction opposite to the velocity of the atoms. By absorbing a photon from the beam the atom receives a momentum kick of $\hbar k$ opposite to its movement direction. Since the emission of photons is randomly distributed over the complete solid angle the average momentum transfer from the emission is zero. This results in a net momentum transfer in the direction of the laser beam

and thus to a deceleration of the atoms. Due to the Doppler-effect the atoms would quickly be off-resonant with the laser beam when their velocity is reduced. Thus, they would not scatter photons any more and their deceleration would be zero. To overcome this problem, the Zeeman slower makes use of a spatially varying magnetic field, which is adjusted in a way that it compensates the Doppler shift by Zeeman shifting the addressed transition. Expressed in a formula this means that

$$\delta_0 + kv + \frac{\mu B}{\hbar} = 0 \tag{4.1}$$

must always be fulfilled. Here δ_0 and μ are the detuning of the laser beam from the transition at zero magnetic field and the magnetic moment of the atom respectively

For our Zeeman slower we chose a decreasing field configuration which means that the magnetic field value inside the slower decreases monotonously towards the MOT. The last part of the decreasing field is provided by the MOT coils which has the advantage that the final part of the deceleration occurs in a region very close to the MOT. This reduces the expansion of the atomic beam in the transverse direction and increases the number of atoms that can be captured in the MOT. A sketch of our slower is shown in figure 4.4. It is mounted on the differential pumping stage between oven and main chamber. The drift tube has a length of 320 mm and is of conical form to allow for an expansion of the beam in transverse direction while the atoms are decelerated. The slower beam enters the vacuum setup through a window on the side opposite to the oven. It is slightly focused, having a diameter of about 30 mm at the window, while its focus lies approximately at the position of the oven. The beam has a power of $\sim$30 mW, corresponding to about $4\times$ the saturation intensity in the middle of the slower where the beam has a radius of about 5 mm. The frequency of the laser light is 120 MHz red detuned from the transition at zero magnetic field. For fields $\gtrsim$100 G the used transition is closed, less repumper light (see section 4.2.3) is needed in the slower compared to the MOT beams. Details about the slower configuration can be found in table 4.1 and in [Ser07].

4.2.3 Magneto optical trap (MOT)

Atoms leaving the Zeeman slower still have velocities on the order of 100 m/s. Further cooling is performed in the magneto-optical trap (MOT). This trap combines a magnetic quadrupole field with six laser beams pointing towards the zero point of the magnetic field. One pair of beams is aligned to coincide with the radial symmetry axis of the magnetic field, while the other two orthogonal pairs lie in the plane normal to it. The laser beams alone form a so-called optical molasses. If the frequency of the laser is red detuned with respect to the optical transition the atoms feel a velocity dependent force, opposing the movement of the atoms,

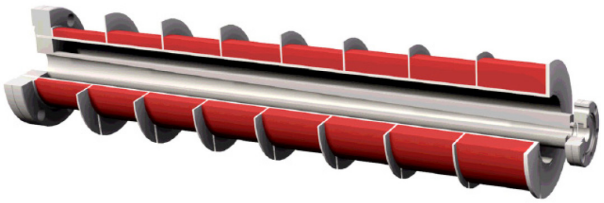

Figure 4.4: Cut through the Zeeman slower, which is mounted on the differential pumping stage between oven and main chamber. Note the conical form of the drift tube to allow for an expansion of the beam in transverse direction while the atoms are decelerated.

length	40 cm including MOT field
coils	8
current coil 1 - 7	5.4 A
current coil 8	2.5 A
max magnetic field	754 G
maximum capture velocity	800 m/s
detuning	-120 Mhz
beam power	$\sim$30 mW
total electric power	370 W

Table 4.1: Main parameters of the Zeeman slower.

which leads to a compression in momentum space. The temperature that can be reached by this method is limited by the stochastic nature of absorption and emission of photons heating the sample. Setting cooling and heating rates equal results in a minimum achievable temperature of

$$T_D = \frac{\hbar\Gamma}{2k_B} \tag{4.2}$$

where Γ is 2π times the linewidth γ of the cooling transition. This temperature is called the Doppler limit and is reached in the limit of intensities much smaller than the saturation intensities at a detuning of $\delta = \gamma/2$. For ^{6}Li the Doppler temperature is 140 μK. Adding the magnetic quadrupole field and choosing appropriate circular polarizations of the laser beams lead to an additional spatial confinement of the atoms. Please refer to [Met99] for more details on laser cooling.

In our setup the quadrupole field is generated by a pair of coils in anti-Helmholtz configuration which are positioned around the flanges of the reentrant viewports.

They are made of flat copper wire with a cross section of $5\times1\,\mathrm{mm}^2$. Each coil consists of 4 layers with 24 windings in each layer. The current used for MOT loading is 32 A, resulting in a magnetic field gradient of 40 G/cm in axial and 20 G/cm in the radial direction. For the MOT beams we use three retro-reflected beams with a diameter of about 20 mm. As cooling transition we use the transition from the F = 3/2 manifold of the $2^2S_{1/2}$ ground state to the $2^2P_{3/2}$ excited state (see figure B.1). For loading the MOT the cooling laser is 40 MHz ($\sim7\gamma$) red detuned from the resonance frequency. At low magnetic fields this transition is not closed and atoms can decay into the F = 1/2 manifold of the groundstate and thus get lost from the cooling process. Therefore, we shine in a second laser frequency, called repumper which is red detuned from the F = 1/2 $\leftrightarrow$ $2^2P_{3/2}$ transition by the same amount as the cooling light. In total we use 70 mW of cooling and 26 mW of repumper light. The distribution among the trapping beams is optimized for maximum transfer into the dipole trap. Figure 4.5 shows a photograph of an atomic cloud captured in the MOT. The lifetime of the atoms in the MOT is on the order of 10 minutes, indicating a very low background pressure. Using

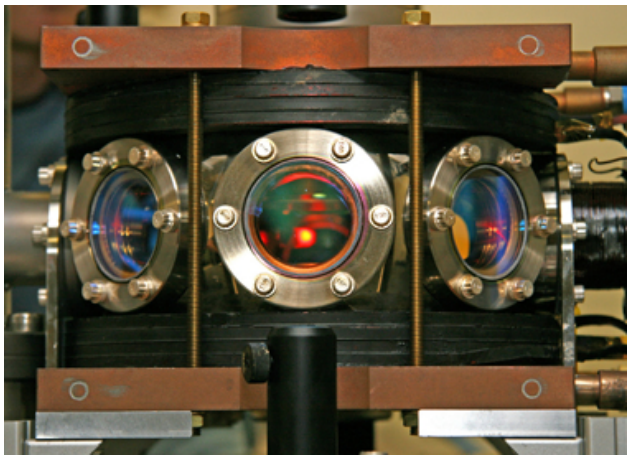

Figure 4.5: A cloud of ^{6}Li atoms captured in the MOT. The coils generating the quadrupole field together with their cooling plates are also visible.

an oven temperature of 360 °C, we reach a loading rate of 10^8 atoms/s. Thus, for most experiments it is sufficient to load the MOT for one or two seconds, which shortens the experimental cycle time significantly. After the loading phase the atoms are prepared for transfer into the optical dipole trap (see section 4.3) by applying a Doppler cooling scheme. The laser intensity is ramped down to zero within 12 ms. At the same time the detuning of the lasers is tuned towards resonance. It was experimentally determined that a final detuning of about -1 γ leads to the best transfer efficiency. Typical temperatures of about 250 μK and a phase space density of 8×10^{-6} are reached. During the intensity ramp the atoms

are optically pumped into the F = 1/2 manifold by applying more cooling than repumper light in the end of the transfer. This is necessary as inelastic collisions of atoms in the F = 3/2 state would lead to a reduced lifetime of the sample in the dipole trap. The optimum parameters for the transfer ramps are determined experimentally. For more information about the transfer please refer to [Lom08].

4.2.4 Imaging systems

In our setup two imaging methods are applied: For determination of the atom number in the MOT usually fluorescence imaging is used while information about ultracold clouds as for example the atom number or density distribution in the dipole trap is inferred using the absorption imaging technique. First, the principles of both methods are discussed and afterwards their implementation in our setup is described.

Fluorescence imaging

The principle of fluorescence imaging is straightforward. Light scattered by the atoms is collected with a lens and projected onto the chip of a CCD camera or a photodiode. In our setup fluorescence imaging is done along the axis perpendicular to the Zeeman slower (see figure 4.7). The light is collected by a plano-convex gradium lens (Lightpath) with a focal length of 120 mm and a diameter of 50 mm and projected onto the CCD camera (Guppy F-038B NIR, AVT) by a standard spherical lens with f = 200 mm. The numerical aperture of this lens system is limited by the viewport to 0.18. Thus, about 8 ‰ of the photons scattered by the atoms can be detected. For a quantitative determination of the atom number the relation between counts on the camera and the number of photons hitting on the chip must be known. This can be measured by illuminating the chip with a laser beam of well known intensity. For our Guppy in gain mode one, one count on the camera corresponds to 226 photons at a wavelength of 671 nm.

On resonance and for intensities much larger than the saturation intensity the atoms scatter photons with a rate of $\Gamma/2$ corresponding to 18.45 Mhz. Using the numbers given above this results in a calibration factor κ of

$$\kappa = 653 \, \frac{\text{counts}}{\text{atom s}}. \tag{4.3}$$

This means that one atom accumulates in one second 653 counts on the camera in our current setup. For large clouds saturation effects like reabsorption of photons in the cloud can lead to a systematic error on the atom number. Therefore, it is useful to work with a detuning of the laser beams, as then saturation effects become less important. On the other hand this lowers the scattering rate and using

the calibration factor given above, leads to an underestimation of the atom number. In this case, the atom number can be calibrated by comparing the fluorescence of a small cloud on resonance with the fluorescence observed for the same cloud when a detuning is applied.

Absorption imaging

Absorption imaging is the standard method to image ensembles of ultracold atoms. The atoms are illuminated with a resonant light pulse and the resulting shadow image is projected onto a camera. Naturally, the atoms are heated by the light pulse, thus the sample is destroyed and for each single measurement a new cloud has to be prepared. There are also non destructive methods like phase-contrast or dark-ground imaging, but as they are not applied in our setup we refer the reader to [Ket99], where basics of these techniques are discussed.

In the experiment, absorption imaging is performed in the following way: In each experimental cycle three pictures are taken. The first one is the absorption image I_{abs} with the atoms, the second one is a reference image I_{ref} without atoms, but with the imaging pulse present and the third image is a background image I_{bg} without imaging pulse. From these three pictures the relative transmission is deduced.

$$T(x,y) = \frac{I_{abs}(x,y) - I_{bg}(x,y)}{I_{ref}(x,y) - I_{bg}(x,y)} \tag{4.4}$$

From this relative transmission, it is possible to deduce the atom number in the following way: The intensity of the imaging beam while passing the cloud is reduced according to Lambert-Beer's law

$$\frac{dI}{I} = -n(z)\,\sigma(z)\,dz \tag{4.5}$$

where $n(z)$ is the particle density and $\sigma(z)$ the scattering cross section which in general depends on the light intensity and therefore on the position within the cloud.

$$\sigma(z) = \sigma_0 \frac{1}{1 + \frac{I(z)}{I_s} + \left(\frac{2\delta}{\gamma}\right)^2} \tag{4.6}$$

where $\sigma_0 = \frac{3\lambda^2}{2\pi}$ is the scattering cross section of a closed transition, with resonance wavelength λ.

In the following we assume that the imaging laser is tuned to resonance, that means $\delta = 0$. For the two limiting cases of intensities much smaller and much higher than the saturation intensity, it is easy to find a solution of equation 4.5:

1. $I \ll I_s$: The cross section becomes intensity independent, $\sigma(z) = \sigma_0$, and the solution to 4.5 reads

$$I(z) = I_0 \exp\left(-\sigma_0 \int n(z)\, dz\right). \tag{4.7}$$

Thus, the number of atoms imaged onto one pixel of the CCD camera is calculated in the low intensity limit as

$$N_{pixel}(x, y) = -\frac{A}{\sigma_0 M^2} \ln\, T(x, y) \tag{4.8}$$

where A and M are the pixel size of the camera and the magnification of the imaging system respectively. $-\ln\, T(x, y)$ is also called the optical density.

2. $I \gg I_s$: In this case the cross section can be approximated by $\sigma(z) = \frac{\sigma_0 I_s}{I(z)}$ and the solution to 4.5 is given by

$$I(z) = I_0 - I_s \sigma_0 \int n(z)\, dz \tag{4.9}$$

resulting in

$$N_{pixel}(x, y) = -\frac{A}{\sigma_0 M^2} \frac{I_0}{I_s} \left(1 - T(x, y)\right) \tag{4.10}$$

For all intermediate cases only numerical solutions can be found and the determination of the atom number runs into problems. Especially, for in-situ imaging of dense clouds in the dipole trap, none of the given approximations is justified. In figure 4.6 the relative error for the deduced atom number in dependence of the used imaging intensity is visualized. This graph was generated by assuming typical experimental parameters for a cloud in our dipole trap. The cloud is of Gaussian shape with a peak density of 10^{12} atoms/cm^3 and a $1/e$ radius of 10 μm. The light intensity transmitted through the cloud was numerically simulated according to equation 4.5. From this the atom number, more precisely the area density, in the low and high intensity limit was calculated and compared with the actual value.

For an acceptable error in the deduced atom number of 5 percent assuming the low intensity limit, the imaging intensity must not be larger than 0.4 times the saturation intensity. The optical density is then on the order of 5 which means that only 0.6% of the imaging light is passing through the cloud, resulting in a bad signal to noise ratio on the camera. For high intensities the intensity should be larger than 25 times the saturation intensity in order to keep the error acceptably small. But the optical density is then smaller than 0.25 which means that the

absorption signal is quite faint and again this results in a bad signal to noise ratio. Ideally, the optical density should be close to one to reach best signal to noise behaviour, but then the error on the atom number is too large in both considered cases. Alternatively, it would be possible to reduce the absorption cross section by applying a detuning of the imaging beam, but due to dispersion this would lead to lensing effects in the cloud also degrading the image quality. This shows that, especially for dense clouds, other methods like phase-contrast imaging are much better suited to infer quantitative information. For this reason, a phase contrast imaging system for our setup is currently under construction.

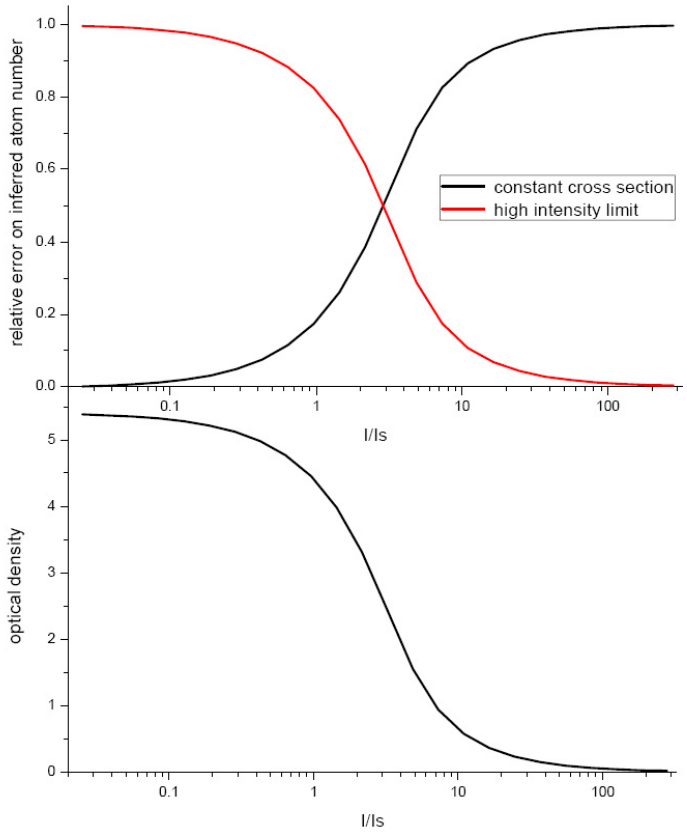

Figure 4.6: Upper panel: Relative error on the atom number by absorption imaging of a dense cloud in dependence of the intensity in units of saturation intensity for low and high intensity imaging. Lower panel: Optical density in dependence of the used intensity. For this graph typical experimental parameters have been chosen. The cloud is of Gaussian shape with a peak density of 10^{12} atoms/cm^3 and has a $1/e$ radius of 10 μm.

Imaging devices in our setup

In our setup, absorption imaging is performed in three different axes. Two in the horizontal plane and one in the vertical direction. The first horizontal imaging axis is perpendicular to the Zeeman-slower axis. The resolution in this axis is limited by the pixel size of the camera. As the Guppy F038B has an interlaced chip where two horizontal lines share one readout register, we have to bin two pixels in the vertical direction. Thus, the effective pixelsize on the camera is 8.4 μm$\times$19.6 μm, while the optical magnification is 1.7. The polarization of the imaging beam is perpendicular to the homogeneous magnetic field generated by the Feshbach coils. This reduces the absorption cross section by a factor of two compared to a properly circular polarized beam along the quantization axis ($\sigma = \sigma_0/2$ in the low intensity limit).

The setup of the other two imaging axes is not that straightforward as they are coincide with the MOT axes and the MOT light has to be separated from the light used for imaging. The optics for the MOT, the two horizontal imaging axes and the dipole trap are set up on a custom built breadboard such that all beams run at a height of 10 cm above the breadboard. An overview over the optics on this breadboard can be seen in figure 4.7.

The second horizontal imaging axis is perpendicular to the symmetry axis of the dipole trap. MOT and imaging beam have orthogonal polarizations and are overlapped on a polarizing beamsplitter. A $\lambda/4$ plate then turns the polarizations of both beams into counter-rotating circular polarizations. The polarization of the MOT beam is defined by the magnetic quadrupole field of the MOT, thus there is only one choice for the polarization of the imaging beam. Fortunately, the orientation of the circular polarization of the imaging beam is not important in this axis. Both possibilities reduce the absorption cross section by a factor of four compared to σ_0. On the one hand this reduces saturation effects for in-situ images of the cloud, as described before, on the other hand it leads to a reduction of the signal in time of flight images. After passing the chamber, a second $\lambda/4$ plate turns the polarizations of the beams back into orthogonal linear polarizations. The MOT beam is reflected at a wiregrid reflective polarizer (Moxtek, PPL05) while the imaging beam is transmitted. The shadow generated by the atomic cloud is imaged onto the CCD camera (Stingray, F033B) by a combination of a Gradium lens (Lightpath) with f=120 mm and a standard spherical lens with f = 400 mm. The optical resolution of the system is approximately 3 μm.

High resolution imaging in the vertical axis

One of our experimental goals is the preparation of a mesoscopic system consisting of a small and controlled number of ultracold fermionic ^{6}Li atoms. A major

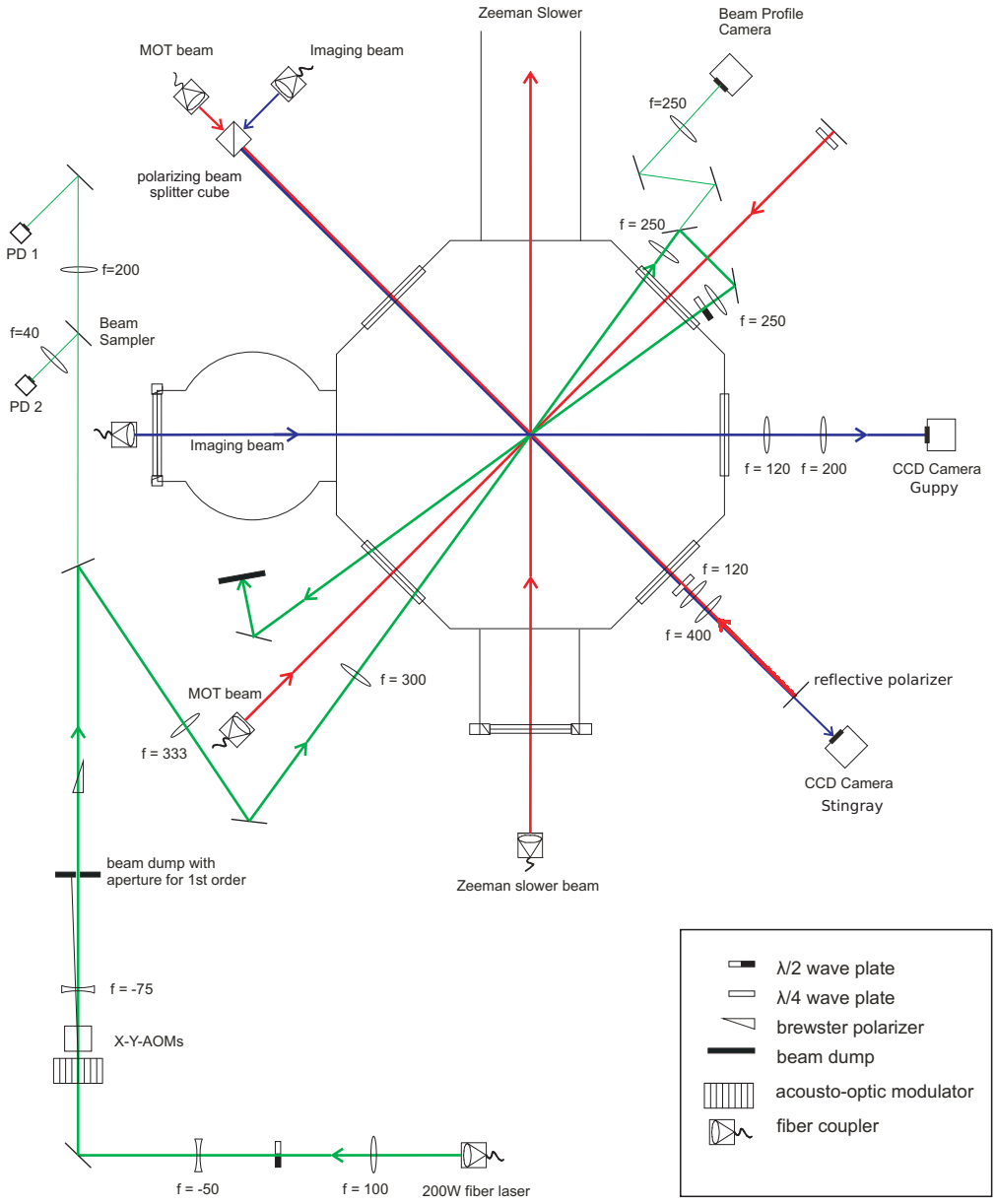

Figure 4.7: Top view on the optics surrounding the main chamber of the experiment. The optics for the two horizontal MOT beams and imaging systems as well as the dipole trap setup are shown.

challenge in such experiments will be the deduction of quantitative information about the system, for example the exact particle number. All this requires spatially

resolved detection of single atoms. The reentrant viewports described in section 4.1 allow to bring a light collecting objective with a large numerical aperture of 0.65 at maximum close to the atoms. The requirements for this objective are not easy to fulfill. On the one hand it should enable high resolution imaging at 671 nm, on the other hand its performance should also be diffraction limited at 1064 nm to focus an infrared beam to (sub)micrometer size (see section 4.3.3).

As a starting point, we chose an off-the-shelve aspheric lens (AL4532-B, Thorlabs) with a design wavelength of 780 nm. It has an effective focal length of 32 mm, a working distance of 24 mm and a clear aperture of 37.3 mm, resulting in a numerical aperture of 0.612. Clearly, its performance is only diffraction limited for 780 nm and we expect aberrations for our wavelengths. Thus, we do not use the full aperture of the lens but only the central part with one inch diameter, reducing the numerical aperture of the lens to 0.35, but also the amount of aberrations. If a diffraction limited performance of the lens is assumed the resolution would be 1.2 μm according to the Rayleigh criterion. Although this lens has not been optimized for our needs, it should give us an idea about basic problems and limitations before a custom objective is designed.

The imaging system in the vertical direction also coincides with one of our MOT axes. Thus, imaging and MOT beam must also be separated and the MOT beam retroreflected. We follow the same strategy as described above for one of the imaging axes in the horizontal plane, but as we were not aware of the Moxtek polarizers when the aspheric lens was built in, we chose a different solution.

A "dual brightness enhanced film" (DBEF, 3M) was directly laminated onto the plane side of the aspheric lens. These kind of films are used in LCD displays to recycle light with the wrong polarization which is normally absorbed in the polarizer. The DBEF film reflects the wrong polarization back to the light source where it is transformed again into both polarizations. This polarizing film has an amazingly large extinction ratio of 1:1000 over the whole visible spectrum.

The rest of the setup is identical to one of the horizontal planes. The helicity of the circular polarized imaging and MOT beams are different. After the chamber a λ/4 plate transforms the polarizations into perpendicular linear polarizations, of which one is reflected and one transmitted at the DBEF film. An overview of the setup can be seen in figure 4.8.

The imaging capability of the aspheric lens was tested in an external test setup which is schematically shown in figure 4.9. As a test target a pinhole (1-0.5+M-1, Dataoptics) with a diameter between 500 and 800 nm was used. The pinhole was illuminated with a laser beam with a wavelength of 671 nm and the image produced by the asphere was recorded on a CCD camera with a pixelsize of 4.65 μm (WinCam D, Dataray). The pinhole was mounted in a XY translating lens mount (LM1XY/M, Thorlabs) and the apsheric lens in a five axis mount (LP2A, Newport) which allows to adjust the angle of the lens with respect to the optical axis

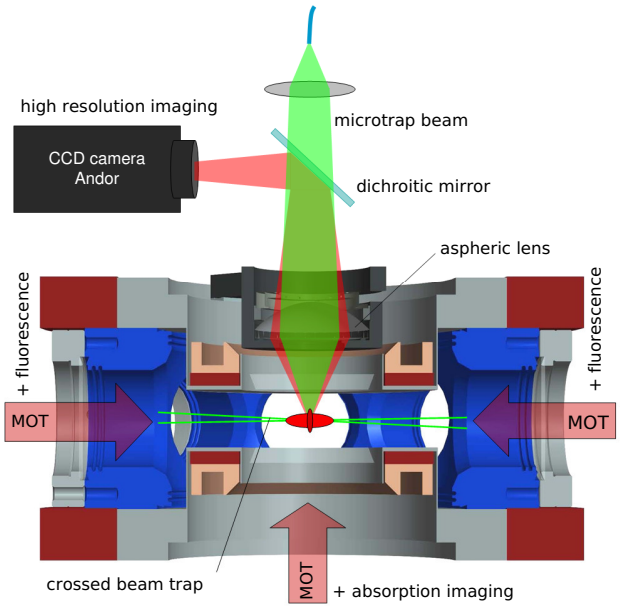

Figure 4.8: Side view of our experimental chamber. Shown are MOT and imaging beams (red), as well as the beams of the large volume dipole trap and the microtrap (green). A dichroic mirror is used to transmit the light for the microtrap and reflect the imaging beam towards the camera. The mount for the aspheric lens also houses a $\lambda/4$ plate (see text) and is directly attached to the reentrant viewport. The Feshbach coils and the cooler are mounted in the space around the windows.

and the transversal as well as the axial position.

The adjustment of the aspheric lens was done in the following steps: First a collimated laser beam was adjusted to run above a series of holes on the optical table and parallel to its surface. The beam path was then fixed with two irises and its position on the CCD camera was written down. The aspheric lens was installed between the two irises such that the faint backreflection from the flat surface coincides with the incoming laser beam which fixes the angles of the lens with respect to the optical axis. The transversal position of the lens was adjusted such that the focus of the transmitted beam is centered on the second iris behind the lens. Then the pinhole and the laser window simulating the vacuum viewport were put into the beam path. The image of the pinhole on the CCD is adjusted to the position of the laser beam which was written down before. The optimum distance between the pinhole and the asphere was beforehand determined with the optical design program OSLO (Lambda Research). The absolute position of the window is rather uncritical. In the real experimental setup it is fixed by the distance between the atoms and the viewport. If the atoms are in the center of the octagon this distance is 17.7 mm. For fine adjustment of the position of the CCD

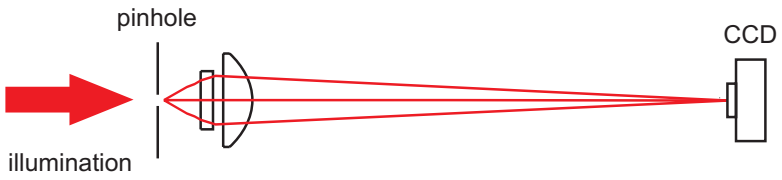

Figure 4.9: Schematic overview of the test setup for the aspheric lens. The pinhole (500-800 nm in diameter) was illuminated with a laser beam with a wavelength of 671 nm. The image produced by the asphere is recorded on a CCD camera with a pixel size of $4.65 \times 4.65\ \mu\text{m}^2$. The window of the reentrant viewport was simulated with a laser window made of the same material and with the same thickness.

camera it was mounted on a translation stage.

First the magnification of the imaging setup was measured by moving the pinhole in the transverse direction and recording its position on the CCD camera. This yielded a magnification of 10.8 which is 7% smaller than the value of 11.6 that was calculated in OSLO. This systematic error was observed in all measurements. Most likely reason is an uncertainty in the travel of the fine adjustment screws of the XY-lens mount in which the pinhole is mounted.

The resolution of the imaging system was estimated by analysing the size of the image of the pinhole on the CCD camera. In figure 4.10 an image of the pinhole is shown. This image was fitted with a two dimensional Gaussian with independent widths in x- and y-direction (see figure 4.10). Although aberrations are present in the image, the width of the central peak is fairly well described by the fit.

The fitted $1/e^2$ radii in the object plane are 0.8 μm in x-direction and 0.97 μm in y-direction. Further attempts to improve this result by better adjustment failed. OSLO simulations show that the adjustment of the angle of the lens and the window with respect to the optical axis are rather uncritical with a tolerance of 0.6 °. Also a possible of decentration of the lens up to 1 mm is not crucial. It turns out that the limiting factors are the tolerances of the lens itself, mainly the angle between the flat and the aspheric surface of the lens. A tilt of 3 arc min (as specified by the manufacturer) can explain the asymmetry observed in the test setup.

For an expected resolution of 1.2μm the finite diameter of the pinhole of less than 800 μm can be neglected and the image of the pinhole can be regarded as the point spread function of the imaging system. The point spread function of a diffraction limited imaging system is given by an Airy function. If this function is fitted with a Gaussian, the resulting $1/e^2$ radius is a factor of 1.49 smaller than the actual resolution. Thus, the resolution gained in the test setup can be estimated to be 1.2 μm in the x-direction and 1.4 μm in the y-direction.

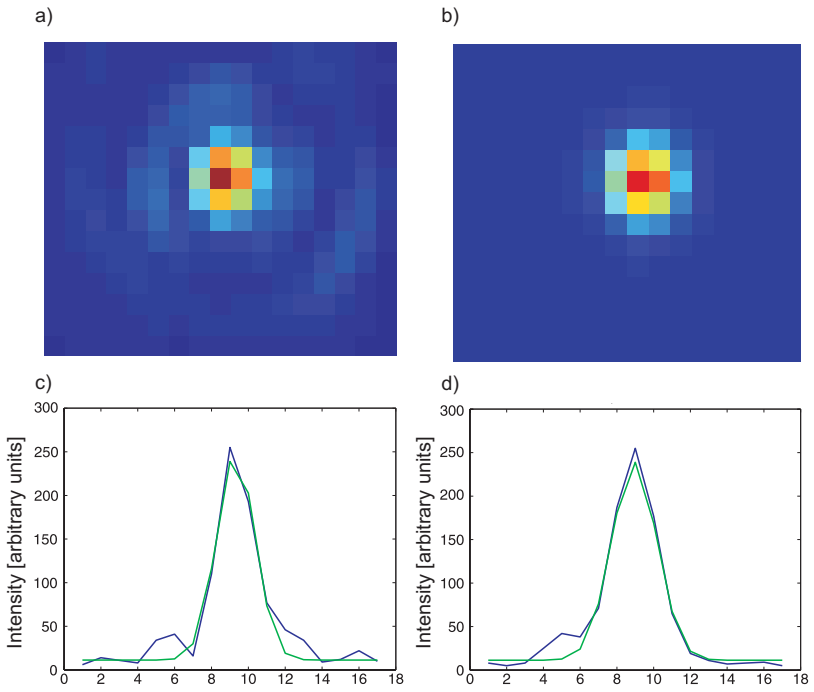

Figure 4.10: a) Image of the pinhole on the CCD camera. One pixel on the camera is $4.65 \times 4.65 \mu m^2$ large corresponding to $430 \times 430\,nm^2$ in the object plane. b) 2D Gaussian fit to the image c) Cut through the image (blue line)and the Gaussian (green line) fit in x-direction at the position of maximum intensity d) Cuts in in y-direction.

When these test measurements were performed unfortunately no $\lambda/4$ plate was available which is needed in the actual setup but according to simulations with OSLO, the waveplate does not alter the performance of the system significantly. A more serious limitation is the reflective polarizing film laminated on the flat surface on the lens. Its surface is not perfectly flat and reduces the optical resolution by about a factor of two.

Figure 4.11 shows an absorption image of the crossed dipole trap acquired with the aspheric lens after its implementation into the setup.

4.3 Optical dipole traps

It is necessary to implement a further cooling and trapping stage following the magneto-optical trap. On the one hand the temperature and phase space density reached in the MOT are not sufficient for our experiments, on the other hand the MOT does not provide a conservative potential for the atoms, due to ongoing

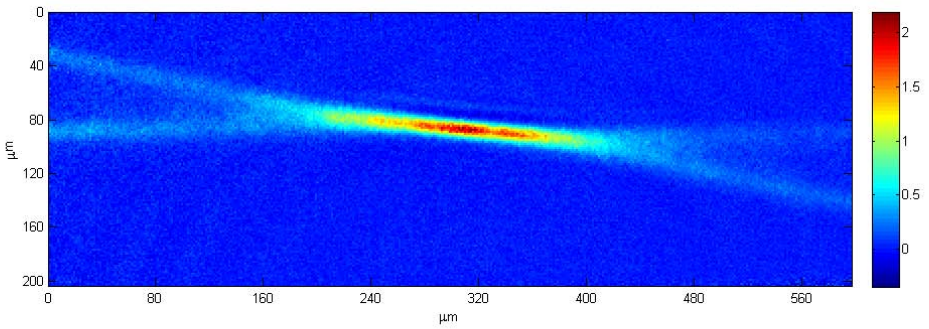

Figure 4.11: Image of the crossed dipole trap acquired with the aspheric lens. Residual atoms in the single beams of the trap are nicely visible.

absorption and emission of photons. This makes it for example impossible to prepare the atoms in a desired internal state, which is essential for most of our measurements. A nearly conservative potential is provided by an optical dipole trap. Such a trap is set up by a focused laser beam, providing a potential, which is directly proportional to the intensity profile of the beam. This is rather simple to understand, as the electric field of the laser induces an electric dipole moment in the atoms, that is proportional to the electric field strength ($\vec{p} \propto \alpha \vec{E}$, where α is the polarizability of the atoms). The potential energy of this dipole in the field is also proportional to $\vec{E}$, thus $U \propto \vec{E}^2 \propto I$. The sign of the polarizability depends on the detuning of the trapping beam from the atomic resonance. For red detuning α is positive and the atoms are attracted towards regions of high intensity which is the most common application of dipole traps. A more rigorous analysis yields the analytic expressions for the trapping potential and the scattering rate of photons [Gri00]

$$U_{dip}(\mathbf{r}) = -\frac{3\pi c^2}{2\omega_0}\left(\frac{\Gamma}{\omega_0-\omega}+\frac{\Gamma}{\omega_0-\omega}\right) I(\mathbf{r}) \tag{4.11}$$

$$\Gamma_{sc}(\mathbf{r}) = -\frac{3\pi c^2}{2\omega_0}\left(\frac{\omega}{\omega_0}\right)^3\left(\frac{\Gamma}{\omega_0-\omega}+\frac{\Gamma}{\omega_0+\omega}\right)^2 I(\mathbf{r}). \tag{4.12}$$

Scattering of photons leads to heating of the atoms and must be suppressed. As the scattering rate is inversely proportional to the square of the detuning while the potential scales only linear, it is favourable to choose a far off-resonant laser. In our setup we use a 200 W Ytterbium doped fibre laser (YLR-200-LP, IPG photonics) at a center wavelength of 1070 nm, which is far red-detuned with respect to the transition wavelength of 671 nm. Ideally, the intensity of a laser beam is de-

scribed by Gaussian beam optics. In radial direction the intensity is of Gaussian shape

$$I(r,z) = I_0 \exp\left(-\frac{2r^2}{w(z)^2}\right) \tag{4.13}$$

where $w(z)$ is the $1/e^2$ radius of the beam and $I_0 = 2P/w(z)^2$ is the maximum intensity at laser power P. The minimum beam radius w_0 is also called the waist of the beam. The divergence of the beam is given by

$$w(z) = w_0\sqrt{1+\left(\frac{z}{z_R}\right)^2} \tag{4.14}$$

where $z_R = \pi w_0^2/\lambda$ is the Rayleigh range. For $r \ll w_0$ and $z \ll z_R$ the resulting potential can be approximated by a harmonic oscillator with trapping frequencies

$$\omega_r \propto \frac{\sqrt{P}}{w_0^2}, \qquad \omega_z \propto \frac{\sqrt{P}}{w_0^3}. \tag{4.15}$$

The aspect ratio is then

$$\frac{\omega_r}{\omega_z} = \frac{\sqrt{2}\pi w_0}{\lambda}. \tag{4.16}$$

4.3.1 Setup of the large volume dipole trap

In our setup two dipole traps are implemented. A large volume trap with a beam waist of 50 μm and a small microtrap with a waist of $\sim$3 μm. The microtrap will be described in section 4.3.3.

After the MOT phase the atoms are transferred into the large volume trap for further evaporative cooling. A complete overview of the setup for this trap can be seen in figure 4.7. After the fibre collimator the beam size is reduced to $\sim$1 mm to match the aperture of two AOM's (3110-197, Crystal Technology). The AOM's are mounted perpendicular to each other and are used for intensity stabilization of the beam and as a beam steering device for the generation of arbitrary potentials (see section 4.3.2). Afterwards the beam is expanded to a diameter of about 4 mm and focused with a f = 300 mm lens into the chamber. As the aspect ratio of a single beam with a waist of 50 μm is $\sim$100, which is too large for our experiments, we pass the beam twice through our chamber and cross the reflected with the incoming beam under an angle of $\sim$11.9°. This results in a cylindrically symmetric trap with an aspect ratio of 1:10. We have observed that the lifetime of the atoms in the trap is strongly dependent on the relative polarization of both beams. The reason for this observation is not yet clear. Best results are obtained when the polarization of both beams is orthogonal to each other. For this reason

the polarization of the incoming beam is cleaned by a Brewster polarizer and the polarization of the reflected beam is turned by 90° using a $\lambda/2$ waveplate. For intensity stabilization some light transmitted through a mirror is detected by two photodiodes. Using a digital PID loop which is implemented in the computer control of our experiment, the signal on the photodiode is fed back to the power of the sound wave in the AOM Crystal. The two photodiodes are used for two different intensity regimes, one at high power and one at low power, as the dynamic range of one photodiode is too small.

Working with high power lasers makes it necessary to consider thermal effects in all optical components. Absorption in the material leads to heating and consequently to a change of the refractive index. This can have devastating effects on the intensity profile of the beam. We try to minimize this effect by using Fused Silica lenses and large beams wherever possible, but we still observe thermal effects, when the laser runs at full power [Lom08]. It seems that optical lensing mainly occurs in the AOMs and the viewports of the vacuum chamber. For this reason the 200 W are only used for transferring the atoms into the dipole trap. After the transfer the laser power is ramped down to 40 W in order to reduce thermal effects.

Calibration of trapping frequencies

For quantitative measurements the trapping frequencies of the trap have to be known, as they for example determine the density of particles at a given atom number. For calibration of these frequencies two methods are used. The first one is called parametric heating and is based on a modulation of the trapping intensity. This results in a modulation of the spring constant of the trap and when the modulation frequency matches twice the trapping frequency, loss of atoms from the trap is enhanced. In a simple picture, the atoms get a kick at both of their classical turning points which leads to an increase of their momenta, until their kinetic energy is high enough to leave the trap. In the experiment both the atom number and the temperature of the atoms in dependence of the modulation frequency is determined after a fixed number of kicks. An exemplary outcome of such a measurement is shown in figure 4.12.

Note that maximum trap loss and maximum heating do not occur for the same modulation frequency of the trapping beam power. This is due to the Gaussian shape of the trapping beam. When the atoms are heated, they sample also the outer parts of the trapping potential. In this region the Gaussian is flatter than a parabola which reduces the trapping frequency and shifts the maximum trap loss to lower modulation frequencies. Therefore the temperature of the atoms provide a better measure of the trapping frequency which is determined from the expansion of the cloud after switching off the trap.

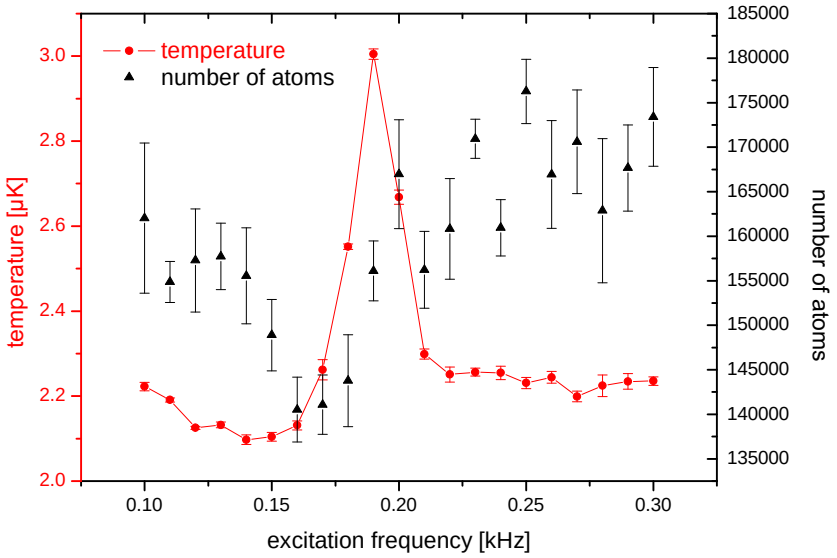

Figure 4.12: Parametric heating measurement of the axial trapping frequency at a laser power of 760 mW. The error bars indicate the statistical error of five independent measurements.

The second method is the excitation of the dipole or compression mode of the cloud, which yields more accurate results. Dipole oscillations can for example be excited by applying a magnetic field gradient, which moves the cloud from the center of the trap. Fast switch-off (compared to the trapping frequency) of the gradient causes the center of the cloud to oscillate in the trap with the trapping frequency. The so-called compression mode can be excited by a sudden change of the trapping frequency. The size of the cloud will then oscillate with twice the trapping frequency. This measurement has to be performed with a cloud in the normal (thermal) phase, as a gas in the hydrodynamic regime will oscillate with another frequency [Pit03]. Both types of excitations can be directly observed by in-situ absorption imaging or alternatively after time-of-flight. Figure 4.13 shows the oscillation of the width of the cloud in the long axis after excitation by a sudden change of the trapping beam power.

4.3.2 Time averaged potentials

As mentioned before, using the two AOMs as a beam steering device enables to generate nearly arbitrary intensity profiles in the focus and thus arbitrary potentials

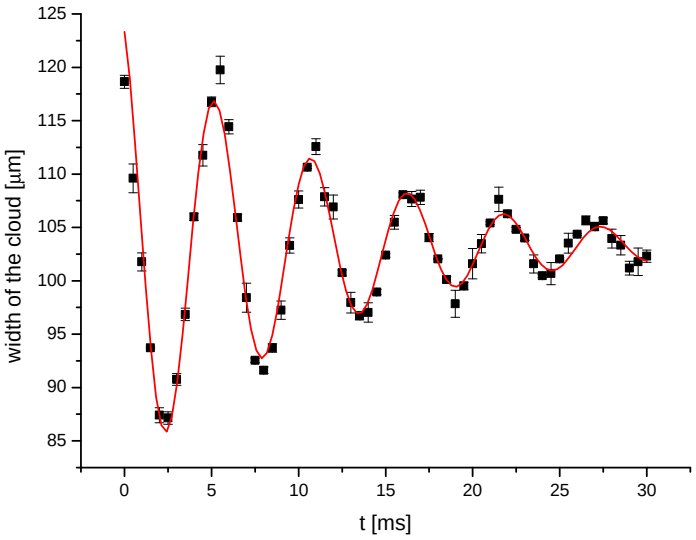

Figure 4.13: Oscillation of the cloud width in the long axes of the trap after sudden change of the trapping frequency. The beam power was 640 mW. The red line is a damped sine fit to the data.

for the atoms. Prerequisite is that the beam is moved fast enough compared to the trapping frequencies. Then the atoms experience the time averaged intensity profile of the moving beam. The deflection angle of the first diffraction order generated at the AOM is dependent on the RF frequency applied to the crystal. Thus, by changing the RF frequency the beam pointing can be changed. A sketch of the ray trajectories is shown in figure 4.14.

Standard matrix methods [Sal91] allow to calculate displacement and angle of the beam in the focus

$$\Delta x = \alpha \frac{f_1 f_3}{f_2} \qquad \alpha^* = -2\alpha \frac{f_2}{f_3}. \tag{4.17}$$

One of the easiest applications of this technique is to increase the waist of the trapping beam. This makes it possible to reduce the trapping frequencies of the trap, while the trap depth is kept constant. As the density of a trapped atomic cloud is proportional to the third power of the mean trapping frequency, this allows to study density dependent phenomena. A density dependent loss for example can be slowed down by this technique and shifted to timescales that are observable in the experiment.

Let us assume the beam of the dipole trap has a waist of σ_0 and it is desired to increase its size to σ_{drawn}. How must the beam be moved and its intensity be modulated, in order to draw a larger Gaussian?

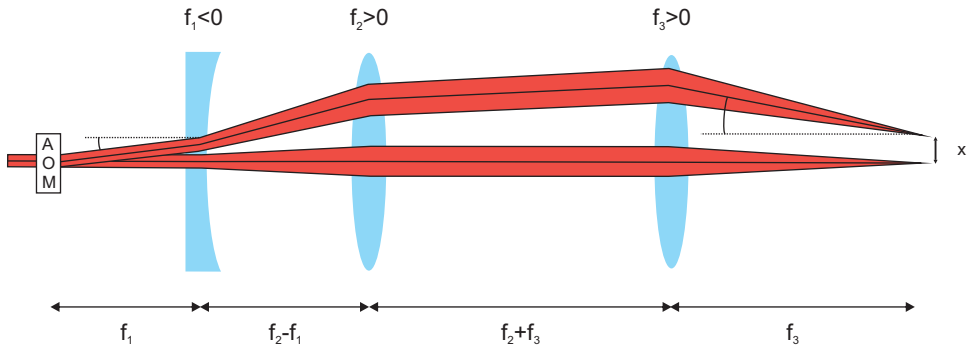

Figure 4.14: Ray trajectories of undeflected and deflected beams after the AOM. Angles and distances are not to scale for better visibility.

If the position of the focus is changed in the radial plane and its intensity is modulated by some function $I(r)$, the resulting intensity pattern is the convolution of the intensity profile of the beam $I_{beam}(\mathbf{r})$ and $I(\mathbf{r})$

$$I_{drawn}(\mathbf{r}) = I_{beam}(\mathbf{r}) * I(\mathbf{r}) \tag{4.18}$$

The convolution of two Gaussians with waists w_0 and w results again in a Gaussian with waist

$$w_{drawn} = \sqrt{w_0^2 + w^2} \tag{4.19}$$

Thus, the intensity of the moving beam has to be modulated by a Gaussian with waist $w = w_{drawn}^2 - w_0^2$. In doing so, the dependence of the diffraction efficiency of the AOM on the applied frequency must be compensated

The experimental procedure is as follows: First the position of the beam and its intensity, depending on the applied RF frequency is determined. This can easily be done by using a CCD camera. A spacing of half a waist of the original Gaussian between the measured points is sufficient. In order to draw the intensity pattern the beam jumps to these points while its dwelling time at each point is given by the amplitude of the Gaussian with waist w and the diffraction efficiency of the AOM. In figure 4.15 the beam profile of the original beam and the drawn Gaussian with doubled waist is shown.

In radial direction the beam has the desired Gaussian shape, while the axial intensity distribution was not discussed so far. Along the beam the resulting intensity pattern is also given by the convolution 4.18. Away from the focus the beam stays Gaussian and its waist expands according to 4.14. It follows that the waist of the

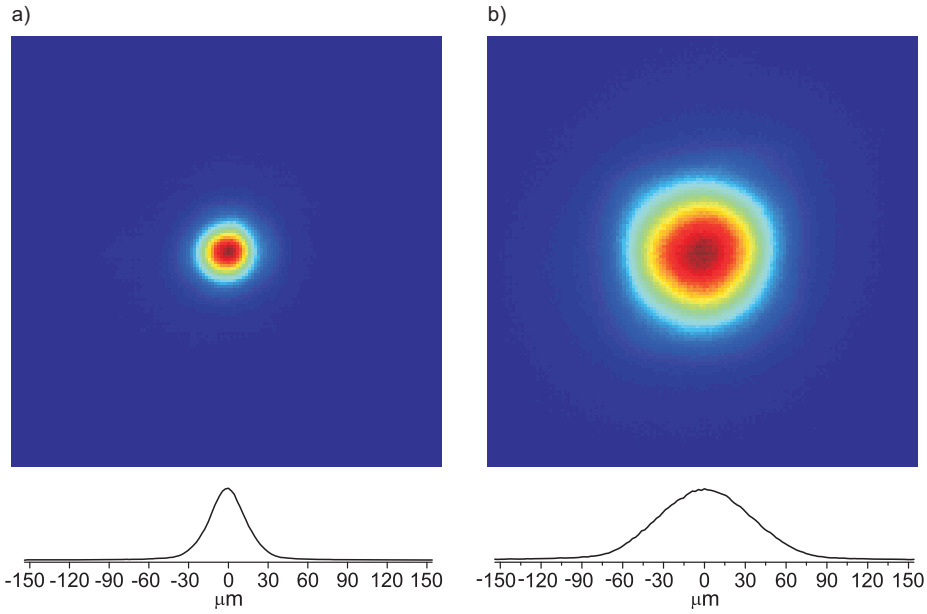

Figure 4.15: a) Radial intensity profile of the original trapping beam with a waist of about 30 mum. In the meantime parts of the dipole trap setup were changed resulting in a smaller focus. b) Radial profile of the drawn Gaussian with a waist of about 60 μm.

drawn beam expands like

$$w_{drawn}(z) = w_{drawn}(0)\sqrt{1 + \left(\frac{w_0}{w_{drawn}(0)}\right)^2 \left(\frac{z}{z_R}\right)^2} \tag{4.20}$$

where z_R is the Rayleigh range of the original trapping beam.

An expansion of radial as well as axial intensity profile to second order shows that the aspect ratio of the drawn trap is the same as the aspect ratio of the original trap.

These considerations do not take into account that the angle of the beam with respect to the optical axes also changes while the beam is moved (see figure 4.14). For a maximum deflection of $\pm 200\,\mu$m the angle is seven arcseconds in our lens configuration, corresponding to 0.4°. Over the axial extension of the cloud which is less than $\pm 500\,\mu$m[1] this corresponds to a shift of the beam center of 3 μm at maximum, which is less than a tenth of the beam waist and thus negligible.

In our setup the RF frequency for the AOM's is provided by two VCOs (Z-Communications V110-ME01) with a large modulation bandwidth of 10 Mhz.

[1]The size of the cloud is determined by the crossing region of the beams.

This is fast compared to the highest trapping frequencies ($\sim$20 kHz) achieved in our trap, and ensures that the atoms experience the time-average of the intensity distribution, while the trapping beam is moved. The tuning voltage for the VCOs is supplied by two arbitrary waveform generators (Agilent, 33220A). Soon, these waveform generators will be substituted by Direct Digital Synthesizers (DDS) as they offer a higher flexibility.

4.3.3 The microtrap

The setup was built to fulfill the requirements that are essential for the preparation of a finite ensemble of deeply degenerate fermionic atoms with particle numbers on the order of one hundred or even less. To study the properties of such systems it is crucial to have full control over the atom number in the trap. Ultimate goal is to prepare a Fock state with a defined number of particles on demand. This requires on the one hand the ability to prepare a deeply degenerate Fermi gas with ideally no unoccupied states up to the Fermi energy and on the other hand the possibility to control the number of quantum states in the trapping potential, see chapter 7. Both challenges can be overcome by using a very tight optical dipole trap, formed by a focused laser beam with a waist in the (sub)micrometer range. In the following such a trap is denoted by microtrap. Using this microtrap as a so-called dimple [Pin97, SK98] that is in thermal contact with the large volume trap, it should be possible to reach high degeneracy. The high trapping frequencies, and thus the large separation of energy levels, should allow to control the number of quantum states in the trap for example by applying an external magnetic field gradient (see figure 7.1). In our current setup the microtrap is realized with the same aspheric lens that is used for imaging in the vertical axis (see section 4.2.4). The setup and tests about the performance are described in detail in the diploma thesis by Gerhard Zuern [Zue09], thus only a short summary is given here. The light for the microtrap is provided by an Ytterbium doped 5 W fiber laser (YLM-5-LP, IPG Photonics) with a central wavelength of 1064 nm. As the lens has a design wavelength of 780 nm aberrations are expected. The optimum beam parameters to minimize aberrations, for example the collimation of the incoming beam as well as spot size on the lens have been optimized beforehand using the optical design software OSLO (Lambda Research). A schematic overview of the lens configuration can is shown in figure 4.16.

In order to clean the profile of the beam, it is guided through a single mode polarization maintaining optical fibre. A special outcoupler [Zue09] was built satisfying the following requirements: As the distance of the aspheric lens to the reentrant viewport is fixed, it must be possible to align the position of the focus in vertical direction for optimum overlap with the large volume dipole trap. This is accomplished by a movable collimating lens (C560TM-B, Thorlabs) after the

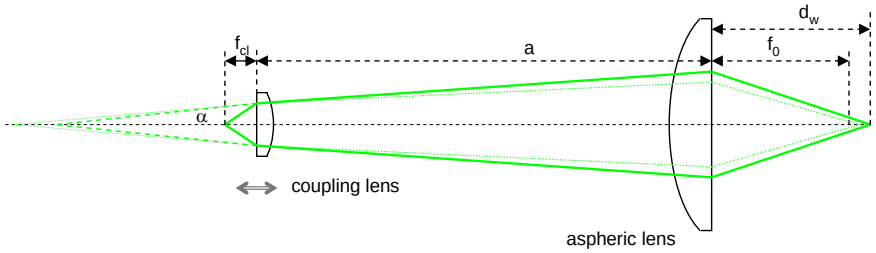

Figure 4.16: Schematic overview over the lens setup for the microtrap.

fibre. The position of the coupling lens with respect to the end of the fibre determines the divergence angle of the beam and thus the position of the focus in the main chamber. Naturally, this changes the waist of the beam on the surface of the aspheric lens. To compensate for this, the distance between outcoupler and aspheric lens can be changed by means of a translation stage. Included in the outcoupler is a glass window that picks up a small part of the light intensity which is recorded on a photodiode for intensity stabilization. In addition, this window compensates for the astigmatism introduced by the dichroic mirror which is used for reflecting the imaging beam to the camera (see figure 4.8).

Before the microtrap beam was integrated into the experimental setup, detailed test measurements on the performance of the lens system have been done [Zue09]. The waist of the beam and its divergence have been determined in dependence of the divergence of the incoming beam and the waist on the surface of the aspheric lens. Optimum results were $w_0 = (2.98 \pm 0.26)\,\mu m$ for the waist and $z_R = (26 \pm 5)\,\mu m$ for the Rayleigh range, which is in good agreement with Gaussian beam optics and results in a trap aspect ratio of 1:12.5. Trapping frequencies of $\omega_r = 2\pi \times 8\,kHz \times \sqrt{P}$ and $\omega_z = 2\pi \times 650\,Hz \times \sqrt{P}$, where P is the beam power in mW, are expected. After the implementation of the microtrap into the existing setup the trapping frequencies were experimentally determined. In axial direction this was done by adiabatically applying a magnetic field gradient which shifts the center of the trap in axial direction. After suddenly switching off the gradient the cloud undergoes dipole oscillations which can be recorded by absorption imaging. In radial direction a compression mode was excited by switching off the microtrap beam for $10\,\mu s$ and recording the cloud size as a function of time after the excitation. The cloud size then oscillates with twice the corresponding trapping frequency. These measurements yielded $\omega_r = 2\pi \times 3.79\,kHz \times \sqrt{P}$ and $\omega_z = 2\pi \times 160\,Hz \times \sqrt{P}$, which differ significantly from the expected values given above. Also the observed aspect ratio of 1:24 is twice the expected value. The reason for this discrepancy is not yet fully understood. The measured values are consistent with a waist of 3.6 μm, which is within a possible range due to mis-

alignment and an additional astigmatism with a focus shift of 50 μm. Up to now this is only a guess and needs further investigation, as astigmatism should actually be compensated in the current setup.

4.4 Feshbach coils

In section 2.3 it was shown that interaction in ultracold gases can be tuned by applying an external homogeneous magnetic field. As in ^{6}Li the Feshbach resonances occur at rather high fields it is necessary to put the field coils as close as possible to the atoms. This reduces the current needed for generating the field and thus the power consumption in the coils. A second issue concerning the design of the coils is to keep the inductance as low as possible such that fast switching of the current is possible. As shown in figure 4.8 the coils are mounted in the space between the window and the outer rim of the reentrant viewports. The coils are made of enamelled copper wire with a rectangular cross section of $1 \times 5\,\mathrm{mm}^2$ and consist of a single layer with 15 windings. The coils itself are hand-wound and bonded with an unfilled epoxy (EPO-TEK 353ND) which allows easy machining of the coils in the later production process. Inner and outer diameter of the coils are 58 mm and 94 mm respectively and the distance between the coils is 32 mm. The calculated magnetic field shape for a current of 210 A is shown in figure 4.17.

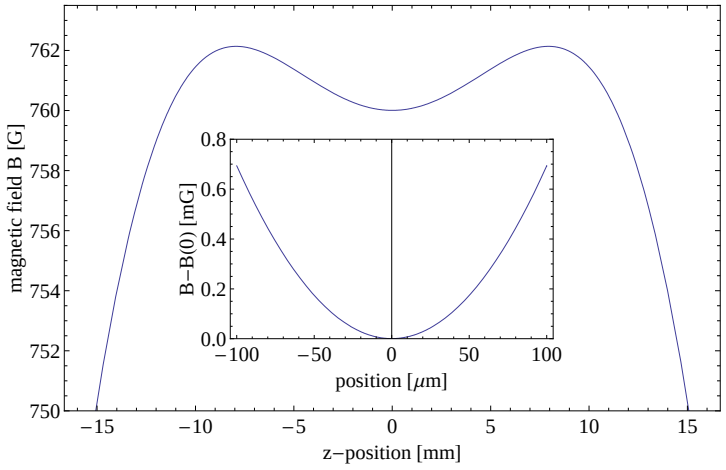

Figure 4.17: Calculated axial magnetic field of our Feshbach coils for a current of 210 A. Although there is a local minimum in the center of the two coils the inhomogeneity of the field over the atomic cloud is only on the order of mG.

As the coils are not in perfect Helmholtz configuration a local minimum in the axial magnetic field occurs, which is on the order of a few mG. In radial direction

the magnetic field has a local maximum whose curvature is half of the value in axial direction. In most cases this curvature of the magnetic field is negligible. As ^{6}Li atoms are high field seekers, for fields larger than 30 G, the field curvature acts as an additional trapping potential in radial direction and as an antitrap in axial direction. For very shallow optical dipole traps this influence of the magnetic field has to be taken into account. The magnetic field strength generated at a current of 210 A is $\approx$ 760 G. For magnetic fields larger than 1400 G it is necessary to run currents up to 400 A in the field coils. The corresponding power consumption is then about 3 kW which requires an efficient cooling system. For this a copper heat sink was designed and an elaborate manufacturing procedure was established [Zue09]. In Figure 4.18 a draft of the heat sink with the connectors for cooling water and electric current is shown.

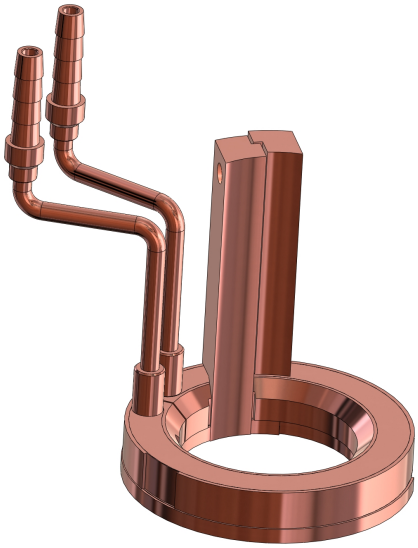

Figure 4.18: Heat sink for the Feshbach coils with connectors for cooling water and electric current.

For efficient cooling of the coils the heat contact between the coil and the heat sink is the most critical issue. To improve the thermal contact several steps have to be taken while building the coils. After winding the coils the isolating film on one side of the coil has to be removed on a lathe. It is crucial that the surface of the coil is flat and no short circuits between the single windings occur. The glue with which the coils are attached to the heat sink must be chosen carefully. It must be electrically isolating but a high thermal conductivity is required. A diamond filled epoxy Prima-Bond ME7159 (AI Technologies) turned out to be the best choice in a set of test measurements. Due to the high filling of this epoxy its viscosity is rather high. Therefore excessive glue and air bubbles cannot escape from the

space between coils and heatsink during the bonding process. A good thermal contact can only be reached when the glue layer is as thin as possible (but still thick enough to avoid electric contact) and free of air bubbles. For this reason, a 0.3 mm deep grid with a spacing of 3 mm was eroded from the surface of the copper cooler. This grid acts as a reservoir to which excessive glue and air bubbles can escape during the bonding process. All this effort payed off as it is possible to run 300 A continuously through the coils generating a field of 1130 G. 400 A corresponding to 1510 G are possible for 2.5 s before the temperature exceeds 100 °C. The temperature of the coils is monitored continuously by measuring their resistance. For this an integrated microcontroller board (Arduino Diecimila) is used that disables the output of the power supply, when the resistance grows too large.

The electric connectors are soldered to the coils and electrically isolated from the copper cooler. Instead of ordinary tin-solder, we used an indium based solder whose electric conductivity is a factor of 1.4 higher. Another advantage of indium is that the melting point is lower compared to ordinary solder and thus the temperature during the soldering process can be reduced which reduces the risk of damaging the glue layer between coils and cooler. It is crucial to put both connectors as close as possible, as over- or underwinding leads to an asymmetry in the magnetic field. The current flowing through the connectors also generates a magnetic field at the place of the atoms. This field contribution is cancelled by winding the two coils in opposite direction and placing the connectors of top and bottom coils on top of each other. For more details on the manufacturing process of the coils and their performance please refer to [Zue09].

In order to change the field from Helmholtz to anti-Helmholtz configuration the current in one of the coils can be reversed using a so-called H-Bridge [Koh08]. This is of special use during the transfer of atoms from the MOT to the dipole trap. In this stage of the experiment the quadrupole field is generated by the Feshbach coils to compress the atomic cloud which enhances the transfer efficiency. Stabilization of the current in the coils is done by a digital PID loop implemented in our experiment control (see section 4.6). The current is measured using a current transducer (Danfysik, Ultrastab 866-600) and the output of the PID loop is fed back onto the output voltage of the power supply (Delta Elektronika, SM15-400).

4.5 Manipulating spin states - the radio frequency (RF) setup

Transition between magnetic sublevels in the ground state of ^{6}Li can be induced by applying radio frequency (RF) fields to the atoms. For our experiments on

three component Fermi gases the RF setup is the essential tool to prepare the sample (see section 6.2). Furthermore, radio frequency spectroscopy is a very precise method to determine the state of the system under study. It allows for example the measurement of binding energies of Feshbach molecules (see section 5.4) or the study of pairing in a BCS like gas [Chi04a, Sch08]. Most experiments are performed with the lowest three states which have an energy splitting of about 80 MHz (see figure B.2)

In principle the RF setup consists of three components: A radio frequency source, an amplifier and an antenna. An overview of the setup is shown in 4.19.

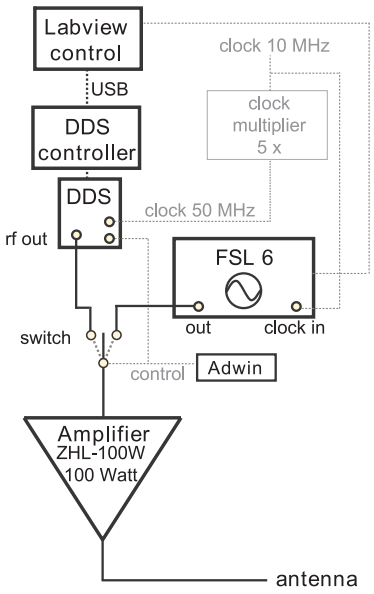

Figure 4.19: Setup for radio-frequency generation. Central part of the setup is a direct digital synthesizer (DDS) system. For frequencies higher than 150 Mhz the generator output of our spectrum analyzer is used. Both devices are synchronized by a 10 Mhz clock signal which has to be multiplied by a factor of five for the DDS.

The central part is a Direct Digital Synthesizer (DDS) system using an AD9854 chip from Analog Devices. It is capable of generating sine signals up to a frequency of 150 Mhz at an output power of 7 dBm and can be programmed via an onboard micro controller (ATmega 128-16AC). The control software is directly implemented in our experimental control and allows to generate sequences of RF pulses and frequency sweeps at wish which are started by an external trigger signal. For high radio frequencies, the generator output of our spectrum analyzer (FSL6, Rohde & Schwarz) is used. Both devices are synchronized using a 10 Mhz

clock signal that is provided by an Agilent arbitrary waveform generator which is used for controlling the radio-frequency in the dipole trap AOMs (see section 4.3.2). For amplification of the radio-frequency signals we use a 100 W amplifier (ZHL-100W, Minicircuits). An overview of the RF setup is shown in figure 4.19.

For the preparation of the three-component mixture, two frequencies are simultaneously needed which match the $|1\rangle - |2\rangle$ and $|2\rangle - |3\rangle$ transitions. These can be generated by setting the spectrum analyzer to the midfrequency of the $|1\rangle - |2\rangle$ and $|2\rangle - |3\rangle$ transition frequencies and modulating sidebands with half the difference frequency onto this signal. The signal for sideband modulation is provided by the DDS.

The purpose of the antenna is to generate an oscillating magnetic field at the place of the atoms. Irradiation of a radio frequency wave is rather undesirable, as this can lead to uncontrolled disturbances in other parts of the experimental setup. Therefore, our antenna consists of a single loop made of copper wire (diameter 1 mm), with a diameter of about 40 mm. For a large oscillation amplitude of the magnetic field, the current in the loop has to be maximized. This is done by tuning the resonance frequency to the desired value (in our case about 80 MHz) and matching its impedance to the output impedance of the amplifier which is 50 Ω. In our setup this is done by a simple L section consisting of two capacitors. Due to the low resistance of the antenna impedance matching is difficult and is done as good as possible. For more details on the antenna design please refer to [Wen09b]. The antenna is placed under an angle of about 45° below the main chamber of our experiment. It surrounds the vertical MOT beam and has a distance of less than 10 cm to the atoms. Rabi frequencies of up to 2 kHz are reached, mostly limited by the distance between the antenna and the atoms.

4.6 Computer control of the experiment

The experimental control is realized by a real-time system (Adwin Pro II, Jäger Messtechnik) with sixteen 16 bit analog outputs, eight 18 bit analog inputs and 32 digital I/O channels. The experimental sequence is prepared in a LabVIEW (National Instruments) program, that allows to time events on each analog or digital channel relative to each other. All timing and output values can be entered directly or in form of variables. The program generates a list with an entry for every point in time when the state of one channel is changed. The list is then transferred via LAN to the memory of the CPU module in the real time system. Implemented in this module is a DSP processor with a clock rate of 300 MHz and 256 MB DRAM. On this processor runs a program written in ADbasic that evaluates the list transferred from the LabVIEW program and changes the state of the respective channels at the desired point in time. Currently, the state of an analog

channel can be changed every 10 μs, corresponding to a bandwidth of 100 kHz. On the digital I/O card there is an additional FPGA (TiCo), that allows to update the the digital channels with a bandwidth of 1 MHz.

Automated loops allow to change experimental parameters automatically in each run of the experiment. This makes experiments much easier and less susceptible to errors.

A special feature of our experimental control is the possibility to implement digital PID loops. The setpoint for an experimental parameter is set in the LabVIEW program. The actual value is recorded by one of the analog inputs and from the difference to the set value a correcting variable is calculated and fed back via an output channel. The parameters for proportional, integral and differential part of the regulator are directly set in the ADbasic program. Such a digital regulator has several advantages. To stabilize one experimental parameter different detectors can be used to increase the dynamic range. This is for example done to stabilize the light intensity in the optical dipole trap (see section 4.3). Furthermore, sudden jumps can be realized by opening the loop for a short time and setting a desired output value. Then the loop is closed again with a new setpoint.

Chapter 5

Ready for experiments: Preparation of a BEC of $^6Li_2$ molecules

This chapter is devoted to the realization of Bose-Einstein condensation of $^6Li_2$ molecules in our experimental setup. After one year of building the preparation of our first Bose-Einstein condensate (BEC) showed that the setup was ready for new experiments with ultracold atoms. A BEC of $^6Li_2$ molecules was for the first time prepared in 2003 [Joc03b, Gre03, Zwi03].

This chapter is organized as follows: After a brief introduction into the theory of Bose-Einstein condensation in ideal gases and the effects of interactions, the evaporative cooling scheme used during the experimental sequence is presented. When the temperature during this cooling procedure drops below the binding energy of the molecules, molecules are formed by three-body recombination. The formation of these molecules and their experimental observation will be explained. By continued evaporation these molecules are further cooled and as soon as the temperature drops below the critical temperature for Bose-Einstein condensation a condensed phase emerges. The observation of this condensed phase in our experimental setup is described in the last section of this chapter.

5.1 Bose-Einstein condensation in ideal gases

In a system of non-interacting bosons the mean occupation number per state in thermal equilibrium is given by the Bose-Einstein distribution

$$f(E) = \frac{1}{e^{\frac{(E-\mu)}{k_B T}} - 1} \tag{5.1}$$

where μ and T are the chemical potential and the temperature of the sample respectively. Thermodynamic properties of this system can be calculated by inte-

grating over the density of states which depends on the system under study times the Bose-Einstein distribution function. For example, the number of particles in the system is given by

$$N = \int dE\, g(E) f(E). \tag{5.2}$$

In the following we restrict ourselves to bosons confined in an optical dipole trap whose potential can in most cases be approximated by a three-dimensional harmonic oscillator with trapping frequencies ω_x, ω_y and ω_z. The density of states in a harmonic oscillator is

$$g(E) = \frac{E^2}{2\hbar\bar{\omega}^3} \tag{5.3}$$

where $\bar{\omega} = (\omega_x\omega_y\omega_z)^{1/3}$. In the thermodynamic limit the energy offset is usually chosen such that the ground state of the system corresponds to $E = 0$. The density of states vanishes then at zero energy which means that the ground state population is not included in the integral 5.2. It therefore includes only the number of particles in the excited states. For a three-dimensional harmonic oscillator potential the integral in 5.2 is finite which means that only a finite number of particles fit into the excited states. Additional atoms have to reside in the ground state and form the Bose-Einstein Condensate. The critical temperature for condensation is the lowest temperature at which the total number of particles can be accommodated in the excited states.

$$N = N_{ex}(T_c, \mu = 0) = \frac{1}{2(\hbar\bar{\omega})^3} \int_0^\infty \frac{dE\, E^2}{e^{E/k_B T_c} - 1} \tag{5.4}$$

Solving the integral results in[1]

$$k_B T_c = \frac{\hbar\bar{\omega} N^{1/3}}{[\zeta(3)]^{1/3}} \approx 0.94\hbar\bar{\omega} N^{1/3} \tag{5.5}$$

where $\zeta(s) = \sum_{n=0}^{\infty} 1/n^s$ is the Riemann Zeta function. At temperatures below T_c the occupation of the ground state is given by

$$N_0 = N\left[1 - \left(\frac{T}{T_c}\right)^3\right]. \tag{5.6}$$

At $T = 0$ all atoms are in the ground state and have the same wavefunction. In the case of non-interacting particles this is the ground state wavefunction of the

[1]Compare with the Fermi energy in a three-dimensional harmonic oscillator $(6N)^{1/3}\hbar\bar{\omega}$ as given in chapter 2. $T_c \approx 0.52 T_F$. This is worthwhile to mention as our experiments start with an ensemble of fermions which are combined to bosonic molecules employing the Feshbach resonance.

harmonic oscillator. How this wave function has to be modified in the presence of interaction will be described in the next section.

The phenomenon of Bose-Einstein condensation was already predicted in 1925 by A. Einstein [Ein] based on the work of S.N. Bose [Bos]. It took 70 years until techniques were developed that enabled to observe Bose-Einstein in a dilute sample of laser cooled alkaline atoms in the groups of E. Cornell, R. Hulet and W. Ketterle [And95, Bra95, Dav95].

5.2 The condensed state in the presence of interactions

In a realistic treatment of a Bose-Einstein condensate the interaction between the particles has to be taken into account. Gross [Gro61, Gro63] and Pitaevskii [Pit61] found an equation for the macroscopic wavefunction of the BEC which takes the interaction into account by employing a mean-field approach. The Gross-Pitaevskii equation (GPE) reads

$$i\hbar\frac{\partial}{\partial t}\psi(\mathbf{r},t) = \left(-\frac{\hbar^2}{2m}\nabla^2 + V_{ext}(\mathbf{r},t) + g|\psi(\mathbf{r},t)|^2\right)\psi(\mathbf{r},t) \tag{5.7}$$

where $g = 4\pi a\hbar^2/m$ is the coupling constant determined by the s-wave scattering length defined in chapter 2. This is the Schrödinger equation of a particle confined in an effective potential given by the sum of the external potential V_{ext} and an additional contribution due to interactions which is proportional to the particle density $n(\mathbf{r},t) = |\psi(\mathbf{r},t)|^2$. In the stationary case, the temporal evolution can be separated using the following ansatz for the macroscopic wavefunction

$$\psi(\mathbf{r},t) = \psi(\mathbf{r})e^{\frac{i}{\hbar}\mu t}. \tag{5.8}$$

Inserting this ansatz into 5.7 yields the time independent GPE

$$\mu\psi(\mathbf{r},t) = \left(-\frac{\hbar^2}{2m}\nabla^2 + V_{ext}(\mathbf{r},t) + g|\psi(\mathbf{r},t)|^2\right)\psi(\mathbf{r},t). \tag{5.9}$$

It is important to note that the time evolution of the macroscopic wavefunction is determined by the chemical potential and not by the energy as it is the case for a single particle state.

The Thomas-Fermi approximation

In general, solutions to the Gross-Pitaevskii equation are hard to find and in most cases it can be solved only numerically. An exception are system consisting of

a large number of particles in which the kinetic energy is negligible compared to the interaction energy. The GPE then reads

$$\left(V_{ext}(\mathbf{r} + g|\psi(\mathbf{r}))|^2\right)\psi(\mathbf{r}) = \mu\psi(\mathbf{r}) \tag{5.10}$$

which has the solution

$$n(\mathbf{r}) = |\psi(\mathbf{r}))|^2 = \frac{\mu - V_e xt(\mathbf{r})}{g}. \tag{5.11}$$

In the case of a harmonic oscillator potential the density distribution of the BEC thus has the shape of an inverted parabola.

To zeroth order the ratio of kinetic to interaction energy is given by [Dal99]

$$\frac{E_{int}}{E_{kin}} \sim \frac{Na}{a_{ho}}. \tag{5.12}$$

where N is the number of particles, a the s-wave scattering length and $a_{ho} = \sqrt{\hbar/m\omega}$ is the harmonic oscillator length. For a typical BEC of $^6Li_2$ molecules consisting of 100.000 molecules E_{int}/E_{kin} has a value of about 2000. Thus, experiments with a BEC of $^6Li_2$ molecules are done in the Thomas-Fermi regime.

For more information about the theory of Bose-Einstein condensates please refer to [Pit03, Pet02, Dal99].

5.3 Evaporative cooling

As discussed in section 4.2.3 the phase space density of ^{6}Li atoms achievable in the MOT by Doppler cooling is on the order of 10^{-6}. In order to reach condensation the phase space density of molecules must be larger than one. Thus another cooling technique must be applied to further decrease the temperature and increase the density in phase space. This is done by so-called evaporative cooling. The principle of evaporative cooling is easy to understand. After transfer of the atoms from the MOT into the dipole trap, the depth of the dipole trap is slowly reduced by lowering the laser power in the trapping beams. This allows hot particles to escape from the trap. More precisely, the tail of the Boltzmann-distribution is cut continuously while collisions between the particles restore the Boltzmann distribution, but with a lower temperature. It is useful to introduce the so called η-parameter defined by $\eta = U/k_BT$, which gives the ratio between the trap depth and the temperature of the sample in the trap. A fraction of $\exp(-\eta)$ atoms can leave the trap and take away energy. Under typical experimental conditions, values of $\eta = 10$ are achievable in optical dipole traps. Larger values are not desirable as the evaporation process will be slowed down significantly, while lower values

lead to inefficient cooling as too many atoms are lost. Thus a value of $\eta = 10$ is a good compromise for fast and efficient cooling. An ideal trap depth reduction scheme leaves η unchanged during the evaporation process. Scaling laws for such schemes are given in [O'H01, Luo06].

After the transfer of atoms from the MOT into the optical dipole trap, η is usually quite small which is not a good starting condition for forced evaporation. Thus, in most experiments a plain evaporation period is applied after transferring the atoms into the optical dipole trap during which the trap depth is kept constant. In this period the hottest atoms leave the trap and the lowest achievable temperature is determined by heating processes, for example due to instabilities of the trapping potential. Unfortunately, this is not possible in our setup as thermal lensing effects will reduce the quality of the profile of the trapping beam when the laser is running at full power for more than 100 ms. To avoid this, the power of the laser is ramped down from 200 to 42 W in 750 ms, 40 ms after the transfer. Right after the transfer from the MOT into the dipole trap the current in the Feshbach coils is ramped up to 210 A, generating a magnetic field of 750 G. At this field the scattering lengths between the two lowest hyperfine states has a large positive value of about 3500 a_0 allowing for fast thermalization and thus fast evaporation. As shown in chapter 2 a large positive scattering length is related to a weakly bound dimer state. After reduction of the laser power the trap depth is further decreased by a closed loop intensity reduction using an AOM and a digital PID loop implemented in our experimental control (see chapter 4). As soon as the temperature drops below the binding energy of the dimers which is about 2.6 μK at this field value, molecules of atoms in the two lowest hyperfine states are formed by three-body recombination (see section 5.4). These molecules are stable and the scattering length between the molecules is still large, being 0.6 times the value for free atoms. The polarizability of the molecules is twice as big as compared to free atoms, resulting in twice the trap depth for the molecules while the trapping frequencies are the same for molecules and atoms. In a temperature regime where both atoms and molecules are present, mostly atoms are evaporated whereas the molecules stay in the trap. Further reduction of the trap depth leads to evaporation of molecules and further increase of the phase space density. The molecules are bosonic particles and as soon as the phase space density exceeds one, a Bose-Einstein Condensate of these molecules is formed. The nice scattering properties of ^{6}Li allow for fast evaporation and the preparation of a BEC within 3 s in our setup. Typical particle numbers are about 150.000 molecules at a temperature of about 100 nK (see section 5.5).

5.4 Molecule formation

It was mentioned before that when the temperature of the sample becomes comparable to the binding energy of the Feshbach molecules, the molecular state becomes occupied via three-body recombination. Although three-body recombination should be suppressed in a two-component Fermi gas at first glance, D. Petrov [Pet03] showed that the three-body recombination rate close to a Feshbach resonance where a weakly bound dimer state exists is proportional to the sixth power of the scattering length. This means that for large positive scattering length where the dimer is weakly bound, molecular production rates can be high. Furthermore, it was shown that these dimers are amazingly stable, as the rates for inelastic atom-dimer or dimer-dimer collisions scale with $a^{-2.55}$ and $a^{-3.33}$ respectively [Pet05]. Thus, there is a large range of positive scattering lengths where molecular production rates are high and the molecules are stable which allows the preparation of an ultracold sample of Feshbach molecules [Joc03a, Str03, Cub03, Reg04a]. As soon as molecules are formed a chemical equilibrium between molecules and free atoms establishes. The ratio of the number of molecules to the number of free atoms is given by [Chi04b]

$$\frac{N_{mol}}{N_{at}} = \rho_{at} \times \exp(E_b/k_B T) \tag{5.13}$$

where ρ_{at} is the phase space density of the atoms and E_b the binding energy of the dimers. Thus, the lower the temperature the more molecules are present in the sample.

Detection of the molecules can be done in several ways. One possibility is the Stern-Gerlach separation of molecules and atoms using a magnetic field gradient. After dissolving the molecules by sweeping the magnetic field over the resonance to negative scattering length values two clouds can be imaged spatially separated. This is possible as the magnetic moment of the molecules is twice the magnetic moment of the atoms. The sweep over the resonance is necessary as the molecules can not easily be imaged by absorption imaging. The optical transition in the molecule is shifted with respect to the free atoms. Even if the laser would be tuned to the resonance of the molecules, one scattered photon would destroy the binding and the laser would be off-resonant again.

The formation of molecules can also be observed using radio-frequency spectroscopy. Let us imagine that a mixture of atoms in the two lowest hyperfine state of ^{6}Li is prepared in an optical dipole trap. By application of a RF-field with certain frequency atoms can be transferred from state $|2\rangle$ to state $|3\rangle$. If two atoms in each state are bound to a dimer, this frequency is not resonant any more, as an additional amount of energy equal to the binding energy is needed to break the molecule. Using this tool, the binding energy of the molecules can be measured

precisely. Fig. 5.1 shows the result of such a spectroscopic measurement. For

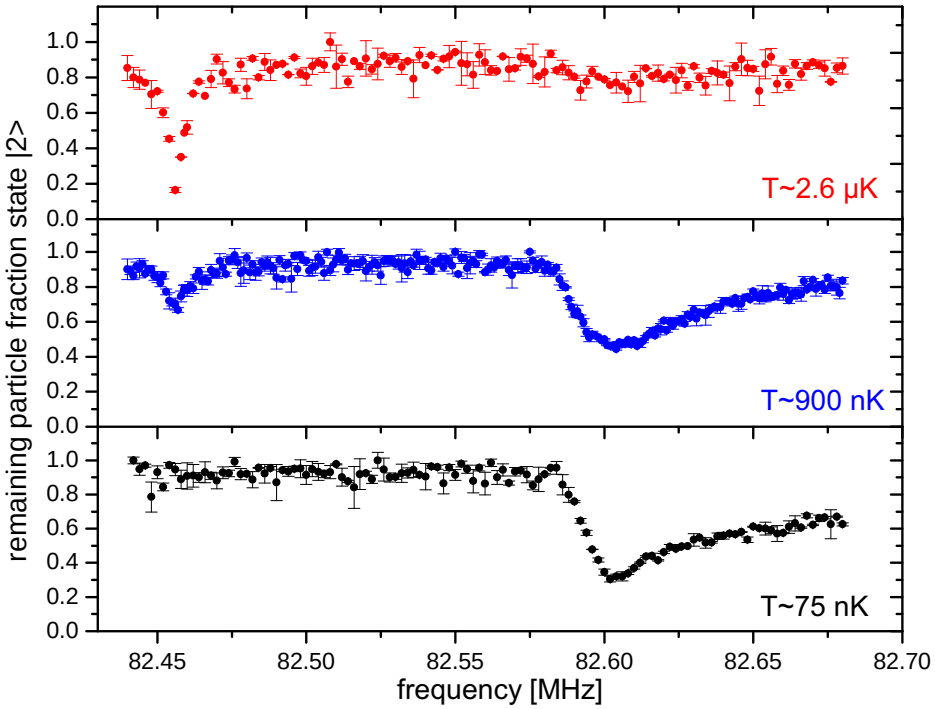

Figure 5.1: Radio frequency spectroscopy of atoms and dimers for different temperatures at 720 G. The plot shows the remaining fraction of atoms in state $|2\rangle$ as a function of the applied radio-frequency. At 2.6 μK only one distinct dip is visible indicating that most atoms are free and not yet bound into molecules. While the temperature is decreased further to 900 nK a second loss dip arises at higher frequencies, corresponding to molecules that were broken by the radio-frequency field. At about 75 nK the free-atom dip vanishes indicating that all atoms are bound into molecules.

this experiment the magnetic field was tuned to 720 G where the scattering length is 2170 a_0. Evaporation was stopped at different temperatures and the number of remaining atoms in state $|2\rangle$ was recorded by absorption imaging in dependence of the frequency of the applied RF-field. At 2.6 μK only one distinct loss dip occurs at 82.454 MHz, corresponding to free atoms that were transferred to state $|3\rangle$. Decreasing the temperature to about 900 nK, leads to the emergence of a second broad loss dip at higher frequencies. This loss corresponds to atoms that were bound into dimers which were broken by the RF-field. The particular shape of this dissociation dip arises due to the momentum distribution of the atoms in the molecule. If the atoms have a finite momentum in the molecule, additional energy has to be transferred by the RF photon in order to fulfill the dispersion relation

for the free atoms after dissociation. The shape of such a dissociation spectrum was used to determine the pair size in a strongly interacting superfluid Fermi gas [Sch08]. From the low energy onset of the loss the binding energy of the dimer can be determined to be 140 kHz at this magnetic field value. At a temperature of about 75 nK the free atom loss vanishes, indicating that all atoms are bound in dimers. More experiments concerning the formation of weakly bound dimers during the evaporation process are discussed in the diploma thesis of Matthias Kohnen [Koh08].

5.5 Observation of Bose-Einstein condensation

For Bose-Einstein condensation to occur, the thermal de-Broglie wavelength must be on the order of the interparticle spacing. This is equivalent to the requirement that the phase space density defined by $\rho = n\lambda_{th}$ must be larger than one[2]. Here n is the particle density and $\lambda_{th} = h/\sqrt{2\pi m k_B T}$ is the thermal de Broglie wavelength. In an optical trap which in most cases can be approximated by a harmonic potential the phase space density can be calculated to be

$$\rho = N \left(\frac{\hbar \bar{\omega}}{k_B T} \right)^3 \tag{5.14}$$

where N is the number of particles, $\bar{\omega}$ the mean trapping frequency and T the temperature of the sample. As all these parameters can be determined independently in the experiment, the calculated phase space density can be a first benchmark for the onset of Bose-Einstein condensation.

A standard method to observe the onset of Bose-Einstein condensation in trapped gases is the emergence of a bimodal distribution in time of flight images (see for example [Ket99]). The BEC reveals itself as a sharp peak surrounded by a thermal cloud with Gaussian envelope. As the molecules in our BEC interact strongly repulsive, the expansion of the BEC is comparable to the expansion of the thermal cloud which makes it very hard to distinguish between both phases. Nevertheless, it is possible to apply a little trick to observe the bimodal structure. Directly after the trap has been switched off to release the cloud for time of flight, the magnetic field is ramped to 500 G to decrease the mean field energy and thus the expansion of the condensed fraction. The reduced density after switching off the trap allows this magnetic ramp without loosing too many molecules via collisional relaxation. The field is then tuned to 785 G where the binding energy of the molecules is small, such that absorption imaging is possible. The resulting

[2]Strictly speaking the phase space density for a homogeneous gas must be larger than $\zeta(3/2) = 2.612$ or larger than $\zeta(3) = 1.202$ in case of a harmonically trapped system.

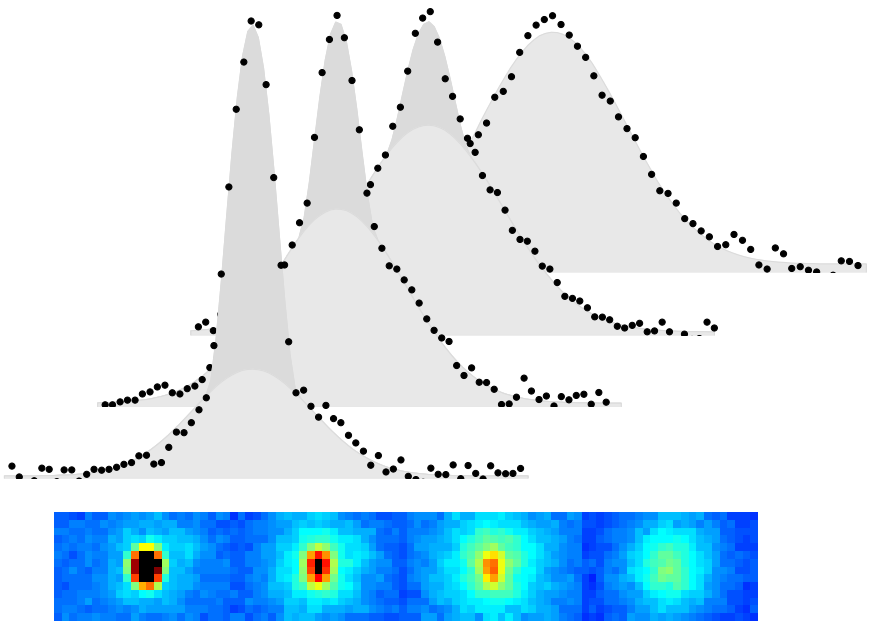

Figure 5.2: The lower panel shows false color absorption images of the molecular cloud after time of flight. The temperature of the sample increases from left to right. The upper panel shows the one dimensional density distribution which is acquired by summing the absorption signal shown below in the vertical direction. With decreasing temperature a clear bimodal distribution is visible. The colors indicate the thermal and the condensed part. The thermal part, shown in light gray, is fitted using a simple Gaussian distribution. For the condensed part, shown in dark gray, a Thomas-Fermi distribution was used.

density distributions for different stages during evaporation are shown in Fig. 5.2. In the lower panel, the false color absorption images of the density distribution after time of flight is shown. The density in the center of the cloud increases strongly with decreasing temperature, indicating the formation of a Bose-Einstein condensate. The temperature increases from left to right. The upper panel shows the one dimensional density distribution acquired by summing the absorption signal in the vertical direction. A bimodal structure clearly appears with decreasing temperature. The thermal fraction was fitted by a Gaussian function and is shown in light gray. The dark gray part shows the condensed fraction fitted with an inverted parabola corresponding to a Thomas Fermi distribution. From this fit the condensate fraction was determined. The experimental conditions under which the images were taken are presented in Table 5.1.

Beam power [mW]	35(2)	61(2)	99(3)	189(6)
Radial trapping frequency [Hz]	194(10)	277(14)	367(19)	519(26)
Axial trapping frequency [Hz]	19(1)	26(2)	34(2)	48(3)
Number of particles [$\times 10^3$]	55(1)	76(2)	99(2)	75(3)
Temperature [nK]	28(2)	115(1)	189(2)	309(3)
calculated phase density	≈ 200	11	7	3
fitted condensate fraction	0.68	0.24	0.10	0.002
calculated condensate fraction	0.81	0.52	0.45	0.3

Table 5.1: Experimental parameters for the molecular clouds shown in Fig. 5.2 from left to right. The fitted condensate fraction is always lower than the one expected due to the calculated phase space density. This is most probably due to the special field ramp technique described in the text which was used to make the bimodal structure visible. The calculated condensate fraction does also not take into account the interaction between the molecules which might lead to a depletion of the condensate. The condensate fraction was calculated by combining equations 5.14 and 5.6.

The first BEC of molecules was prepared in our setup exactly after one year of building and demonstrates that the apparatus is ready for experiments exploring new physics. The experiments that were done in the following year on three-component Fermi gases and their interpretation is presented in the following chapter.

Chapter 6

From two to three: Experiments with three-component Fermi gases

In this chapter our experiments on three-component Fermi mixtures consisting of atoms in the three lowest hyperfine states of ^{6}Li are described. As a short motivation an overview of the phenomena expected in such systems is given. Then the experimental procedure for the preparation of the sample is described and the results on our study of the collisional stability in dependence of the interparticle interaction are presented. In the last section, the experimental data is interpreted in terms of an Efimov-like universal trimer state.

6.1 Motivation

In the last decade tremendous progress has been made in the field of cold atoms, starting with the first experimental realization of Bose-Einstein Condensation in dilute gases in 1995 [Dav95, And95, Bra95]. Using similar techniques as for bosonic samples, it was possible to observe the onset of Fermi degeneracy in an ensemble of fermionic atoms in two different spin states [DeM99b] in 1999. The stability of two-component Fermi mixtures, together with the possibility to tune the interparticle interactions by means of Feshbach resonances allowed for the study of fermionic superfluidity and the so-called BEC-BCS crossover [Zwi05, Bar04, Reg04b, Bou04]. So far, a third state was only considered as a probe for the two-component sample. It was used as a final state in radio frequency spectroscopy [Gup03, Chi04a, Bar05] or as a tool for thermometry of degenerate Fermi gases [Reg05], but a sample of three distinguishable fermions in thermal equilibrium has not yet been prepared. A number of questions arise when a third distinguishable fermion is added:

a) In a three-component fermionic mixture the Fermi pressure is reduced com-

pared to a binary mixture [Blu08, Hei01]. Is there a critical interaction strength for which the system collapses?

b) How does pairing occur in a three-component Fermi gas? Will two species pair, forming a superfluid under appropriate circumstances, while the third one remains a spectator and how do these configurations depend on parameters like chemical potential, mass ratios and temperature? First order quantum phase transitions and second order phase transitions at finite temperature between different paired states as well as the normal unpaired state have been predicted [Paa06, Hon04, Sil09, Err09, Che07, Zha07, Bed09].

c) Does phase separation occur between different paired superfluid states in trapped three-component gases? [Paa07]

d) Are there three-body bound states comparable to Efimov states in a three-component Fermi mixture? Is a gas of such trimers the ground state of the system? [Rap07, Bra06, Flö09a, Nis09] This question will be throughly discussed in this thesis.

e) Which phenomena arise when a three-component Fermi gas is loaded into an optical lattice? Quantum phase transitions between superfluid phases and a phase of trions are predicted [Rap08, Rap07, Mol09, Aza08]. Additionally, it seems that strong three-body loss can be utilized for the stabilization of paired superfluid phases in optical lattices [Kan09].

f) If the three components interact with the same scattering length, the system has a SU(3) symmetry which reminds of the symmetry of colour and flavour in QCD. Thus, such an ultracold three-component Fermi gas may establish a model system for aspects of high energy physics as for example colour superfluidity [Wil07, Rap07].

The experiments reported in this thesis make the first steps towards the study of these phenomena, by preparing a three-component ultracold Fermi gas consisting of atoms in the three lowest hyperfine states of ^{6}Li in thermal equilibrium. These states are denoted by $|1\rangle$, $|2\rangle$ and $|3\rangle$ in figure B.2 in the appendix. Due to overlapping Feshbach resonances between each pair of these states, ^{6}Li offers unique possibilities to access different parameter regimes for the interparticle interaction, making it a promising candidate for the observation of effects like pairing competition between different superfluid phases. Prerequisite for such an experiment is a sufficient lifetime of the sample. Thus, after successful preparation of the gas, our first experiments studied its collisional stability.

6.2 Preparation of a three-component mixture

So far there has been only little experimental work on three-component Fermi gases: A third non-degenerate sample was used as a probe for thermometry in samples of ^{40}K atoms [Reg05]. In experiments studying pairing in two-component gases of ^{6}Li, the third state (labeled as $|3\rangle$ in figure B.2) was used as a final state for radio-frequency spectroscopy [Chi04a, Sch08]. The lifetime of atoms in this third state was limited to milliseconds. Thus, it seemed that strong loss processes would make the preparation of a three-component sample with ^{6}Li atoms difficult.

The dominant loss process in ultracold gases is three-body recombination as discussed in section 3.3. Two-component Fermi gases exhibit a remarkable stability against three-body decay over a wide range of interparticle interactions [Pet04, Pet05]. In a simple picture this is due to the fact that in a three-body event at least two identical fermions have to come close together which is suppressed by the Pauli principle. When a third component is present, this does not hold anymore and the probability for three-body recombination increases, limiting the lifetime of the sample (see figure 6.1 a) and c)). Thus, a parameter regime where the interaction between the particles is weak enough to suppress three-body recombination has to be found in order to prepare a three-component sample. In other words, the scattering lengths between the particles must be sufficiently small. Luckily, the zero crossings of the Feshbach resonances between the three lowest states occur at similar magnetic field values around 560 G. This field region is most promising for the preparation of the three-component mixture. Before the third state is being populated, an ultracold two-component mixture of states $|1\rangle$ and $|2\rangle$ has to be prepared at this magnetic field value, which turns out not to be straightforward. As soon as this is accomplished the third state can be populated by applying radio-frequency fields.

The first steps of the production scheme involve the preparation of a binary mixture of states $|1\rangle$ and $|2\rangle$ at 563 G. This is done in the following way: After transferring the atoms from the MOT into the optical dipole trap, evaporation of the $|1\rangle$-$|2\rangle$ mixture is performed at 751 G where the scattering length is large and positive ($a_{12} = 3560a_0$) leading to high thermalization rates which enable fast and efficient evaporative cooling. When the temperature of the sample is about 10 μK the magnetic field is tuned to 300 G, where the scattering length a_{12} is about $-290\,a_0$ [1]. As the absolute of the scattering length is smaller at this magnetic field, collision

[1] Continuing the evaporation at 751 G would result in the formation of dimers as discussed in section 5.4. If molecules are present in the sample when the magnetic field is reduced to 563 G, strong losses occur due to collisional relaxation of the molecules. This is due to the fact that with decreasing scattering length the dimers become more bosonic in character and the argument given in the text does not hold anymore (see figure 6.1 b). As shown in [Pet04, Pet05] dimer relaxation rates scale as $a^{-3.33}$ for atom-dimer collisions and as $a^{-2.55}$ for dimer-dimer collisions.

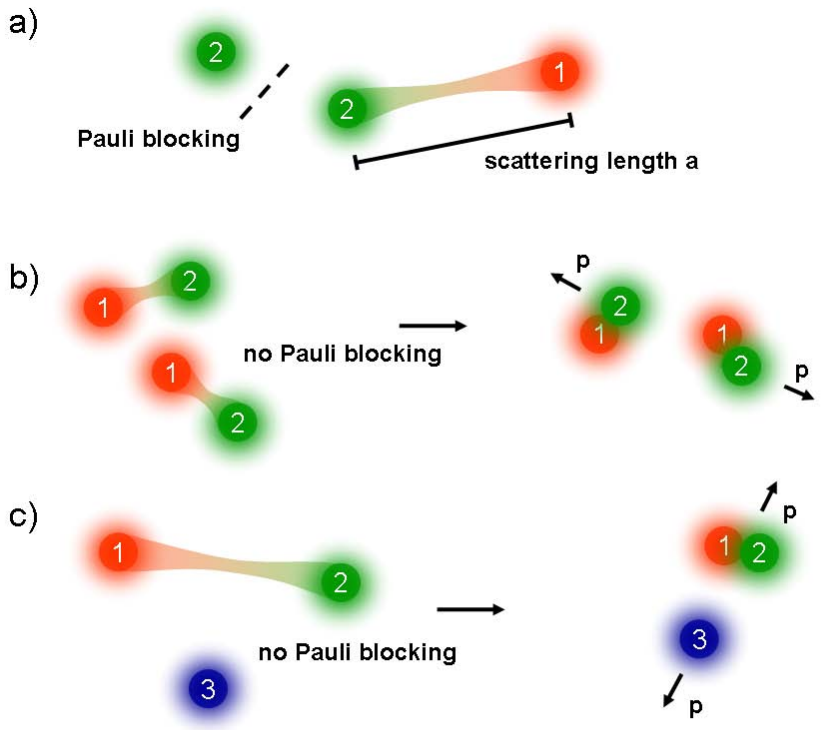

Figure 6.1: a) Due to Pauli blocking Feshbach molecules in a two-component mixture are remarkably stable for large scattering lengths. b) When the scattering length is decreased the molecules get more tightly bound and more bosonic in character. This weakens the Pauli blocking effect, and collisional relaxation becomes a serious problem for the stability of the sample. c) When a third distinguishable Fermion is present, no Pauli blocking occurs and strong losses are possible.

rates are reduced compared to 751 G. Thus, thermalization is slower and evaporation needs more time. With this evaporation scheme we are able to produce two-component samples with about 7.5×10^4 atoms per spin states at temperatures as low as 130 nK. After evaporation is finished the power in the dipole trap beams is adiabatically increased by a factor of two to avoid further evaporation. This increase in trap depth leads to adiabatic heating of the sample, but leaves T/T_F unchanged, as the temperature and the trapping frequencies scale in the same way with the laser power. After increasing the laser power, the trapping frequencies are $\omega_x = \omega_y = 2\pi \times 386(15)Hz$ and $\omega_z = 2\pi \times 38(2)Hz$, determined with the procedures described in 4.3. From this we calculate $T/T_F \approx 0.28$ which is in the quantum degenerate regime. To create the three-component mixture the magnetic field is tuned to 563 G. Here, the scattering lengths are $a_{12} \approx +135a_0$,$a_{23} \approx -140a_0$

and $a_{13} \approx -95a_0$. These are small enough to minimize three-body recombination, but still large enough to allow for thermalization.

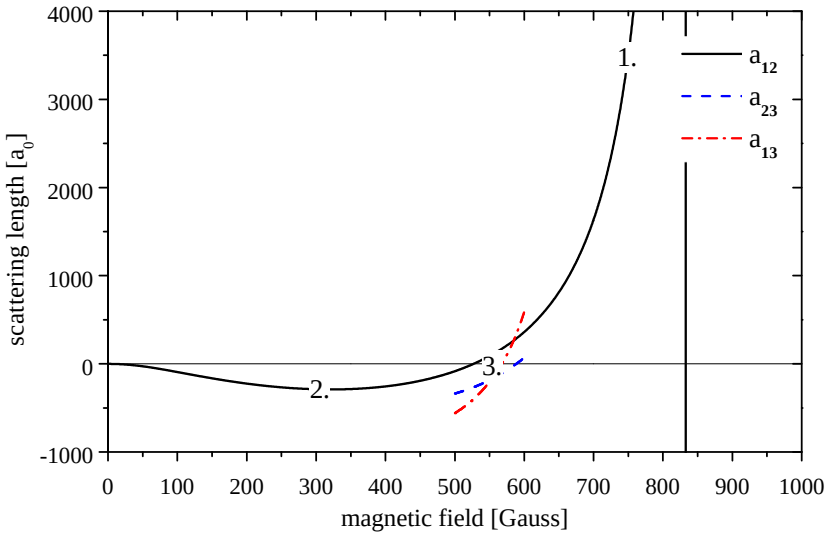

Figure 6.2: Main steps during preparation of the three-component Fermi mixture. 1.) Evaporation at 751 G 2.) Before molecule formation sets in, the field is tuned to 300 G to avoid losses via collisional relaxation during the field ramp. Evaporation is finished at this magnetic field value. 3.) The field is tuned to 563 G where the three-component mixture is prepared by applying radio frequency fields.

In the next step the three-component mixture is prepared by applying simultaneously two radio-frequency fields for 850 ms, whose frequencies are matched to the $|1\rangle - |2\rangle$ and the $|2\rangle - |3\rangle$ transition. A residual magnetic field gradient and collisions between the atoms lead to an incoherent mixture of atoms in the three lowest spin states with 5×10^4 atoms per state. As atoms have been distributed over all three states the degeneracy decreases, resulting in $T/T_F \approx 0.37$. The density of the sample is about 6×10^{11} atoms/cm^3 per state.

We observe a $1/e$ lifetime of 30 s demonstrating that we are able to prepare a degenerate and stable three-component Fermi mixture consisting of atoms in the three lowest hyperfine states of ^{6}Li in thermal equilibrium, which is the starting point for our experiments.

6.3 Collisional stability

In the following, measurements concerning the collisional stability of the sample are described. In a first experiment the three-component mixture was prepared

as described above, then the field was tuned to various magnetic field values between 0 and 750 G. After a holding time of 250 ms the field was tuned to 526 G and the number of remaining atoms was recorded by absorption imaging. Due to a Zeeman splitting of about 80 Mhz between the states, each state can be imaged separately in different experimental cycles. Imaging at a fixed field value brings the advantage that the laser frequencies for imaging must be calibrated only once. As the timescale for the magnetic field ramps is on the order of a few milliseconds, and thus significantly smaller than the holding time, their influence can be neglected. To confirm this, cross checks with zero holding time were also performed to rule out any corrections due to the finite ramp time. The outcome of this measurement is shown in figure 6.3. In the region of the zero crossings of the

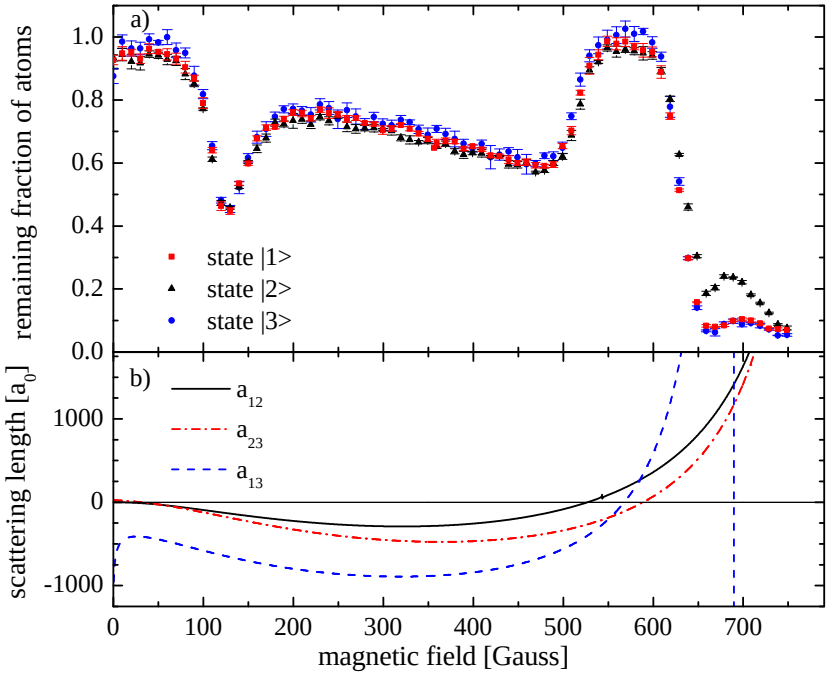

Figure 6.3: a) Remaining fraction of atoms in each spin state after holding the sample 250 ms at various magnetic field values between 0 and 750 G. b) Two body-scattering length for each binary mixture in the magnetic field region of interest.

scattering lengths between 540 and 590 G the remaining fraction of atoms is close to one. For fields larger than 600 G strong inelastic decay can occur already in a binary mixture due to the two-body Feshbach resonances (see figure 6.4). Here the influence of the third distinguishable Fermion is extremely hard to quantify. Thus, this region will not be considered in the following. Below 540 G the fraction of remaining atoms rapidly drops to a minimum of 0.6 at 470 G and then

increases linearly to 0.75 at 200 G. Between 80 and 190 G a strong loss feature occurs, where the fraction of remaining atoms drops to 0.5 at 130 G. For magnetic fields below 70 G the three-component mixture is once again stable. Considering the smooth behaviour of the scattering length in that magnetic field region such a strong variation of the stability is not expected, particularly the strong loss at 130 G is not understandable on basis of the scattering length. To verify that this effect indeed arises due to the presence of a third distinguishable fermion in the trap, we repeated the same experiment with all three possible binary mixtures. To keep this cross check as reliable as possible first the three-component mixture was prepared, then one of the components was removed with a resonant light pulse and the remaining atom number was again recorded as a function of the magnetic field. The results for each binary mixture is shown in figure 6.4. All binary mixtures are

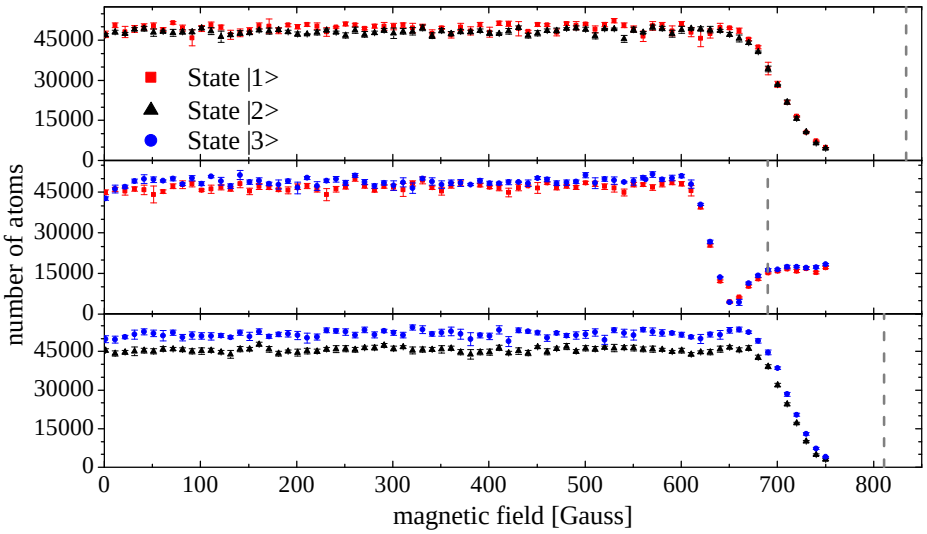

Figure 6.4: Remaining fraction of atoms after 250 ms for a binary mixture. The third component was removed by a resonant light pulse at 563 G.

stable stable between 0 and 600 G. In the region below the Feshbach resonances in the respective channels losses occur which are expected due to inelastic collisional relaxation of dimers. The lifetime of all binary mixtures in the low-field region is limited by heating due to photon scattering from the trapping light and background collisions. Thus, the magnetic field dependence of the losses in figure 6.3 can be attributed to the processes involving particles in the lowest three Zeeman substates of ^{6}Li

6.4 Measurement of three-body loss coefficients

The loss measurement described in the last section shows that so far unidentified three-body processes including particles in all three spin states alter significantly the stability of the sample in dependence of the magnetic field. As the loss for a fixed holding time in figure 6.3 depends strongly on the atomic density in the dipole trap a more quantitative analysis has to be done. In our three-component mixture the loss of atoms can be described with the following differential equation

$$\frac{dn_i(\mathbf{r})}{dt} = -K_3\, n_1(\mathbf{r})\, n_2(\mathbf{r})\, n_3(\mathbf{r}) - K_{1,i}\, n_i(\mathbf{r}) \tag{6.1}$$

where $n_i(\mathbf{r}), i = 1, 2, 3$ denotes the density of atoms in state $|1\rangle$, $|2\rangle$ or $|3\rangle$. The first term on the right hand side describes losses in which atoms in all three states are involved. This ansatz is possible as atoms in all three states get lost in equal measure. The last term attributes to one-body losses due to the scattering of photons from the trapping light and collisions with the residual background gas. As shown in in the last section, two-body losses are weak in the magnetic field region of interest and can therefore be neglected. To obtain quantitative information on K_3,we prepared the three-component mixture as described above, tuned the magnetic field to to the value of interest and observed the subsequent evolution of atom number and temperature as a function of time. As an example figure 6.5 shows the evolution of atom number and temperature for state $|2\rangle$ over five seconds at a magnetic field of 300 G. To deduce K_3 from the lifetime measurements we follow a model originally developed in [Web03b]. This model is strictly speaking only applicable for a thermal gas, but at a degeneracy of $T/T_F \approx 0.37$ only minor changes occur which can be neglected. The local differential equation in 6.1 can be spatially integrated under the assumption of a thermal gas with Gaussian density distribution of the atoms, yielding

$$\frac{dN}{dt} = -\alpha N - \gamma \frac{N^3}{T^3}. \tag{6.2}$$

where α describes the one-body loss and γ is related to the three-body loss via

$$\gamma = K_3 \frac{1}{\sqrt{27}} \left(\frac{m\bar{\omega}^2}{2\pi k_B} \right)^3. \tag{6.3}$$

Three-body loss does not only lead to loss of atoms, but also to an increase in temperature caused by anti-evaporation. As three-body loss depends on the third power of the density, it predominantly happens in the center of the trap, where the mean temperature of the atoms is lower than in the outer regions. Thus, the coldest atoms are lost first, leading to an increase of the temperature. This increase

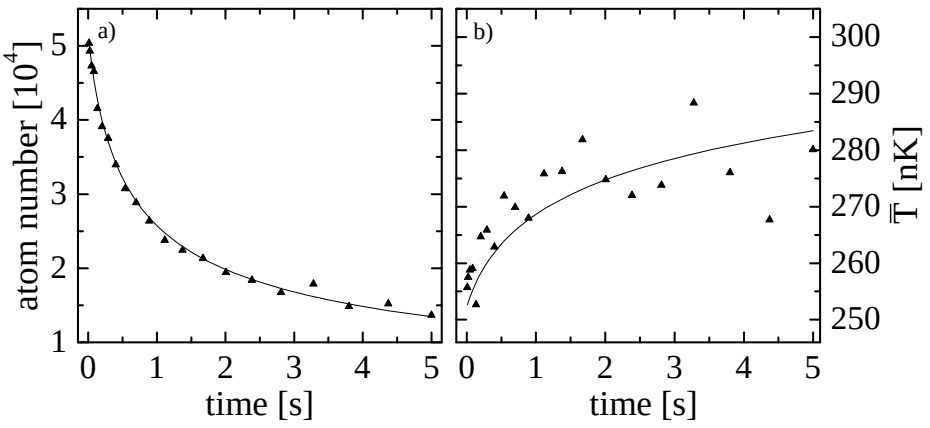

Figure 6.5: Evolution of atom number and temperature of the atoms in state $|2\rangle$ over five seconds at 300 G. $\bar{T}$ denotes an effective temperature temperature deduced from a Gaussian fit to the cloud after time of flight. Each data point is a mean value of three independent measurements taken in random order. The solid line is a fit to the data, applying the method described in the text. The resulting K_3 for the shown data is 1.93×10^{-23} cm^6/s.

in temperature can be modeled by comparing the heating energy per loss to the mean energy per particle

$$\frac{\dot{T}}{T} = \frac{\dot{N}}{N}\frac{k_B T_h}{3k_B T}. \tag{6.4}$$

Inserting equation 6.2 under the reasonable assumption that only three-body loss contributes to heating, yields

$$\frac{dT}{T} = \gamma\frac{N^2}{T^3}\frac{T_h}{3}. \tag{6.5}$$

Equations 6.2 and 6.2 form a set of two coupled differential equations describing the evolution of atom number and temperature in the trap as a function of time. The measured lifetime curves were analyzed using an optimization algorithm minimizing the least square error between the measured data and numerical solutions of these equations. This was done in the following steps.

1) Chose initial α and γ, by fitting equation 6.2 to the data, ignoring the temperature dependence.

2) Fit the measured temperature evolution, using α and γ determined in the last step, with T_h being the only free parameter

3) Calculate the error sum of squares between the measured values and the numerical solutions

4) Repeat steps 1)-3) while α and γ are varied to minimize the error sum of squares

For the analysis of the lifetime curves, we use an effective temperature ($\bar{T}$ in figure 6.5) deduced from a Gaussian fit to the density distribution after time of flight. If the gas is degenerate, the obtained value $\bar{T}$ is slightly higher than the real temperature. As the density in a degenerate Fermi gas is reduced with respect to a thermal gas of the same temperature, the higher effective temperature value compensates to some extent for the small effects of degeneracy. Hence, $T \approx \bar{T}$ is a good approximation. For most values of K_3, this approximation affects only the first data points, as the temperature exceeds the Fermi temperature after initial loss and heating.

The Matlab code for this analysis was developed by T. Weber and uses a nonlinear optimization algorithm [Web03a, Web03b]. In the original model the heating energy is defined as $k_B(T+T_{rec})$ where the first summand is due to anti-evaporation and the second due to recombination heating[2] . This leads to a more difficult differential equation and a less stable numerical convergence. Thus, we combined both contributions in the single parameter T_h. As the overall temperature increase is small compared to the absolute temperature of the sample, this does not change significantly the result. It turns out that the fitted T_h is comparable to the absolute temperature of the sample, showing that recombination heating and other heating processes are negligible As shown in figure 6.5 the agreement between the measured values and the fit according to our model is good. The result for the three-body coefficients in dependence of the magnetic field is shown in figure 6.6. The observed values of K_3 vary over three orders of magnitude between 10^{-25} and 10^{-22} cm^6/s and reflect the behaviour of the atom number in figure 6.4. The smallest observed value is still four orders of magnitude larger than the value for three-body recombination in a thermal cloud of ^{87}Rb [Bur97], but small enough to observe lifetimes of 30 s. The behaviour of K_3 shows two maxima, a pronounced one at around 130 G and a more broadened one at values of 500 G. At 200 nK unitarity limits the observable K_3 to values smaller than about 2×10^{-19}cm^6/s (from equation 3.33) which is three orders of magnitude larger than our largest observed value. Thus, thermal effects do not have an influence on this measurement.

The relative error on K_3 can be estimated from the scatter of fitted values for different spin states and is much smaller than the variation of K_3 with the magnetic field. These errors are mainly caused by uncertainties in spin imbalance, different detection efficiencies of the states and fitting uncertainties. The error on the absolute scale is subject to additional systematic errors in particle number and trap frequency. As $K_3 \propto N^2\bar{\omega}^6$ uncertainties of 40% in N and 7% in $\bar{\omega}$ lead to an uncertainty of about a factor of two in the absolute scale. The results of this and

[2] In [Web03a, Web03b] T_{rec} is called T_h. The notation was changed to avoid confusion.

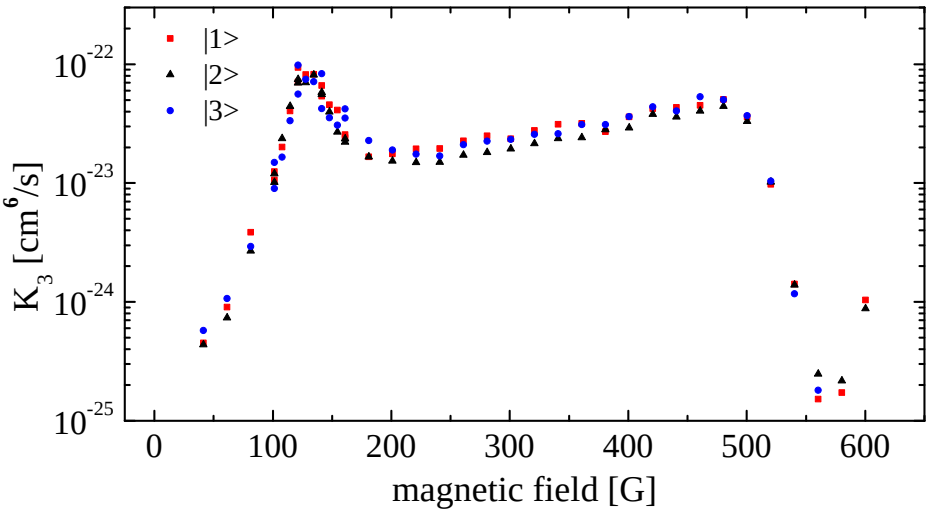

Figure 6.6: Measured three-body loss coefficients in dependence of the magnetic field between 50 and 600 G. The values are determined from lifetime measurements analyzed with the method described in the text. The loss coefficients reflect the qualitative behaviour of the atom number in figure 6.4, especially around 130 G the loss coefficients are strongly enhanced.

the previous chapter have been published in [Ott08]. Similar results have independently been obtained in the group of K. M. O'Hara [Huc09]. Their measurements also include data at higher magnetic field values up to 950 G, including the region of the Feshbach resonances.

6.5 Interpretation of the data

This section is devoted to the theoretical interpretation of our data on the three-body loss coefficients in the magnetic field region between 0 and 600 G. It will be shown that the magnetic field dependence in figure 6.6 can be fully explained by presence of a universal Efimov-like trimer consisting of atoms in all three Zeeman substates. This trimer crosses the scattering threshold for three free atoms twice and has a magnetic field dependent lifetime. For the interpretation of our data we adapt the theory of Braaten and Hammer [Bra06] by combining the three different two-body scattering lengths a_{12}, a_{23} and a_{13} to an effective interaction parameter a_m and including a magnetic field dependent lifetime of the trimer.

6.5.1 Scaling of three-body losses in a three-component Fermi gas

In section 3.3 it was shown that in general three-body loss coefficients scale with the fourth power of the scattering length. The theory for three-body physics and recombination presented in chapter 3 was originally developed for a sample of indistinguishable bosons, where interactions are described by a single scattering length. In contrast, our system consists of three distinguishable fermions whose pairwise interactions are described by three different scattering lengths denoted by a_{12}, a_{23} and a_{13} (see figure 6.7). Yet, it is possible to combine these scat-

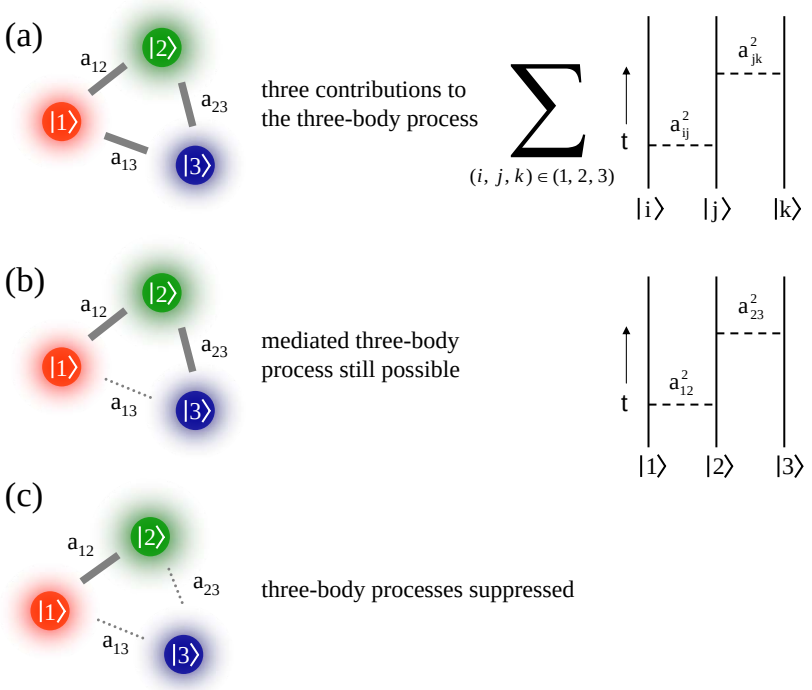

Figure 6.7: Possible three-body events in a sample of three-distinguishable fermions, under the assumption that collisions involving three different fermions can be described as two independent two-body collisions governed by the respective scattering lengths. a) When all three scattering lengths are larger than the effective range of the underlying van der Waals potential, the three-body collision can happen in three different configurations. b) If only two scattering lengths are large, only one mediated process has to be taken into account. c) In the case of two scattering lengths being small, no three-body processes are allowed, and the sample can effectively be described as a two-component system.

tering lengths to a single interaction parameter a_m. To do so, the assumption is

made that a three-body collision can be described by two independent two-body events which are described by the respective two-body scattering lengths. Thus, the probability for a three-body collisions can be expressed as the product of the cross-sections of the two-body collisions. These scale with a_{ij}^2, leading to an $a_{ij}^2 a_{jk}^2$ scaling for the rate of three-body collisions. In a sample of three distinguishable fermions this collision can happen in three different configurations. By summing over them, a scaling parameter for the total rate of three-body collisions can be defined

$$a_m^4 = \frac{1}{3}\left(a_{12}^2 a_{23}^2 + a_{13}^2 a_{23}^2 + a_{12}^2 a_{13}^2\right). \tag{6.6}$$

This ansatz is valid, except for those cases when one of the scattering lengths diverges. This would mean that the rate for three-body collisions also diverges which is not correct. Equation 6.6 correctly describes several important limiting cases. If all three scattering lengths are equal $a_{12} = a_{23} = a_{13} = a$ the simple a^4 scaling for three-body recombination is reproduced. It also describes correctly the fact that three-body processes are suppressed when two of the scattering lengths are small. This is confirmed by our measurements close to zero magnetic field. Here only a_{13} is large and the three-component mixture is stable. The scaling of three-body loss, taking all scattering lengths into account, has also been rigorously calculated by Braaten et al. [Bra09b] in the case of $a_{13} \gg a_{12}, a_{23}$. J. D'Incao and B. Esry [D'I09] considered a system with $a_{13} \gg a_{23} \gg a_{12} \gg r_0$ with r_0 being the effective range of the van der Waals potential. The ansatz in equation 6.6 agrees with the results of both rigorous calculations.

With this scaling at hand it is possible to predict the behaviour of three-body loss in the region between 65 G and 510 G where all scattering lengths are larger than the range of the van der Waals potential. Figure 6.8 shows a comparison of the measured K_3 and the expected behaviour according to equation 6.6. The prefactor of the a_m^4 scaling was adjusted to reproduce the measured K_3 at 300 G. The measured values for the different components were averaged to a single one. Obviously, there is strong disagreement between the experimental values and the behaviour expected due to the simple a_m^4 scaling. The loss is strongly enhanced at the loss feature at 130 G and around 500 G. As in these regions all scattering lengths are larger than the range of the van der Waals potential, observables are universal in the sense that they should depend only on the scattering length. Thus, additional physics, which is not captured by the two-body scattering lengths, lead to a resonant enhancement of the three-body recombination rate. As described in chapter 3, resonant enhancement of three-body loss coefficient with respect to the background behaviour is caused by the presence of universal trimer states crossing the free atom threshold. The application of this idea to our experimental results is discussed in the next section.

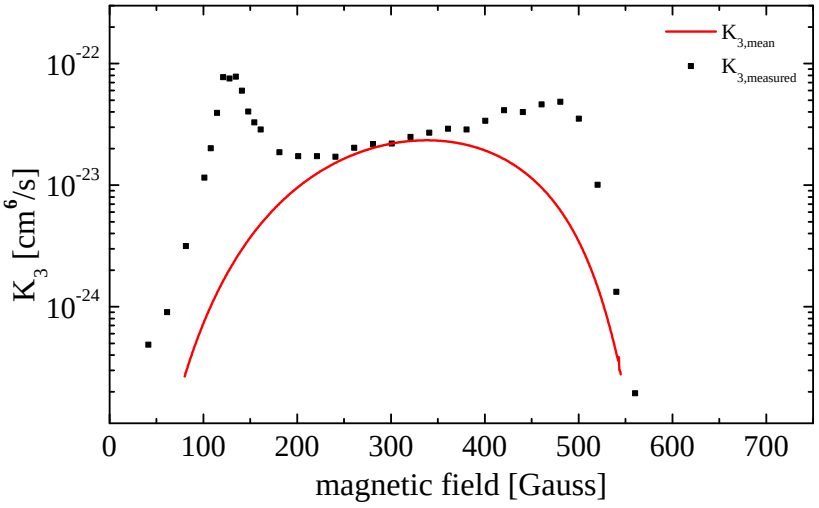

Figure 6.8: Comparison of the measured K_3 values and the expected behaviour due to a simple a_m^4 scaling. The experimentally determined loss coefficients for each component were averaged to a single one for this plot. The overall offset of the a_m^4 scaling was adjusted to reproduce the measured value at 300 G. Clearly, there is strong disagreement between the simple a_m^4 scaling and the measured data. The measured loss coefficients are obviously enhanced at the loss feature at 130 G and at values around 500 G.

6.5.2 A universal Efimov-like trimer

The theoretical description of Efimov trimers was originally developed for a sample of identical bosons where the two-body interactions are described by a single s-wave scattering length. Braaten and Hammer [Bra06] have derived an analytical expression for three-body recombination into a deeply bound (non-universal) dimer and a free atom in the zero range and the low-energy limit.

$$K_{3,deep}(a) = \frac{c \sinh(2\eta_*)}{\sin\left[s_0 \ln(a/a_*)\right] + \sinh^2 \eta_*} \tag{6.7}$$

where a is the two-body scattering length, c is a numerical constant and $s_0 = 1.00624$ is the scaling parameter derived by Efimov. The properties of the Efimov trimers are described by the parameters a_* and η_*. a_* is the scattering length where the Efimov state crosses the free-atom threshold and is one choice for the three-body parameter discussed in chapter 3. η_* describes the lifetime of the trimer and therefore influences the width of the loss resonances. Both parameters can be combined in a complex three-body parameter, describing all properties of the trimer. As already discussed, in our three-component Fermi gas not only one

scattering length but three different ones between each possible pair combination describe the underlying two-body interactions. In the last section it was shown, that these three different scattering lengths can be combined to a single interaction parameter describing the strength of three-body recombination. Based on that discussion an effective mean scattering length a_m can be defined. As all three-scattering length are negative in the region of interest, it is defined as the negative fourth root of equation 6.6

$$a_m = -\sqrt[4]{\frac{1}{3}\left(a_{12}^2 a_{23}^2 + a_{13}^2 a_{23}^2 + a_{12}^2 a_{13}^2\right)} \tag{6.8}$$

and takes the role of the scattering length a in equation 6.7.

Using this effective mean scattering length, it is possible to fit the measured values of K_3 with formula 6.7. a_*, η_* and the normalization constant c are the free fitting parameters and are adjusted to get best agreement with the measured data around the loss feature at 130 G. The result is shown in figure 6.9. The fit re-

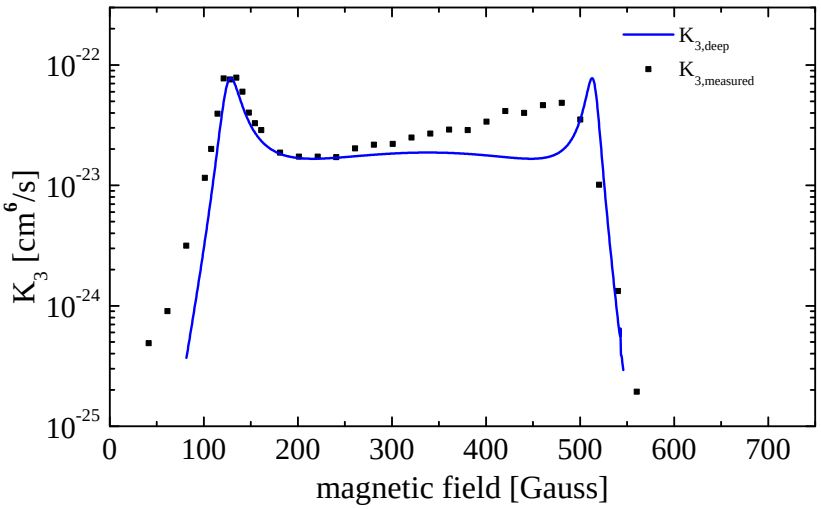

Figure 6.9: Fit of the measured K_3 values using the analytic formula 6.7 derived by Braaten and Hammer. The scattering length was substituted by the effective mean scattering scattering length defined in equation 6.8. The parameters a_* and η_* are adjusted for best agreement in the magnetic field region of the pronounced loss feature at 130 G. The resulting values are $a_* = -292a_0$, $\eta_* = 0.072$ and $c = 5612.88$. The fit reproduces remarkably well the behaviour around the narrow loss feature, but fails at higher field values. Especially the second sharp loss resonance at 500 G is not visible in the measured data.

produces remarkably well the behaviour of the loss coefficients around the loss

feature, indicating that this resonant enhancement of three-body loss is caused by a trimer state crossing the free atom threshold at this magnetic field. For higher magnetic field values, the fit completely fails and predicts a second sharp loss resonance at about 500 G which is not visible in the measured data. The fitted parameters are $a_* = -292a_0$, $\eta_* = 0.072$ and $c = 5612.88$. The shown results are very similar to the ones obtained by using the Skorniakov-Ter-Martirosian equations to directly calculate three-body loss rates [Bra09b], a hyperspherical treatment [Nai09] or functional renormalization group theory [Flö09b]. The model presented here did not include a rigorous treatment of all three different scattering lengths, but introduced an effective interaction parameter a_m allowing for the use of a semi-analytical model. This simplifies the analysis a lot and yields similar results as the thorough theoretical analysis.

The theoretical models predict a second sharp loss resonance at 500 G which is not visible in our data. This second enhancement of three-body loss is attributed to the Efimov trimer becoming unbound when a_m equals a_* again. Arguments based on universality suggest that beginning from low fields, at a certain interaction strength an Efimov trimer becomes bound whose binding energy increases with increasing scattering lengths. At about three-hundred Gauss where a_m has its maximum value, the binding energy is maximal and decreases again towards higher fields. When a_m equals a_* the second time, the trimer becomes unbound causing a second loss resonance. The disagreement of these models with the measurements raises some doubt about the validity of universality in the considered magnetic field range, as the scattering lengths become on the order of the effective range of the van der Waals potentials at about 500 G. But as shown in figure 6.8, three-body loss is enhanced over the expected background value over a wide range in this region. In the next section the reason for this behaviour is explained, taking into account the effects of the dimers below the scattering threshold.

6.5.3 Effects of dimers

The model discussed in the last section assumed that the parameters a_* and η_* do not depend on the magnetic field. In [Bra04, Bra01], E. Braaten and coworkers state that these parameters are in general smooth functions of the magnetic field, but can be approximated as constant values near narrow Feshbach resonances. This condition is clearly not fulfilled in the magnetic field region below 530 G, questioning whether the assumption made in the last section is justified. As the enhancement of three-body loss at 127 G and around 500 G appears for similar values of a_m, a variation of a_* is neglected. But what about η_*? How does the trimer decay and which parameters determine its lifetime? As discussed in chapter 3, the crossing of a trimer state with the free atom continuum leads to a resonant enhancement of three-body recombination into lower lying dimer states.

Thus, the trimer state is only virtually occupied and decays into a dimer and a free atom. In general, the properties of the lower lying dimer states are not known as they are deep in the non-universal regime and their binding energies greatly exceed $\hbar^2/2mr_0^2$. The situation is fundamentally different in our case. The highest dimer states below the scattering threshold are the ones associated with the four Feshbach resonances between 543 and 834 G. Their properties, as binding

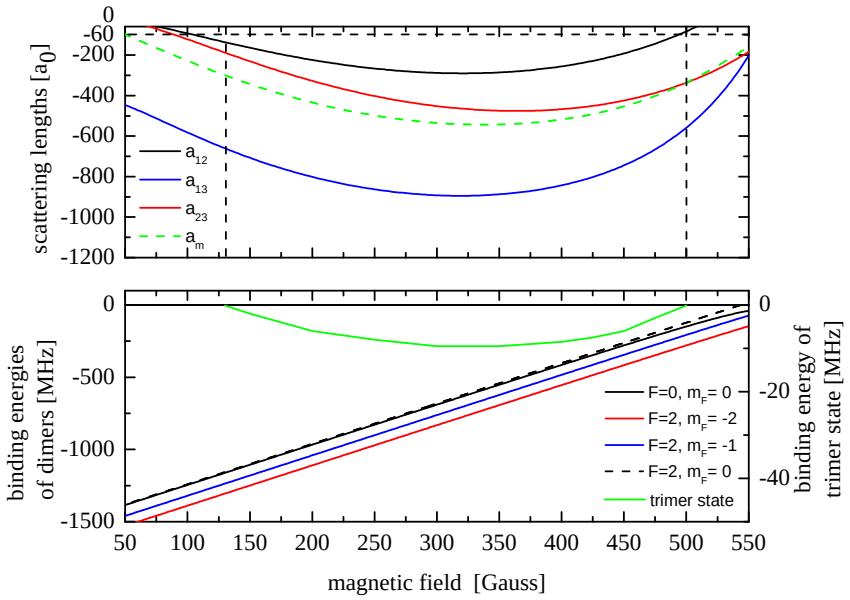

Figure 6.10: Upper Panel: Behaviour of the scattering lengths in the low-field region. The mean effective scattering length defined in 6.5.2 is plotted as a dashed line. The horizontal line in the upper panel indicates the van der Waals length of $60a_0$, while the vertical lines mark the positions where the trimer enters the free atom continuum ($a_m = a_*$). Lower panel: Binding energies of the dimer states and the Efimov-like trimer in the low-field region. The dimer states are associated with the Feshbach resonances with the four Feshbach resonances between 543 and 834 G. The binding energy varies more than a factor of five in the magnetic field region where the trimer exists. Considering the behaviour of the scattering lengths, the behaviour of the trimer is understandable on universal grounds. When the interaction strength, parametrized by a_m, overcomes a critical value, the trimer state becomes bound. With increasing $|a_m|$ the binding energy of the trimer increases, being maximal when $|a_m|$ is at its maximum value and then decreases. The trimer state becomes unbound when a_m equals the critical value again. The binding energy of the trimer state was taken from [Bra09a]

energies or open and closed channel fractions, can readily be calculated using a model described in [Chi09]. The results for the binding energies are shown in

the lower panel of figure 6.10. In the magnetic field region where the trimer state exists the binding energies of these dimer states vary by more than a factor of five. In the non-universal regime they tune as expected with two Bohr magnetons, corresponding to 2.8 Mhz/G, with respect to the free atom threshold. This strong variation in the binding energy of the dimer states has strong effects on the lifetime of the trimer as the wavefunction overlap is better the smaller the binding energy of the dimer. Better overlap makes the decay more probable and shortens the lifetime of the trimer. Thus, the value of η_* describing the width of the loss resonance should depend on the magnetic field. The experimental data suggest that the second loss resonance at around 500 G is broadened due to this effect. It turns out that already the simple ansatz $\eta_* \propto 1/E_B$ leads to good agreement with the experimental data. We assume that all four dimer states contribute in the same way, leading to

$$\eta_* = A \left(\frac{1}{E_{B,1}} + \frac{1}{E_{B,2}} + \frac{1}{E_{B,3}} + \frac{1}{E_{B,4}} \right) \tag{6.9}$$

where $E_{B,i}$ are the binding energies of the different dimer states shown in figure 6.10 and A is a numerical constant, which is adjusted in a way to reproduce the value of $\eta_* = 0.072$ acquired for the first loss resonance at 130 G within the constant lifetime model. Leaving a_* and the overall offset c in equation 6.7 unchanged while varying η_* according to 6.9 leads to the behaviour shown in figure 6.11. The result shows remarkable agreement with the measured three-body loss coefficient over the addressed magnetic field region. The fact that this agreement can be reached without considering a magnetic field dependence of a_* suggests that the short range physics determining the properties of the trimer do not change with the magnetic field. Thus, the disagreement of the measurements with the calculations in [Bra09b, Nai09, Flö09b] is not due to a breakdown of universality, but must be attributed to a variation of the dimer states the trimer decays into. While the trimer state itself can be completely described in a universal framework, its decay depends on non-universal dimer states, whose magnetic field dependence leads to a variation of the elasticity parameter η_* and thus to a broadening of the observed three-body loss resonance. The assumption of $\eta_* \propto 1/E_B$ is so far purely empirical, but it should be possible to calculate $\eta_*(E_B)$ in a rigorous manner, as the properties of the involved trimers are precisely known [Bar05]. The results of the last sections are published in [Wen09a].

6.6 Efimov physics in ultracold gases of ^{6}Li atoms

This section gives a concluding overview of the occurrence of Efimov physics in a system of ultracold atoms in the three lowest Zeeman substates states of ^{6}Li.

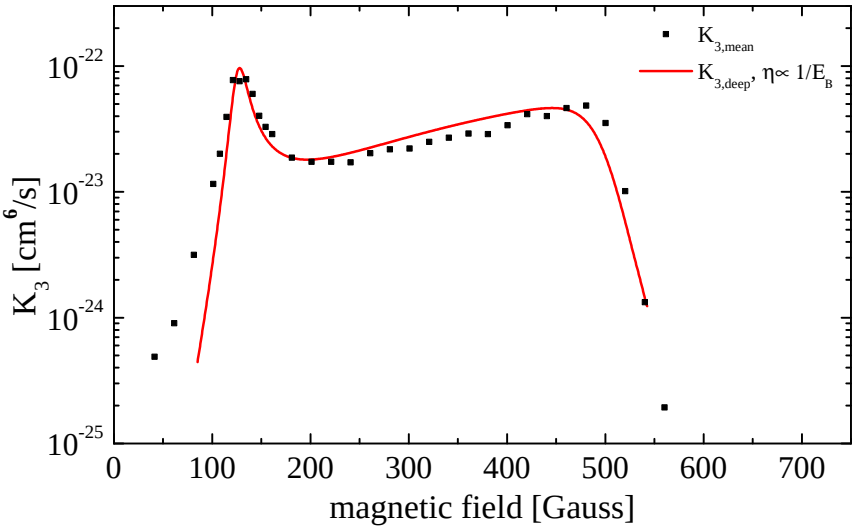

Figure 6.11: The red solid line shows the fitted behaviour of three-body loss coefficients according to equation 6.7 under the assumption of a magnetic field dependence of the elasticity parameter η_*. Assuming a simple scaling of $\eta_* \propto 1/E_B$, where E_B is the binding energy of the highest dimers, yields very good agreement with the measured data. Thus, the trimer itself can be described in a universal framework, while its decay is determined by the properties of non-universal dimers.

In the last sections it was discussed how the observed rate of three-body loss in the magnetic field region below 600 G, the so-called low-field region, can be explained by the presence of an Efimov-like trimer state consisting of atoms in each of the three spin states. This trimer state crosses the three atom continuum twice, at 130 G and around 500 G. Additionally, it was demonstrated that lower lying (non-universal) dimer states have significant influence on the width of the observed loss resonances. In our case, these dimer states are precisely known and their binding energies vary substantially over the magnetic field range where the trimer exists. This leads to a broadening of the second loss resonance. Thus, the properties of the trimer state can be fully described in a universal framework, while its decay is determined by properties of non-universal lower-lying dimer states. The scenario is depicted in figure 6.10.

The high-field region above 600 G is subject of current experimental and theoretical investigations. J.R. Williams et al. [Wil09] found evidence for the first excited Efimov-trimer intersecting the free atom threshold near 895 G. E. Braaten et al. give a thorough review on Efimov physics in ^{6}Li atoms [Bra09a]. They use the three-body parameter determined in [Wil09] and calculate the spectrum of Efimov states and three-body recombination rates in the universal region above

600 G. The spectrum of bound states is shown in figure 6.12. The lowest trimer state corresponding to the one already identified in the low field region does not cross the free atom threshold at higher magnetic fields, as the scattering lengths converge to a large negative value of 2100 a_0. Thus, the state stays always below the free atom scattering continuum. The first excited Efimov state crosses the free atom threshold at about 895 G which was already observed in an enhanced three-body recombination rate in the group of K.M. O'Hara [Wil09]. At about 672 G

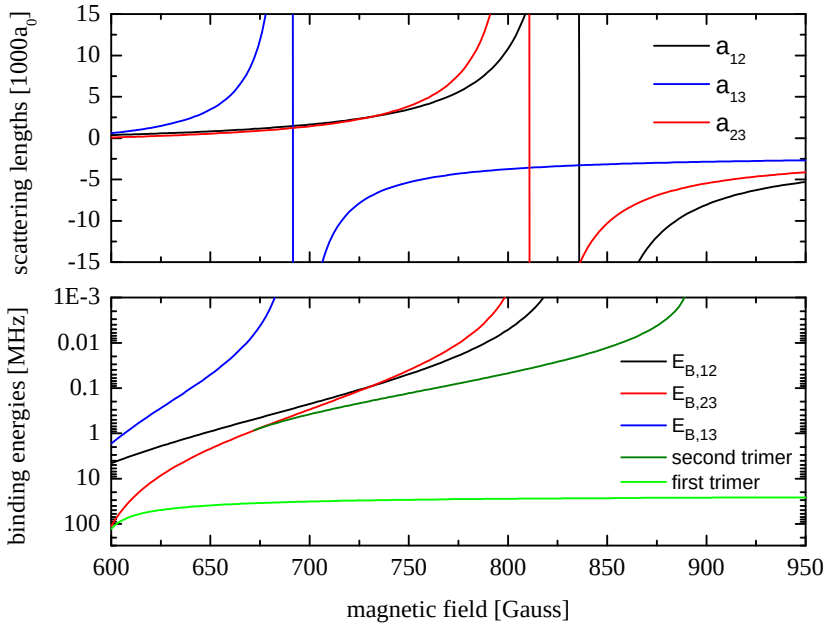

Figure 6.12: Upper Panel: Behaviour of the scattering lengths in the high-field region. Note that all scattering lengths converge to the large triplet background scattering length of 2100 a_0 at high fields. Lower panel: Spectrum of bound states in the high-field region above 600 G. Shown are the three atom-dimer thresholds associated with the three broad Feshbach resonances. The lowest Efimov-like trimer state never crosses the free atom threshold as the scattering lengths converge to a large negative value, but vanishes through the $|1\rangle - |23\rangle$ atom-dimer threshold at around 600 G. The first excited Efimov state intersects the three atom threshold near 895 G, which was observed as a resonant enhancement of three-body loss in the group of K.M. O'Hara [Wil09]. This state disappears also through the $|1\rangle - |23\rangle$ atom-dimer threshold at a field value of about 672 G what should be observable in a resonant enhancement of atom-dimer losses at this magnetic field value. The graph is adapted from [Bra09a].

this state vanishes through the $|1\rangle - |23\rangle$ atom-dimer threshold which should be observable in a resonant enhancement of atom-dimer losses at this magnetic field

value. Thus, there is still experimental work to be done to study the occurrence of Efimov physics in an ultracold mixture of atoms in the three lowest spin states of ^{6}Li. If possible, the most exciting result would be a spectroscopic measurement of the binding energy of an Efimov trimer.

Chapter 7

From the thermodynamic limit to physics in a finite system

In recent years several experimental and theoretical [Dud07, Pon09, Rai09] efforts have been made towards an atomic system consisting of a definite number of particles. Number squeezing which means the reduction of atomic number fluctuations below the shot noise limit was observed in optical lattices [Orz01, Ger06] as well as in a single well trap [Chu05]. In optical lattices also shells with a definite number of occupants in individual wells were observed [Cam06, Foe06]. All these experiments were performed with bosonic particles.

An ensemble of a controlled number of deeply degenerate fermions in a single well trap will form a clean model system for finite Fermi systems in nature as for example atomic nuclei. In this chapter our approach for the preparation of a deeply degenerate Fermi gas consisting of a finite and controlled number of ^{6}Li atoms is presented. A similar approach which aims for the initialization of a high fidelity qubit consisting of two fermionic atoms in the ground state of an optical dipole trap was developed in [Rai09].

This chapter is organized as follows: First a motivation is given why the experimental realization of such a system is desirable and how it can contribute to a better understanding in other fields of physics. After that the experimental challenges that have to be overcome in the preparation of such a system are discussed and our approach to deal with these problems is presented. In the last section an estimate of the required experimental parameters is given.

7.1 Motivation

Few-body physics in ultracold gases usually deals with collisional processes where only few atoms are involved in a single event. As discussed in the preceding chap-

ters experiments studying such processes work with a large ensemble of atoms and a typical observable is the loss of atoms. In a different point of view, few-body physics is the physics of systems consisting only of a few number of particles. A prominent example of such systems in nature is the atomic nucleus which consists of a finite number of protons and neutrons.

In the last decade ultracold Fermi gases turned out to be a magnificent model system for large systems that can be described in the thermodynamic limit as electrons in a metal or in a superconductor and helped a lot to understand the underlying physics. For an overview see [Ket08]. The techniques developed in these experiments make it now possible to prepare a deeply degenerate ensemble of ultracold fermions consisting only of a finite and controlled number of atoms.

Due to the easy manipulation of ultracold atoms for example with radio frequency fields and the ability to tune the interparticle interactions by means of Feshbach resonances, such a finite gas will be a fascinating playground and may contribute considerably to the understanding of finite fermionic systems in nature.

There are a lot of open questions in the physics of few-body physics:

a) What is the energy of the system in dependence on interaction between the constituents and the number of particles [Zin09]?

b) How does pairing in a finite Fermi system occur [Hei03, Bru02]?

c) Is there a superfluid phase and how many particles are needed to for a superfluid? [Mig59].

A detailed overview of physics in finite Fermi systems can be found in [Mig67, Bri05].

Towards the experimental realization of a finite deeply degenerate system of fermionic atoms, several challenges have to be overcome. What these challenges are and how we are going to overcome them is described in the following section.

7.2 Our approach towards a finite system of ultracold fermions

Our approach for the preparation of a finite system of ultracold fermions in an optical dipole trap involves three main steps:

1. A large ensemble of ^{6}Li atoms in the two lowest Zeeman substates has to be prepared. This is done in the large volume crossed-beam optical dipole trap by employing standard evaporative cooling schemes that allow to prepare samples of about 10^5 atoms in each spin state at a temperature of a few percent of the Fermi temperature [O'H02b].

2. Transfer (a part) of the atoms into a small microtrap with high trapping frequencies

3. Spill atoms from the microtrap in a controlled way by applying an external magnetic field gradient.

In steps two and three the so called microtrap which is established by a tightly focused laser beam (see 4.3.3) plays the central role. It fulfills two major tasks. By transferring the atoms into the microtrap the degeneracy of the system is considerably increased. This so-called dimple trick was firstly applied for reaching high phase space densities in Bose gases [Pin97, SK98].

During evaporation in the large volume trap the microtrap is already present. The microtrap gets populated by collisions between the particles leading to thermal equilibration between both traps. Thus, the temperature of the system is determined by the large trap which acts as a reservoir. As soon as the evaporation is finished the large volume trap is adiabatically switched off and the scattering length can be tuned to arbitrary values by means of the Feshbach resonance.

The degeneracy that is achievable in the microtrap for an ideal Fermi gas can easily be estimated using expression 2.3 for the Fermi energy in a harmonic oscillator. For the ratio of the degeneracy in the microtrap and the large volume trap one gets

$$\frac{T/T_{F,mt}}{T/T_{F,lt}} = \left(\frac{N_{lt}}{N_{mt}}\right)^{1/3} \frac{\bar{\omega}_{lt}}{\bar{\omega}_{mt}} \tag{7.1}$$

where N_{lt}, N_{mt} and $\bar{\omega}_{lt}$, $\bar{\omega}_{mt}$ are the atom numbers and mean trapping frequencies in the large volume trap and the microtrap respectively. For typical experimental parameters in our setup (see 4.3 and 8.1) of $N_{lt} = 10^5$, $N_{mt} = 5000$ and $\bar{\omega}_{lt} = 2\pi\times160\,Hz$, $\bar{\omega}_{mt} = 2\pi\times2.9\,kHz$ and a temperature of 200 nK, this means that the degeneracy is increased by about a factor of six from $0.02\,T/T_F$ to $0.045\,T/T_F$. This is a rather conservative estimate based on parameters we have worked with so far. In principle, it is feasible to prepare a gas with a much deeper degeneracy of about $0.05\,T/T_F$ in the large trap [Ket08] which would result in an extreme degeneracy of of less than $0.01\,T/T_F$ in the microtrap.

Yet, this estimate assumed full equilibration between both traps which is not experimentally tested so far. Thermalization rates will for example depend on the spatial overlap of the traps and the collision rate of particles. Major difficulty in the measurement of thermalization rates is the determination of T/T_F in the microtrap, as information about the degeneracy is contained in the outer tails of the density distribution which are hard to observe (see 2.1). Studying the thermalization process will be a challenging future experiment.

Once the sample is prepared in the microtrap, atoms can be spilled from the trap by applying an external magnetic field gradient. Due to the magnetic moment of

^{6}Li atoms of one μ_B, this gradient acts a a linear potential which is superimposed on the trapping potential. A sketch of the spilling process is shown in figure 7.1. When the separation of the energy levels in the trapping beam is large enough, it is possible to control the atom number in the trap by the strength of the field gradient. Aim of this experiment is the preparation of a finite Fermi gas consisting of about

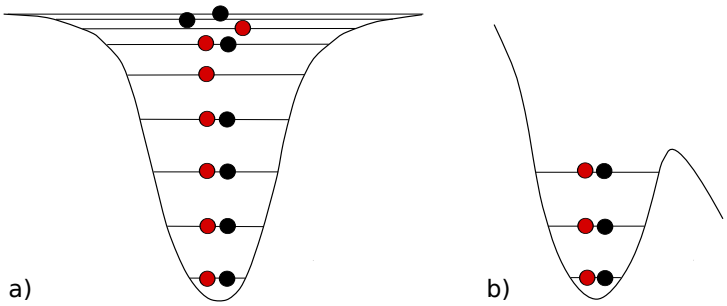

Figure 7.1: a) Schematic picture of a Gaussian beam trap filled with atoms in two different spin states up to the anharmonic part. b) By using an external magnetic field gradient the depth of the trap is reduced. When the separation of energy levels is large enough, the number of remaining particles can be controlled by the strength of the gradient.

100 atoms or even less ideally without unoccupied states up to the Fermi energy. The probability for such an unoccupied state can be estimated using the Fermi-Dirac distribution. In a Fermi gas consisting of N atoms with a given degeneracy the probability for at least one unoccupied state (also called hole) in the lowest N^* states is given by

$$p_{hole}(N^*, N, T/T_F) = \tag{7.2}$$
$$1 - \prod_{i=1}^{N^*} \left(\exp\left[\left(\frac{T}{T_F}\right)^{-1} \left(\left(\frac{i}{N}\right)^{(1/3)} - \left(1 - \frac{\pi^2}{3}\left(\frac{T}{T_F}\right)^2\right)\right)\right] + 1\right)^{-1}$$

where for the chemical potential the Sommerfeld expansion (see 2.6) to lowest order was used. Figure 7.2 shows the probability for a hole in the lowest 100 states for a total atom number of 5000 atoms in dependence of the degeneracy. For $T/T_F = 0.04$ the probability for a hole is 1.4×10^{-6}.

Thus, if the assumption of full thermalization between the large trap and the microtrap holds and a method is found to remove excess particles without disturbing the system, it is possible to prepare a Fermi gas consisting of a finite number of atoms in its absolute ground state with extremely high probability. However, besides thermalization there are a couple of additional experimental limitations as for example intensity noise in the trapping beam and beam pointing instabilities which will lead to heating of the sample. Also photon scattering from the

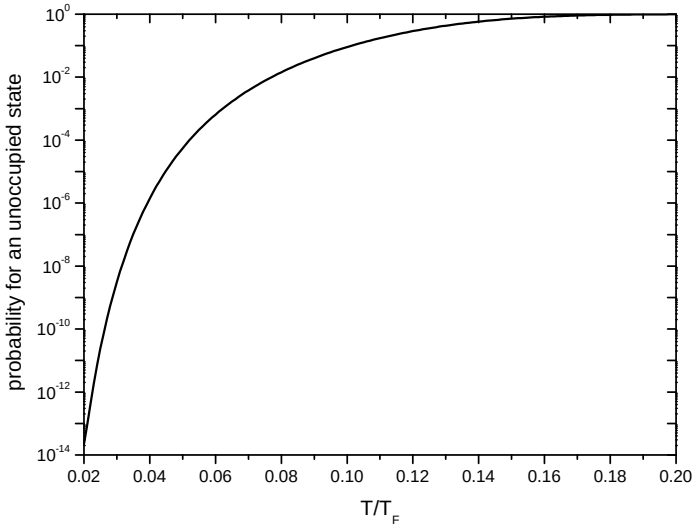

Figure 7.2: Probability for a hole in the lowest 100 states for a total atom number of 5000 in dependence of the degeneracy.

trapping beam and collisions with residual background gas will create additional holes. Yet, these numbers are absolutely encouraging to do the experiment.

7.3 Spilling atoms from the microtrap - an estimate of tunneling rates

In this section an estimate of tunneling rates from the tilted microtrap potential is presented. For the preparation of a Fock state[1] with high fidelity it is crucial that subsequent states in the tilted trap have sufficiently different tunneling rates. Two requirements have to be fulfilled: the lifetime of the highest energy state must be much smaller than the lifetime of the next lower lying state and the lifetime of this lower state must be sufficiently large compared to the timescale of the experiment.
The field gradient for tilting the trap is generated by a pair of coils in anti-Helmholtz configuration. In the center of the coils the field can be approximated by a constant magnetic field gradient along the symmetry axis and by constant gradients with half the strength in the plane parallel to the coils. As in the symmetry axis which coincides with the weak axis of the trap a high offset field is applied to make use of the Feshbach resonance the gradients perpendicular to the offset field can be neglected in most cases. Thus, the trap is essentially tilted only in one dimension along its weak axis. The potential of the tilted microtrap is given

[1] A Fock state denotes a state with well defined atom number.

by the following expression

$$V(r,z) = V_0 \left(1 - \frac{e^{-2r^2/w(z)^2}}{1+(z/z_R)^2} \right) + \mu \frac{dB}{dz} z \tag{7.3}$$

where $z_R = \pi w_0^2/\lambda$, $w(z) = w_0\sqrt{1+(z/z_r)^2}$ and w_0 are the Rayleigh range, the divergence and the minimal $1/e^2$ radius of the trapping beam respectively. μ denotes the magnetic moment of the atoms which is $1\mu_B$ for ^{6}Li.

A simple estimate of tunneling rates was done using the one dimensional WKB approximation. For an overview of WKB see for example [Mer98]. Figure 7.3 shows the potential curve along the tilted axis of the trap. The calculation of

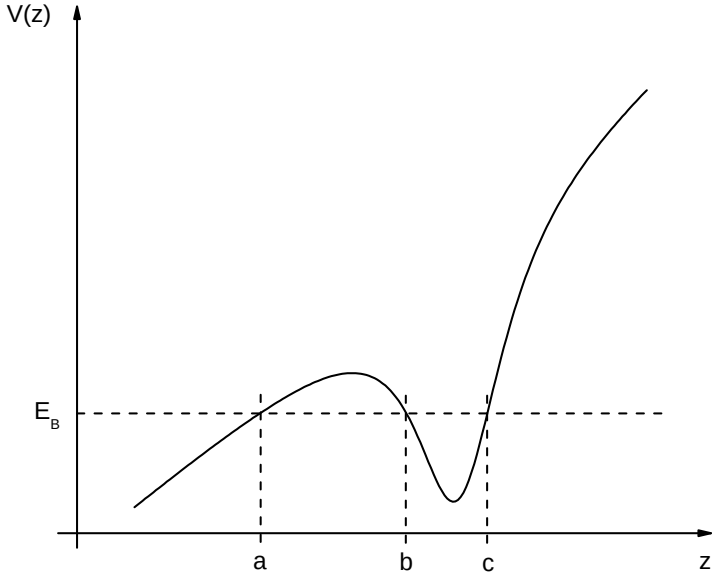

Figure 7.3: Tilted potential along the weak axis of the trap. E_B is the energy of a bound state in the trap. a, b and c denote integral limits for WKB integrals in the calculation of tunneling rates.

the tunneling rates is done in two steps: First the energy of bound states in the potential well is calculated, then the width of the state which is related to the lifetime of a particle in the trap is determined.

For a given energy E the z-axis can be divided into classically allowed $(E > V)$ and classically forbidden regions $(E < V)$. In these distinct regions it is useful to

define the following abbreviations

$$k(z) = \sqrt{\frac{2m}{\hbar^2}\Big(E - V(z)\Big)}, \qquad \Big(E > V(z)\Big) \tag{7.4}$$
$$\kappa(z) = \sqrt{\frac{2m}{\hbar^2}\Big(V(z) - E\Big)}, \qquad \Big(E < V(z)\Big)$$

and integrals

$$L(E) := \int_b^c k(z)dz \qquad\qquad \theta(E) := \int_a^b \kappa(z)dz \tag{7.5}$$

where the integration limits are given by the classical turning points a, b and c which depend on the energy E.

The energy of bound states in the potential well are determined by the condition

$$L(E) = \left(n + \frac{1}{2}\right)\pi. \tag{7.6}$$

For the lifetime of a particle in such a bound state two parameters are important. The first one is the so-called Gamow factor which expresses the probability for a particle with energy E to penetrate a potential barrier and is defined by

$$G(E) = \exp\Big(-2\,\theta(E)\Big). \tag{7.7}$$

Simply speaking, this Gamow factor describes the decrease of the amplitude of the wavefunction in the barrier. The second parameter is given by the derivative of $L(E)$ with respect to the energy. Physically, this factor can be interpreted as the rate with which the particle hits the potential barrier. Indeed, for a harmonic oscillator potential $L(E)$ is a linearly increasing function of the energy whose slope is given by the inverse trapping frequency. Thus, the lifetime of a particle inside a potential well can be estimated to be

$$\tau = \hbar\, G(E) \left(\frac{\partial L}{\partial E}\right)_{E=E_B} \tag{7.8}$$

where E_B is the energy of the bound state.

The lifetime of the lowest states has been calculated for several parameters of the trapping potential. The results are shown in figure 7.4. Parts a) and b) combine the results for our microtrap under typical experimental parameters. The measured

axial trapping frequencies in the microtrap are consistent with a Rayleigh range of 73 μm which was used for the calculation.

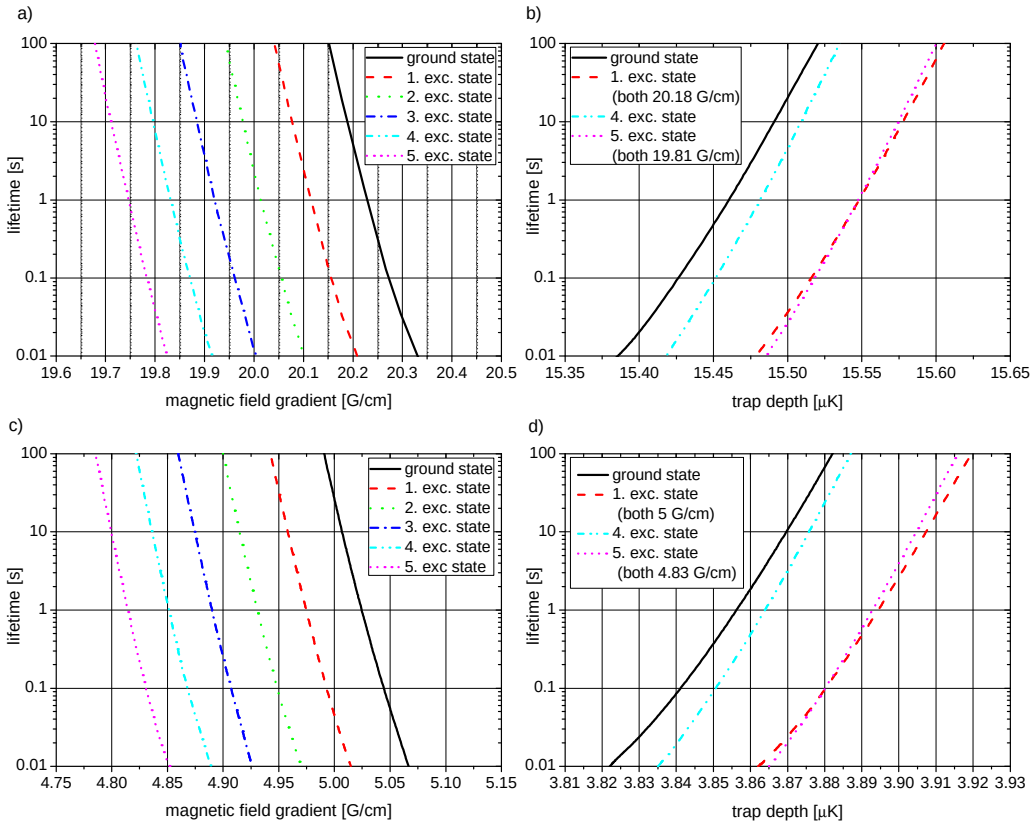

Figure 7.4: One dimensional WKB results for the lifetime of the lowest states in the tilted microtrap potential for two different trap depths: a) Lifetime for the lowest six states in our microtrap in dependence of the magnetic field gradient. The trap depth is 15.5 μK and the axial trapping frequency is 450 Hz ($\omega_r = 10.6$ kHz). b) Lifetime in dependence of the trap depth for a fixed field gradient. For the ground and first excited state the field gradient was chosen to be 20.18 G/cm and for the fourth and fifth excited state 19.81 G/cm. c) and d): WKB results for the same trap but the trap depth has been decreased by a factor of four to about 3.9 μK resulting in half the trapping frequencies. ($\omega_a = 225$ Hz and $\omega_r = 5.3$ kHz). Comparison with a) and b) shows that the magnetic field gradient necessary for controlling the number of states in the trap scales with the trap depth, while the sensitivity of the lifetimes on the field gradient and the trap depth scale with the trapping frequency. Thus, high trapping frequencies are desired. More details can be found in the text.

In a) the lifetime of the six lowest states in the trap is shown in dependence of the applied magnetic field gradient. The trap depth for the data shown is 15.5 μK and the axial and radial trapping frequencies in the trap are $\omega_a = 450$ Hz and $\omega_r = 10.6$ kHz. The lifetime of each state varies over four orders of magnitude when the field gradient is changed about 150 mG/cm. To control the atom number in the trap the field gradient must be controlled on the order of 50 mG/cm, what seems feasible in our current setup. For a gradient of 19.8 ± 0.025 G/cm the lifetime of the fourth excited state is between thirty ms and one second, whereas the lifetime of the fifth excited state is one hundred times smaller. This should be observable in the experiment. The second crucial issue in the preparation of a state

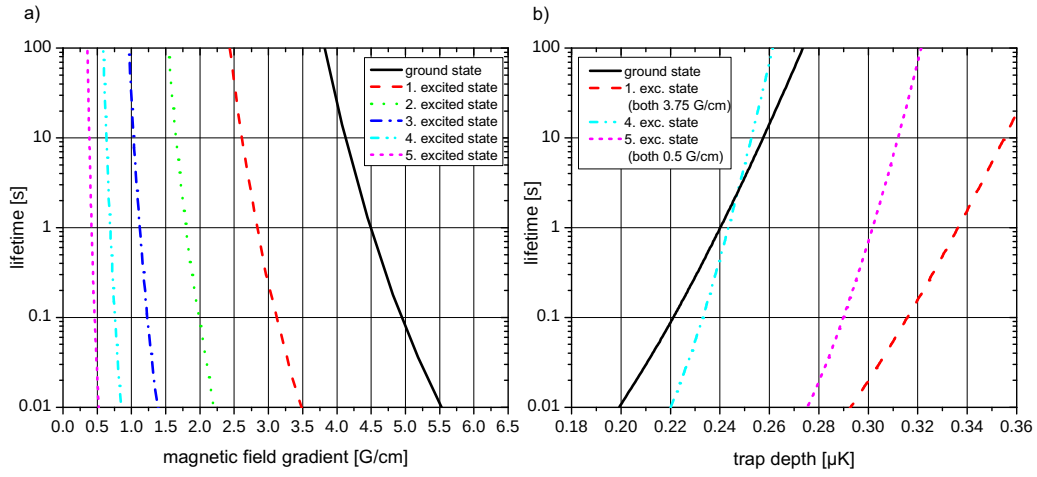

Figure 7.5: WKB results for a Gaussian beam trap with a waist of 1 μm and a trap depth of 280 nK. Trapping frequencies are $\omega_a = 1.5$ kHz and $\omega_r = 6.3$ kHz. Even in this very shallow trap it should be possible to prepare a number state with high fidelity. The change in the slope of the lifetime curves for different states in a) is due to the anharmonicity of this shallow trap.

with defined atom number is the stability of the optical trap. In part b) the lifetime of four states is shown in dependence of the trap depth for fixed field gradients. For the ground and first excited state the gradient was chosen to be 20.18 G/cm and 19.81 G/cm for the fourth and fifth excited state. For fixed trap depth the lifetime of two consecutive states differ by more than two orders of magnitude. The lifetime of a single state changes about two orders of magnitude when the trap depth is changed by 50 nK. This means that the intensity stabilization of the trapping beam must be on the order of 10^{-3} what is experimentally feasible. Thus, it seems that our current microtrap can be used for the preparation of an atomic number state.

To get an intuition for the scaling of the required experimental parameters, parts c) and d) show the corresponding lifetimes when the trap depth is reduced by a factor of four compared to a) and b). As the trapping frequencies scale with the square root of the trap depth, they are reduced by a factor of two. Having this in mind, it is instructive to compare both cases.

The magnetic field gradient which is necessary to control the number of states in the trap scales linearly with the trap depth, while the sensitivity of the lifetime on the magnetic field gradient and the trap depth scales with the trapping frequency. Thus, in order to prepare a number state under controlled conditions high trapping frequencies are desired. These can in principle be achieved by increasing the depth of the trap, but as mentioned above the trapping frequencies increase only with the square root of the trap depth. Therefore, it is more efficient to reduce the size of the trap, as the axial trapping frequency scales inversely with the square of beam waist when the trap depth is kept constant. This is a direct consequence of equation 4.15.

For this reason, a custom objective is currently under construction which is capable of generating a focus with a waist of 1 μm. In figure 7.5 the WKB results for the 1 μm trap are shown for a very shallow trap of 280 nK. The axial trapping frequency is 1.5 kHz ($\omega_r = 6.3$ kHz). Even in this shallow trap it is possible to control the atom number under controlled conditions. The magnetic field gradient and the stability of the optical trap are much less critical compared to our current microtrap. Furthermore, the ratio of lifetimes for constant magnetic field gradient and constant trap depth is larger than 10^4. Thus, in such a trap it should be much easier to prepare a number state with very high fidelity. Our first experimental steps towards a finite system with controlled atom number are presented in the next chapter.

Chapter 8

Approaching the finite Fermi gas: First experiments

This chapter describes the first experiments performed with the microtrap and presents current progress on the way towards a finite deeply degenerate Fermi gas. The setup of the microtrap is described in 4.3.3. The first part of this chapter describes briefly how a sample of fermions is prepared in the microtrap and gives an overview of the properties of this trap. Then it is shown how atoms can be spilled from the trap by applying an external magnetic field gradient and to what extend we gained control over the atom number in the current setup. In the last part it is demonstrated how single atoms can be detected by fluorescence imaging.

8.1 The microtrap at work

The microtrap is the most crucial tool for the preparation of a highly degenerate Fermi gas consisting of a finite number of particles. It helps to overcome two challenges: Firstly, the degeneracy of the gas is considerably increased by transferring the atoms from the large volume trap into the microtrap. Secondly, due to the high trapping frequencies the level spacing is sufficiently large and allows for a control of the atom number in the trap by applying an external magnetic field gradient.

After implementation of all experimental tools necessary for the microtrap, the trapping beam had to be overlapped with the large dipole trap. Due to the small focus of 3 μm of the microtrap beam, this turned out to be a difficult task. Gerhard Zürn developed an elaborate overlapping scheme which is described in detail in his diploma thesis [Zue09].

For transferring atoms into the microtrap, the trapping beam is already switched on during evaporation in the large volume trap. The first evaporation step is in

most cases done at a magnetic field of 760 G where the scattering length has a large and positive value of 4000 a_0. Before molecule formation sets in, the magnetic field was tuned to 300 G where the scattering length is negative (see 2.3) and no weakly bound dimer state is present. This is essential if a non-interacting two-component sample at the zero crossing of the scattering length is desired. Ramping the field directly to the zero crossings with molecules in the sample would result in dramatic losses due to collisional relaxation of the molecules. During evaporation at 300 G atoms accumulate in the microtrap while the large volume trap acts as a reservoir. Atoms in the microtrap collide with particles in the large volume trap such that both subsystems are in thermal equilibrium. After the evaporation is finished the atoms in the large volume trap are removed by adiabatically ramping down the light intensity in the crossed-beam dipole trap within 100 ms. Absorption images of the transfer are presented in figure 8.1

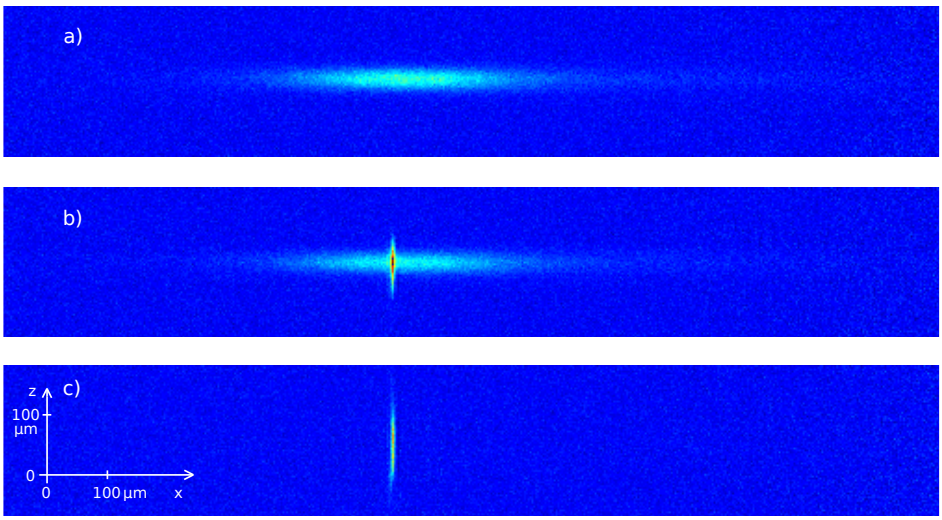

Figure 8.1: Absorption images of the transfer between large volume trap and microtrap. a) Large cloud of atoms in the crossed dipole trap. The faint wings of the density distribution in horizontal direction arise from atoms that are trapped in the single beams. b) Both traps switched on. The microtrap is nicely visible as a strong enhancement of density in the microtrap beam. c) Atoms in the microtrap after switching off the large volume trap.

Typical atom numbers in the large volume trap are about 1.5×10^5 atoms per spin state at a temperature of 200 nK. Plugging this atom number and the trapping frequencies of ω_r=$2\pi \times 360$ Hz and $\omega_a = 2\pi \times 33$ Hz into Equation 2.3 yields a Fermi temperature of 750 nK and a degeneracy of about 0.27 T/T_F in the large volume trap. For a typical atom number of 5000 particles in the microtrap at the same temperature and trapping frequencies of $\omega_{r,mt} = 2\pi \times 8.3$ kHz and

$\omega_{a,mt} = 2\pi \times 350$ Hz the calculated degeneracy is $0.05\,T/T_F$. Thus, just by transferring atoms from the shallow dipole trap into the microtrap more than a factor of five is gained in degeneracy under the assumption of full equilibration between both traps. Unfortunately, measuring the degeneracy in the experiment is a quite difficult task as described in 2.1 and [Wen09b] and is currently investigated in our group. An estimate for the degeneracy based on studying the decay of the sample in the microtrap trap at negative scattering length resulted in a degeneracy of $0.14\,T/T_F$ [Zue09].

The measurement of the trapping frequencies in the microtrap was already discussed in 4.3.3. It was shown that the trapping frequencies in radial and axial direction in dependence of the beam power in mW are given by $\omega_r = 2\pi \times 3.79\,kHz \times \sqrt{P}$ and $\omega_a = 2\pi \times 160\,Hz \times \sqrt{P}$.

The lifetime of atoms in the microtrap is a crucial parameter for experiments. The lifetime was measured for several trap depths at the zero crossing of the scattering length at 530 G to avoid inelastic losses due to two- or three-body processes. Figure 8.2 shows lifetime curves for three different trapping beam powers. The atom loss can be nicely fitted with an exponential decay indicating a one-body loss process. Photon scattering rates in the trap can be calculated to be $0.029\,\mathrm{s}^{-1}$, $0.073\,\mathrm{s}^{-1}$ and $0.148\,\mathrm{s}^{-1}$ for the measured beam powers which would lead to lifetimes of 35.5 s, 13.5 s and 6.8 s under the assumption that each scattering event causes an atom to leave the trap. Compared to the trap depths of 100 μK, 50 μK and 20 μK a single photon recoil of 1.6 μK cannot cause an atom to leave the trap after a single scattering event. Thus, additional heating processes like power or beam steering instabilities influence the lifetime of the atoms in the microtrap. However, the observed lifetimes are still long enough for experiments.

8.2 Spilling atoms from the microtrap

In a first set of experiments we studied how atoms can be spilled from the trap by applying an external magnetic field gradient. Due to the magnetic moment of the ^{6}Li atoms of $1\mu_B$, the gradient acts as a linear potential that is superimposed on the trap. For a more detailed description of our approach see 7.2

A maximum gradient of 40 G/cm in the axial direction of the microtrap can be generated by the quadrupole coils of the magneto-optical trap which is enough for the experiments described in this chapter. Due to the high offset field of 530 G that is generated by the Feshbach coils in the axial direction the radial gradient that is generated by the MOT coils has negligible effect. Thus, the gradient is applied only in the axial direction of the microtrap and leads to a tilt of the trap as discussed in chapter 7.

The experiment was performed as follows: A balanced mixture of the two low-

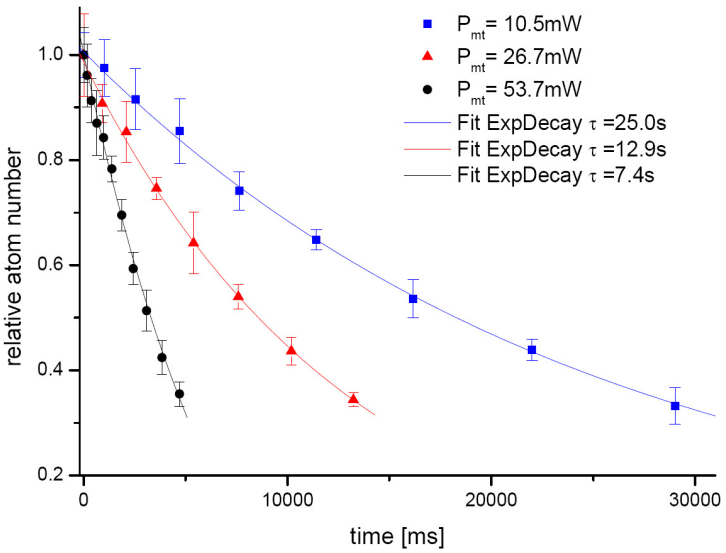

Figure 8.2: Lifetime curves for atoms in the microtrap at three-different trap depths. The behaviour of atom loss is nicely fitted by an exponential decay indicating that the loss is a one-body process. As the fitted lifetime is inversely proportional to the beam power, photon scattering seems to be the dominant loss process.

est Zeeman substates states was prepared in the microtrap under the same experimental conditions as described in 8.1: 5000 atoms per state, $T \approx 200\,\mathrm{nK}$, $\omega_{r,mt} = 2\pi \times 8.3\,\mathrm{kHz}$, $\omega_{a,mt} = 2\pi \times 350\,\mathrm{Hz}$ and a trap depth of $9.5\,\mu\mathrm{K}$. Then the magnetic field gradient was tuned to the desired value within 50 ms which is adiabatic with respect to the axial trapping frequency of the microtrap. Then the gradient was ramped down again in 50 ms and the remaining number of atoms was recorded by absorption imaging. The result is shown in figure 8.3.

This shows that atoms can be removed from the trap by applying an external magnetic field gradient, the crucial question is how well the atom number can be controlled using this technique. To get quantitative information about the uncertainty in the prepared atom number the experiment was repeated more than two hundred times with trapping frequencies of $\omega_r = 2\pi \times 12.1\,\mathrm{kHz}$, $\omega_{a,mt} = 2\pi \times 510\,\mathrm{Hz}$, a trap depth of $20\,\mu\mathrm{K}$ and a magnetic field gradient of 18.6 G/cm. The number of atoms was determined by absorption imaging. Figure 8.4 shows the observed atom number statistics. The distribution is fitted well with a Gaussian distribution with a mean value of 120 atoms and a standard deviation of 11 atoms. Thus, the uncertainty of the atom number is given by the square root of the mean corresponding to Poissonian number statistics. Although there is still a lot of work to do until it is possible to prepare a Fock state with deterministic atom number this

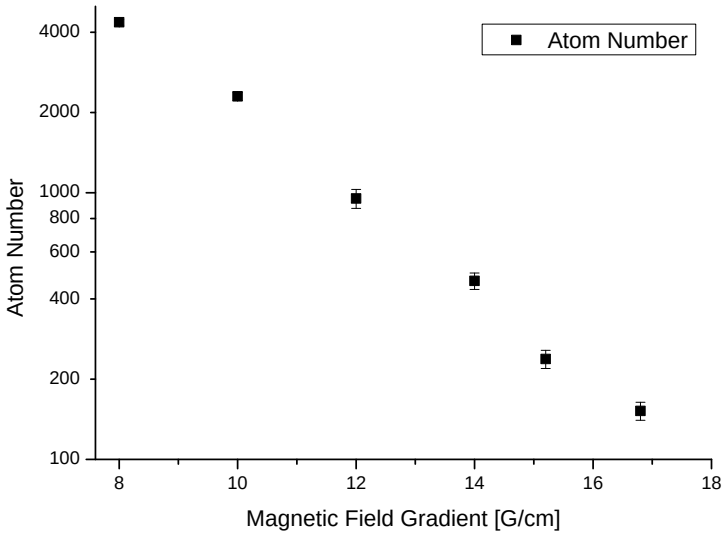

Figure 8.3: Atoms can be spilled from the microtrap by applying an external magnetic field gradient. Shown is the number of atoms remaining in the microtrap after ramping up the field gradient to the desired value within 50 ms. The atom number was recorded by absorption imaging after ramping down the field gradient again in 50 ms. The error bars show statistical errors from several measurements. Parameters of the microtrap were: $\omega_{r,mt} = 2\pi \times 8.3\,\mathrm{kHz}$, $\omega_{a,mt} = 2\pi \times 350\,\mathrm{Hz}$ and a trap depth of 9.5 μK.

result shows that we are on a good way.

Some care has to be taken in the interpretation of the presented data. A crucial issue in experiments with few atoms is the imaging technique. In this experiment, we applied absorption imaging to count the number of atoms in the microtrap. A short time of flight of 50 μs was applied to reduce the atomic density and the used light intensity was much smaller than the saturation intensity. However, there are still doubts about the accuracy of the atom number if light atoms as ^{6}Li are imaged using this technique. Momentum transfer during the scattering process accelerates the atoms and the corresponding Doppler shift changes the scattering rate. This leads on the one hand to a systematic error in the atom number and on the other hand to an additional contribution to the atom number uncertainty due to the isotropic emission of scattered photons. Also photon shot noise in the imaging beam can affect the observed number statistics. Thus, fluorescence imaging is a much better choice to detect small atom numbers with high fidelity. Our progress in the detection of few atoms using fluorescence imaging is described in the next section.

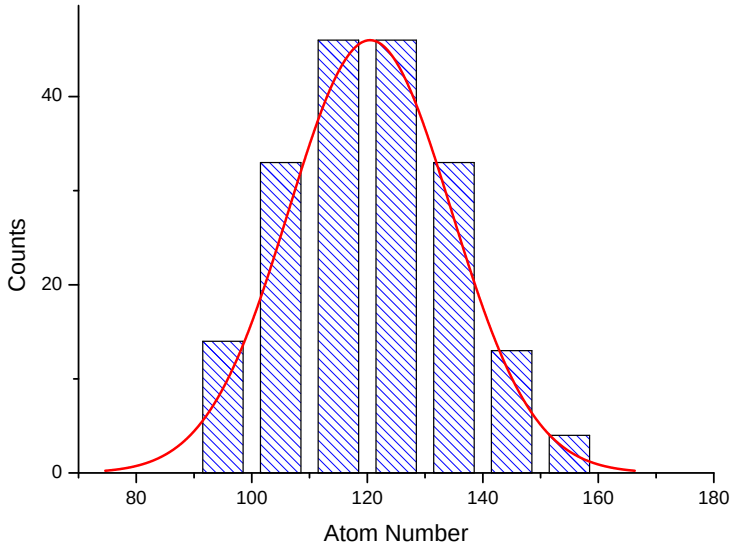

Figure 8.4: Observed atom number statistics after applying a magnetic field gradient of 18.6 G/cm. The experiment was repeated more than 200 times and the atom number was determined by absorption imaging. The resulting distribution is of Gaussian shape with a mean value of 120 atoms and a standard deviation of 11 atoms.

8.3 Single atom detection using fluorescence imaging

To overcome the limitations of absorption imaging in atom number determination, fluorescence imaging will be used in future experiments. The experimental protocol is as follows: The sample is prepared in the microtrap as discussed above. Then the atoms are recaptured in the MOT and their fluorescence is collected with a large numerical aperture lens and projected onto a CCD camera. From the amount of the scattered light the atom number can be determined with high fidelity. The setup used for fluorescence imaging is described in 4.2.4.

For single atom detection a critical issue is the suppression of stray light. The signal on the camera due to stray light must be much smaller than the fluorescence of a single atom. In order to test whether it is possible to detect single atoms with our current setup we did a benchmark experiment with single atoms in the MOT. To suppress stray light the diameter of the MOT beams was made smaller by putting irises into the beam path. It turned out that a size of about 7 mm in diameter is optimal. This is large enough to ensure easy alignment of the MOT beams and small enough for sufficient suppression of stray light.

For loading single atoms into the MOT the loading parameters had to be modi-

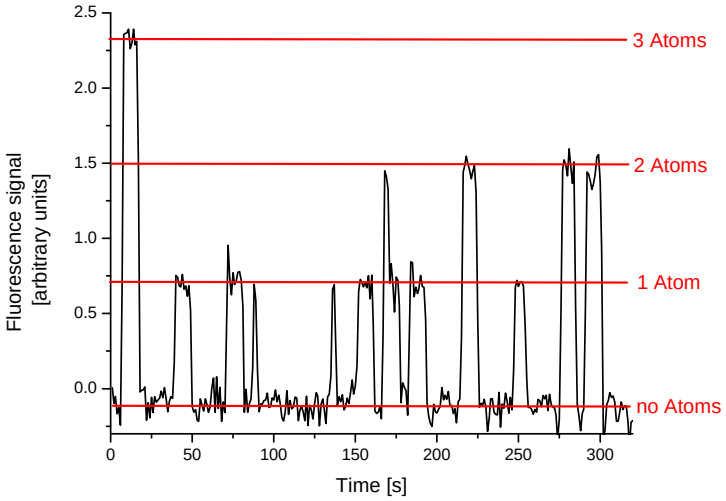

Figure 8.5: Steps in the fluorescence signal demonstrate that we are able to detect single atoms in the MOT. The amount of fluorescence light is shown arbitrary units. The atoms were held in the MOT for 1 s, then the MOT was cleared and the experiment started again as described in the text. The graph shows the amount of fluorescence over several experimental cycles.

fied. For this experiment the Zeeman slower was switched off, the loading time was reduced to 100 ms and the oven shutter was closed after the loading phase. The frequency of the MOT lasers was 10 MHz $\sim 2\gamma$ red detuned from resonance and the overall light intensity in all beams was about 20 times the saturation intensity of 2.54 W/cm^2. After closing the oven shutter the atoms were held for 1 s in the MOT and their fluorescence was collected on the CCD camera. Then the MOT beams were switched off to remove the atoms from the trap and the experiment was started again. The fluorescence detected on the CCD camera for several experimental cycles is shown in figure 8.5.

The steps in the signal clearly reveal the presence of single atoms in the MOT and demonstrates that we are able to detect single atoms by fluorescence imaging. Naturally, the next step will be the combination of microtrap and fluorescence imaging in order to determine the atom number with high fidelity. To do so, irises were built whose size can be adjusted during the experimental cycle by means of servo motors. Thus, for loading the MOT and transferring the atoms into the crossed-beam dipole trap large beams can be used while for fluorescence imaging the beam size can be reduced by closing the irises for suppression of stray light. These will be implemented in the setup soon.

Chapter 9

Conclusion and outlook

9.1 Three-component Fermi gases: A new playground

This PhD project started in January 2007 with an empty lab. The first year was mainly devoted to the construction of a new experimental setup that is capable of preparing ensembles of ultracold gases consisting of fermionic ^{6}Li atoms. Milestones in this period were the first cloud of laser cooled atoms in the magneto-optical trap in May and the preparation of a Bose-Einstein condensate of $^6Li_2$ molecules in January 2008. The first successful preparation of a BEC in our setup showed that we had gained control over the setup and that we were now ready for new experiments with ultracold atoms.

Inspired by discussions with Chris Greene who, among others, raised the question about the stability of a three-component Fermi gas for strong interactions [Blu08], we decided to play around with our setup and see whether we could prepare such a three-component gas. So far, most experiments had been performed only with atoms in the two lowest hyperfine states of ^{6}Li and populating the third state seemed difficult due to strong inelastic losses caused by three-body recombination. Thus, the first task was to develop a scheme to prepare a sufficiently stable mixture of atoms in the three lowest hyperfine state of ^{6}Li. After some experimental efforts we succeeded in preparing a three-component mixture consisting of about 5×10^4 atoms per spin state in thermal equilibrium at a temperature of 250 nK corresponding to $T/T_F \approx 0.37$. This was accomplished by populating the third state close to the zero crossings of the Feshbach resonance resulting in a lifetime of about 30 s. The production scheme is discussed in detail in chapter 6.2. This ensemble is the starting point for further experiments.

In a first set of experiments we studied the collisional stability of the ensemble as a function of the applied homogeneous magnetic field between 0 and 600 G and thus as a function of the interaction between the constituents. In a first run of

the experiment we measured the remaining fraction of atoms in the trap after the ensemble was held at a certain magnetic field for a fixed time and discovered an enhanced loss of atoms at two magnetic field values (see figure 6.3). We showed that the observed loss does not occur when only two spin states are in the trap and concluded that a three-body effect involving atoms in all three spin states must be the reason for the enhanced loss. To obtain more quantitative information we measured the so-called three-body loss coefficient (for definition of K_3 see section 3.3) as a function of the magnetic field (see figure 6.6) in a series of lifetime measurements. As expected the loss coefficient was enhanced at two magnetic field values. We observed one pronounced resonance at 130 G and a relatively broad enhancement at 500 G. Similar results were obtained in the group of K.M. O'Hara at Pennsylvania State University [Huc09].

Soon, theoreticians were deeply interested and interpreted our results in terms of an Efimov-like trimer state that crosses the free atom continuum twice. E. Braaten and H.-W. Hammer, P. Naidon and M. Ueda and S. Flörchinger et al. were able to achieve nice agreement of the calculated three-body loss coefficient around the pronounced loss feature at 130 G, but their models failed to describe the broad enhancement of loss around 500 G. Instead, they predicted a second sharp loss resonance [Bra09b, Nai09, Flö09b] which caused some doubt about the validity of the universal description of the trimer state.

Yet, in section 6.5 it was shown that the observed three-body loss can be explained using universal theory when a varying lifetime of the trimer is taken into account. For the interpretation of our data, the model by Braaten and Hammer [Bra06], which was originally developed for three-body loss in a sample of identical bosons, was adapted to our case. Therefor the three scattering lengths a_{12}, a_{23} and a_{13} between the different components were combined to an effective interaction parameter a_m which takes the role of the scattering length in the Braaten-Hammer model. The universal description of the trimer state involves two additional parameters: The first one is the so called three-body parameter a_* that fixes the value of the scattering length where the trimer crosses the three atom continuum. The second one η_* is called elasticity parameter which is related to the lifetime of the trimer and determines the width of the observed loss resonance. The authors of [Bra09b, Nai09, Flö09b] assumed that η_* is constant over the whole magnetic field region.

It turned out that for a complete understanding of the observed behaviour of the three-body loss, a magnetic field dependence of the elasticity parameter η_* has to be taken into account [Wen09a]. In order to understand this, one has to know that the trimer decays into a deeply bound dimer and a free atom. Usually, the properties of these deeply bound dimers do not change over the region of interest and η_* can assumed to be constant. This is different in the case of ^{6}Li. In the considered magnetic field region below 500 G the trimer decays into the dimers

that are associated with the Feshbach resonances. The properties of these dimers change dramatically with the magnetic field. Their binding energy for example is a factor of about five smaller at 500 G than at 130 G. In section 6.5.3 it was shown that a simple ansatz in which η_* is assumed to be inversely proportional to the binding energy of these dimers, leads to a remarkable agreement between the observed three-body loss and the universal theory. This shows that the trimer itself can be described within a universal framework while its decay is determined by the non-universal dimer states that are associated with the Feshbach resonances.

Our next experiments on the three-component Fermi mixture will help to complete the understanding of Efimov physics in the ^{6}Li system in the high field regime above 600 G. E. Braaten and H.-W. Hammer calculated that the first excited trimer state merges the atom dimer-threshold of $|2\rangle - |3\rangle$ dimers and free atoms in state $|1\rangle$ around 670 G what should be observable in an enhancement of the atom-dimer relaxation rate [Bra09a]. In a first experiment evidence for this enhancement was already found, but a quantitative measurement of relaxation rates has still to be done. The mergence of the trimer with the atom-dimer threshold is also a promising parameter regime for the measurement of the binding energy of the trimer by radio frequency spectroscopy. The idea is the following: A sample consisting of $|2\rangle - |3\rangle$ dimers and free atoms in state $|2\rangle$ is prepared acting as the starting point of the experiment. Then a radio frequency field is applied whose frequency is detuned from the free-free transition between states $|2\rangle$ and $|1\rangle$. At a certain detuning that matches the binding energy of the trimer it should be possible to associate the trimer which is observable as an additional loss of atoms in state $|2\rangle$ at a frequency that is different from the free-free transition.

All experiments described so far are studying few-body physics. Knowledge of few-body physics in the system is essential for further studies of many-body phenomena. One experiment in that direction could probe the mean field-interaction between atoms and dimers. Let us imagine we have an imbalanced mixture of atoms in state $|2\rangle$ and $|3\rangle$, where atoms in state $|2\rangle$ form the majority component. When the temperature is lower than the critical temperature for condensation, a phase separated state is formed in which $|2\rangle - |3\rangle$ dimers form a superfluid core which is surrounded by free atoms in state $|2\rangle$. By applying a radio frequency pulse these free atoms can be transferred to state $|1\rangle$. In this configuration the atom-dimer scattering length determines the ongoing dynamics. If the scattering length is sufficiently large and positive the system should be stable in the separated phase. It turns out that the atom-dimer scattering length is determined by the trimer state, similar to a Feshbach resonance where a bound dimer state determines the scattering length of the free atoms. The preparation of such a separated state is the first step towards the preparation of a so called colour-superfluid where two of the components form a superfluid while the third one is a spectator.

In a colour-superfluid the superfluid and spectator components are not phase sep-

arated. Promising proposals for the preparation of such a colour-superfluid have been done for three-component Fermi mixtures in optical lattices [Rap08, Rap07, Mol09, Aza08]. Depending on the interaction strength between the particles the ground state of the system is either a colour superfluid or, for strong attractive interactions, a phase trions. These trions are bound states involving one atom of each of the components. Both states are connected via a quantum phase transition. Counterintuitively, strong three-body losses can be utilized to stabilize a colour-superconducting phase [Kan09]. This idea is based on a Quantum-Zeno like argument. Let us imagine two distinguishable fermions occupy the same lattice site while an atom in the third state occupies one of the neighbouring sites. There is some probability that this atom tunnels and all three atoms are then in the same site. These atoms might get lost from the system by three-body recombination. If the three-body recombination rate is much larger than the tunneling rate, the probability for the atom to tunnel is decreased substantially. In simple words, the probability amplitude of the third atom to be in the site of the other two atoms is probed with the three-body recombination rate. This probing can be understood as an ongoing measurement whether the atom did tunnel or not. As the tunneling rate is much smaller than the three-body recombination rate, the wavefunction of the atom is projected back onto its original site with a large probability. Thus, the tunneling probability is reduced and the stability of the system is increased. Inspired by such ideas we are currently constructing a new experimental setup in which an optical lattice will be implemented.

9.2 Towards a finite system of ultracold fermions

Progress was also made towards a finite fermionic ensemble with a controlled number of atoms. The most important tool in these experiments is the so called microtrap which is established by a tightly focused laser beam. Due to the high trapping frequencies and thus the large separation of energy states in this trap it should be possible to control the atom number by applying an external magnetic field gradient. Due to the magnetic moment of the atoms this gradient will serve as a linear potential that is superimposed on the trapping potential. Thus, the trapping potential is tilted and atoms are spilled from the trap (see figure 7.1).

To get started we chose an off-the-shelf aspheric lens for the generation of the microtrap and achieved a minimum beam waist of about 3 μm. After implementation of the lens into the setup, atoms were transferred into the microtrap and in a first experiment we applied a magnetic field gradient and recorded the remaining atom number by absorption imaging (see section 8.2). This experiment was repeated several times for a fixed magnetic field gradient and showed that we can prepare ensembles consisting of 120 ± 11 atoms so far. Since absorption imaging

was used for detecting the atoms this number may be affected by systematic errors for example due to saturation effects.

A much better choice for the detection of small atom numbers is the fluorescence imaging method. The number of atoms in the microtrap will be determined by recapturing them in the magneto optical trap and counting their fluorescence on a photodiode or a CCD camera. In order to be able to detect single atoms with this method, the amount of stray light falling onto the detector must be reduced as far as possible. To test whether this is possible in our current setup we modified our magneto-optical trap in way that it was able to capture only single atoms. To reduce the amount of stray light, the size of the trapping beams was reduced to about 7 mm in diameter. After some optimization of the MOT gradient and the detuning of the trapping beams it was possible to detect steps in the fluorescence light emitted by the atoms (see figure 8.5). This demonstrates that we are able to detect single atoms by applying the fluorescence imaging technique.

For the preparation of atomic number states in the tilted microtrap potential it is necessary that the tunneling rates of bound states in the trap are substantially different. While the lifetime of the highest excited state should be sufficiently small, the lifetime of the next lower state must be long compared to the timescale of the experiment. Only if this condition is fulfilled the desired atom number can be prepared with high fidelity. The tunneling rates for typical parameters of our microtrap have been estimated using the one-dimensional WKB approximation. Although the waist of the microtrap is still relatively large, the results seem quite promising (see figure 7.4) and suggest that the control of the atom number on the single particle level is feasible with our current setup. As soon as possible the microtrap will be combined with the fluorescence imaging technique and experiments will show how far we can get with the current setup. To improve the microtrap setup a custom made objective is currently under construction that will be able to generate a focus with a waist on the order of one micrometer. According to the WKB approximation, the preparation of a desired atomic number state should be possible in such a trap with high fidelity.

Once we are able to prepare number states on demand, the system will serve as a clean model system for few fermion systems as for example atomic nuclei. The key feature of our system will be that the interaction between the particles is tunable by means of the Feshbach resonance. In a first experiment it will be studied how the number of particles that fit into the trap scales as a function of the interaction. For diverging scattering length this will be a measure of the universal β factor (see 2.4) in a finite system. It is not a priori clear whether the bulk value is also applicable in a system with small particle number. Another phenomenon that can be studied is pairing between the particles as a function of the atom number and the interparticle interaction. The gap in the excitation spectrum can be measured by performing radio-frequency spectroscopy. As the gap is a function of the

particle number it should be possible to do spectroscopy on a single particle level.

Appendix A

Fundamental constants

Symbol	Value	Meaning
$\hbar$	$1.054571628\times10^{-34}\,\mathrm{Js}$	Planck's constant over 2π
h	$6.62606896\times10^{-34}\,\mathrm{Js}$	Planck's constant
c	$2.99792458\times10^{8}\,\mathrm{m/s}$	Speed of light in vacuum
k_B	$1.3806504\times10^{-23}\,\mathrm{JK^{-1}}$	Boltzmann's constant
a_0	$0.52917720859\times10^{-10}\,\mathrm{m}$	Bohr's radius
ϵ_0	$8.854187817\times10^{-12}\,\mathrm{Fm^{-1}}$	Electric constant
μ_B	$927.400915\times10^{-26}\,\mathrm{J/T}$	Bohr's magneton
m_e	$9.10938215\times10^{-31}\,\mathrm{kg}$	Mass of a electron
m_{Li}	$9.98834146\times10^{-27}\,\mathrm{kg}$	Mass of a $^6\mathrm{Li}$ atom
γ_{Li}	$5.872\times10^{6}\,\mathrm{Hz}$	Natural linewidth of the D_2 line of $^6\mathrm{Li}$
λ_{Li}	$670.977338\times10^{-9}\,\mathrm{m}$	Wavelength of the D_2 line of $^6\mathrm{Li}$ in vacuum

Table A.1: Fundamental constants are taken from [NIS], the properties of $^6\mathrm{Li}$ can be found in [Geh].

Appendix B

Level scheme of ^{6}Li

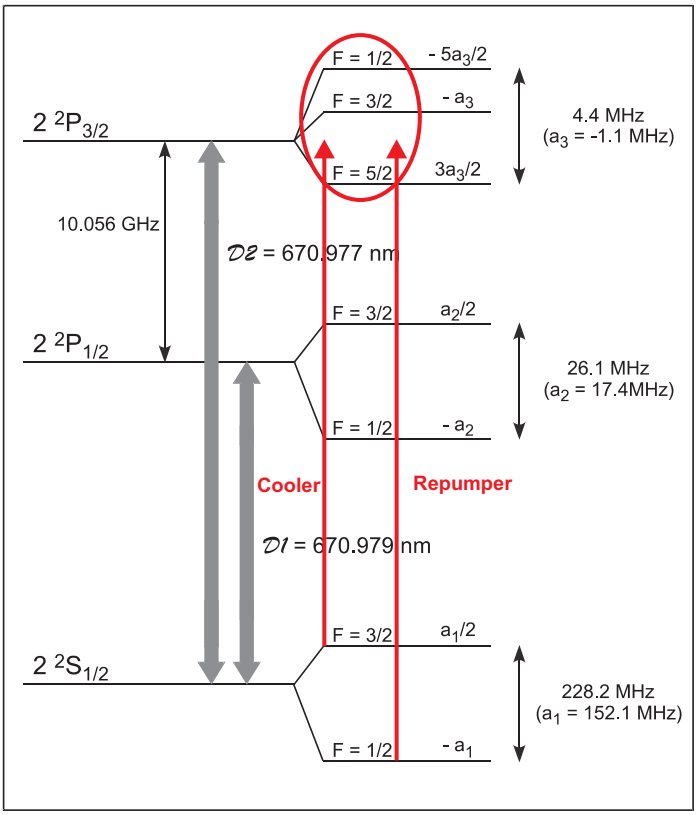

Figure B.1: Level scheme of ^{6}Li taken from [Geh]. Arrows indicate the transitions used as cooler and repumper in the magneto-optical trap. While the hyperfine spiltting of the ground state of 228 MHz is experimentally important, the splitting in the $2P_{3/2}$ excited state is on the order of the natural linewidth of 5.9 MHz and can not be resolved.

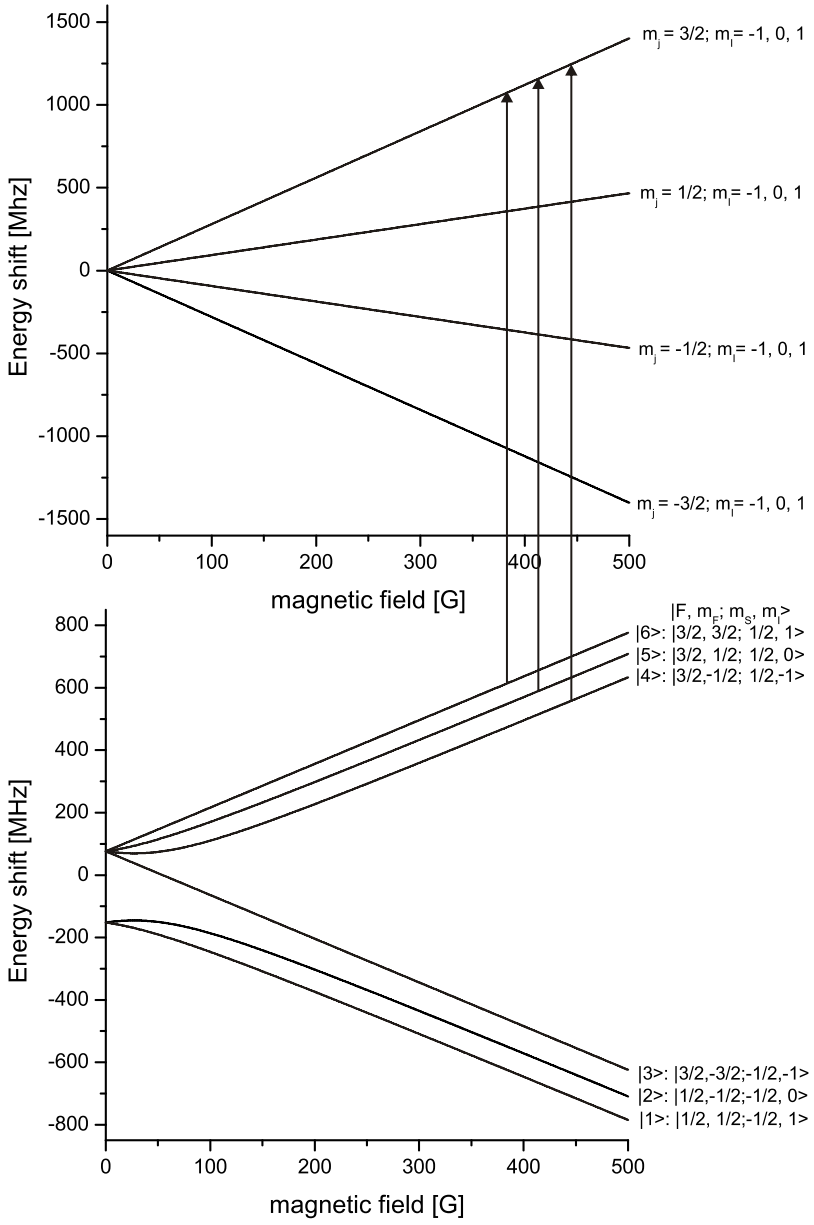

Figure B.2: Zeeman hyperfine levels of the ^{6}Li electronic ground and the $2P_{3/2}$ excited state. The arrows indicate the transitions used in the Zeeman slower. For large magnetic fields nuclear and electron spin decouple and optical transitions become closed due to selection rules for electric dipole transitions.

List of Figures

Bibliography

[And95] M. H. Anderson, J. R. Ensher, M. R. Matthews, C. E. Wieman, E. A. Cornell, *Observation of Bose-Einstein condensation in a Dilute Atomic Vapor*, Science **269**, 198–201 (Jul 1995).

[Ast04] G. E. Astrakharchik, J. Boronat, J. Casulleras, Giorgini, S., *Equation of State of a Fermi Gas in the BEC-BCS Crossover: A Quantum Monte Carlo Study*, Phys. Rev. Lett. **93**(20), 200404 (Nov 2004).

[Aza08] P. Azaria, S. Capponi, P. Lecheminant, *Three-Component Fermi Gas in a one-dimensional Optical Lattice*, arXiv.org:0811.0555 (2008).

[Bar57] J. Bardeen, L. N. Cooper, J. R. Schrieffer, *Microscopic Theory of Superconductivity*, Phys. Rev. **106**(1), 162–164 (Apr 1957).

[Bar04] M. Bartenstein, A. Altmeyer, S. Riedl, S. Jochim, C. Chin, J. Hecker Denschlag, R. Grimm, *Crossover from a molecular Bose-Einstein condensate to a Degenerate Fermi Gas*, Phys. Rev. Lett. **92**(12), 120401 (Mar 2004).

[Bar05] M. Bartenstein, A. Altmeyer, S. Riedl, R. Geursen, S. Jochim, C. Chin, J. H. Denschlag, R. Grimm, A. Simoni, E. Tiesinga, C. J. Williams, P. S. Julienne, *Precise Determination of ^{6}Li Cold Collision Parameters by Radio-Frequency Spectroscopy on Weakly Bound Molecules*, Phys. Rev. Lett. **94**(10), 103201 (2005).

[Bar09] G. Barontini, C. Weber, F. Rabatti, J. Catani, G. Thalhammer, M. Inguscio, F. Minardi, *Observation of Heteronuclear Atomic Efimov Resonances*, Physical Review Letters **103**(4), 043201 (2009).

[Bed00] P. F. Bedaque, E. Braaten, H.-W. Hammer, *Three-body Recombination in Bose Gases with Large Scattering Length*, Phys. Rev. Lett. **85**(5), 908–911 (Jul 2000).

[Bed09] P. F. Bedaque, J. P. Jose P. D'Incao, *Superfluid phases of the three-species fermion gas*, Annals of Physics **324**(8), 1763 – 1768 (2009).

[Blu08] D. Blume, S. T. Rittenhouse, J. von Stecher, C. H. Greene, *Stability of inhomogeneous multicomponent Fermi gases*, Phys. Rev. A **77**(3), 033627 (2008).

[Bos] S. N. Bose, *Plancks Gesetz und Lichtquantenhypothese.*, *Z. Phys.*, 26:178, 1924.

[Bou04] T. Bourdel, L. Khaykovich, J. Cubizolles, J. Zhang, F. Chevy, M. Teichmann, L. Tarruell, S. J. J. M. F. Kokkelmans, C. Salomon, *Experimental Study of the BEC-BCS Crossover Region in Lithium 6*, Phys. Rev. Lett. **93**(5), 050401 (2004).

[Bra95] C. C. Bradley, C. A. Sackett, J. J. Tollett, R. G. Hulet, *Evidence of Bose-Einstein Condensation in an Atomic Gas with Attractive Interactions*, Phys. Rev. Lett. **75**(9), 1687–1690 (Aug 1995).

[Bra01] E. Braaten, H.-W. Hammer, *Three-Body Recombination into Deep Bound States in a Bose Gas with Large Scattering Length*, Phys. Rev. Lett. **87**(16), 160407 (Oct 2001).

[Bra03] E. Braaten, H.-W. Hammer, *Universality in the three-body problem for ^{4}He atoms*, Phys. Rev. A **67**(4), 042706 (Apr 2003).

[Bra04] E. Braaten, H.-W. Hammer, *Enhanced dimer relaxation in an atomic and molecular Bose-Einstein condensate*, Phys. Rev. A **70**(4), 042706 (Oct 2004).

[Bra06] E. Braaten, H. W. Hammer, *Universality in Few-body Systems with Large Scattering Length*, Physics Reports **428**, 259 (2006).

[Bra09a] E. Braaten, H. W. Hammer, D. Kang, L. Platter, *Efimov Physics in ^{6}Li Atoms*, arXiv.org:0908.4046 (2009).

[Bra09b] E. Braaten, H.-W. Hammer, D. Kang, L. Platter, *Three-Body Recombination of ^{6}Li Atoms with Large Negative Scattering Lengths*, Physical Review Letters **103**(7), 073202 (2009).

[Bri05] D. M. Brink, R. A. Broglia, *Nuclear Superfluidity - Pairing in finite systems* (Cambridge University Press, 2005).

[Bru02] G. M. Bruun, H. Heiselberg, *Cooper pairing and single-particle properties of trapped Fermi gases*, Phys. Rev. A **65**(5), 053407 (Apr 2002).

[Bul06] A. Bulgac, J. E. Drut, P. Magierski, *Spin 1/2 Fermions in the Unitary Regime: A Superfluid of a New Type*, Physical Review Letters **96**(9), 090404 (2006).

[Bur97] E. A. Burt, R. W. Ghrist, C. J. Myatt, M. J. Holland, E. A. Cornell, C. E. Wieman, *Coherence, Correlations, and Collisions: What One Learns about Bose-Einstein Condensates from Their Decay*, Phys. Rev. Lett. **79**(3), 337–340 (Jul 1997).

[Cam06] G. K. Campbell, J. Mun, M. Boyd, P. Medley, A. E. Leanhardt, L. G. Marcassa, D. E. Pritchard, W. Ketterle, *Imaging the Mott Insulator Shells by Using Atomic Clock Shifts*, Science **313**(5787), 649–652 (2006).

[Car03] J. Carlson, S.-Y. Chang, V. R. Pandharipande, K. E. Schmidt, *Superfluid Fermi Gases with Large Scattering Length*, Phys. Rev. Lett. **91**(5), 050401 (Jul 2003).

[Car08] J. Carlson, S. Reddy, *Superfluid Pairing Gap in Strong Coupling*, Physical Review Letters **100**(15), 150403 (2008).

[Cha04] S. Y. Chang, V. R. Pandharipande, J. Carlson, K. E. Schmidt, *Quantum Monte Carlo studies of superfluid Fermi gases*, Phys. Rev. A **70**(4), 043602 (Oct 2004).

[Che07] R. W. Cherng, G. Refael, E. Demler, *Superfluidity and Magnetism in Multicomponent Ultracold Fermions*, Phys. Rev. Lett. **99**(13), 130406 (2007).

[Chi04a] C. Chin, M. Bartenstein, A. Altmeyer, S. Riedl, S. Jochim, J. Hecker Denschlag, R. Grimm, *Observation of the Pairing Gap in a Strongly Interacting Fermi Gas*, Science **305**(5687), 1128–1130 (2004).

[Chi04b] C. Chin, R. Grimm, *Thermal equilibrium and efficient evaporation of an ultracold atom-molecule mixture*, Phys. Rev. A **69**(3), 033612 (Mar 2004).

[Chi09] C. Chin, R. Grimm, P. Julienne, E. Tiesinga, *Feshbach resonances in ultracold gases*, arxiv.org:0812.1496v2 (2009).

[Chu05] C.-S. Chuu, F. Schreck, T. P. Meyrath, J. L. Hanssen, G. N. Price, M. G. Raizen, *Direct Observation of Sub-Poissonian Number Statistics in a Degenerate Bose Gas*, Phys. Rev. Lett. **95**(26), 260403 (Dec 2005).

[Cub03] J. Cubizolles, T. Bourdel, S. J. J. M. F. Kokkelmans, G. V. Shlyapnikov, C. Salomon, *Production of Long-Lived Ultracold Li_2 Molecules from a Fermi Gas*, Phys. Rev. Lett. **91**(24), 240401 (Dec 2003).

[Dal99] F. Dalfovo, S. Giorgini, L. P. Pitaevskii, S. Stringari, *Theory of Bose-Einstein condensation in trapped gases*, Rev. Mod. Phys. **71**(3), 463–512 (Apr 1999).

[Dav95] K. B. Davis, M. O. Mewes, M. R. Andrews, N. J. van Druten, D. S. Durfee, D. M. Kurn, W. Ketterle, *Bose-Einstein condensation in a gas of sodium atoms*, Phys. Rev. Lett. **75**(22), 3969–3973 (Nov 1995).

[Del60] L. M. Delves, *Tertiary and general-order collisions (II)*, Nuclear Physics **20**, 275 – 308 (1960).

[DeM99a] B. DeMarco, J. L. Bohn, J. P. Burke, M. Holland, D. S. Jin, *Measurement of p-Wave Threshold Law Using Evaporatively Cooled Fermionic Atoms*, Phys. Rev. Lett. **82**(21), 4208–4211 (May 1999).

[DeM99b] B. DeMarco, D. S. Jin, *Onset of Fermi degeneracy in a trapped atomic gas*, Science **285**(5434), 1703–1706 (1999).

[D'I04] J. P. D'Incao, H. Suno, B. D. Esry, *Limits on Universality in Ultracold Three-Boson Recombination*, Phys. Rev. Lett. **93**(12), 123201 (Sep 2004).

[D'I09] J. P. D'Incao, B. D. Esry, *Ultracold three-body collisions near overlapping Feshbach resonances*, arXiv.org:0905.0772 (2009).

[Dud07] A. M. Dudarev, M. G. Raizen, Q. Niu, *Quantum Many-Body Culling: Production of a Definite Number of Ground-State Atoms in a Bose-Einstein Condensate*, Physical Review Letters **98**(6), 063001 (2007).

[Efi70] V. Efimov, *Energy levels arising from resonant two-body forces in a three-body system*, Physics Letters B **33**(8), 563 – 564 (1970).

[Efi71] V. Efimov, *Weakly-bound states of three resonantly-interacting particles* (1971), originally: Yad. Fiz. **12**, 1080-1091 (1970).

[Efi79] V. Efimov, *Low-energy properties of three resonantly interacting*, Sov. J. Nucl. Phys. **29**, 546–553 (1979), originally: Yad. Fiz. **29**, 1058-1069 (1979).

[Ein] A. Einstein, *Quantentheorie des einatomigen idealen Gases. Zweite Abhandlung.*, *Sitzungsberichte der Preussischen Akademie der Wissenschaften*, 1:3, 1925.

[Err09] B. Errea, J. Dukelsky, G. Ortiz, *Breached pairing in trapped three-color atomic Fermi gases*, Physical Review A (Atomic, Molecular, and Optical Physics) **79**(5), 051603 (2009).

[Esr99] B. D. Esry, C. H. Greene, J. P. Burke, *Recombination of Three Atoms in the Ultracold Limit*, Phys. Rev. Lett. **83**(9), 1751–1754 (Aug 1999).

[Fed93] D. V. Fedorov, A. S. Jensen, *Efimov effect in coordinate space Faddeev equations*, Phys. Rev. Lett. **71**(25), 4103–4106 (Dec 1993).

[Fer09] F. Ferlaino, S. Knoop, M. Berninger, W. Harm, J. P. D'Incao, H.-C. Nägerl, R. Grimm, *Evidence for Universal Four-Body States Tied to an Efimov Trimer*, Physical Review Letters **102**(14), 140401 (2009).

[Fes58] H. Feshbach, *A Unified Theory of Nuclear Reactions*, Ann. Phys. **5**(337) (1958).

[Flö09a] S. Flörchinger, R. Schmidt, S. Moroz, C. Wetterich, *Functional renormalization for trion formation in ultracold fermion gases*, Physical Review A (Atomic, Molecular, and Optical Physics) **79**(1), 013603 (2009).

[Flö09b] S. Flörchinger, R. Schmidt, C. Wetterich, *Three-body loss in lithium from functional renormalization*, Physical Review A (Atomic, Molecular, and Optical Physics) **79**(5), 053633 (2009).

[Foe06] S. Foelling, A. Widera, T. Müller, F. Gerbier, I. Bloch, *Formation of Spatial Shell Structure in the Superfluid to Mott Insulator Transition*, Physical Review Letters **97**(6), 060403 (2006).

[Geh] M. E. Gehm, *Properties of* $^6\mathrm{Lithium}$*, 2003: http://www.phy.duke.edu/research/photon/qoptics/techdocs/pdf/PropertiesOfLi.pdf*.

[Ger06] F. Gerbier, S. Fölling, A. Widera, O. Mandel, I. Bloch, *Probing Number Squeezing of Ultracold Atoms across the Superfluid-Mott Insulator Transition*, Physical Review Letters **96**(9), 090401 (2006).

[Gra02] S. R. Granade, M. E. Gehm, K. M. O'Hara, J. E. Thomas, *All-Optical Production of a Degenerate Fermi Gas*, Phys. Rev. Lett. **88**(12), 120405 (Mar 2002).

[Gre03] M. Greiner, C. A. Regal, D. S. Jin, *Emergence of a molecular Bose-Einstein condensate from a Fermi gas*, Nature **426**, 537–540 (2003).

[Gri00] R. Grimm, M. Weidemüller, Y. B. Ovchinnikov, *Optical dipole traps for neutral atoms*, Advances in Atomic, Molecular and Optical Physics **42**, 95 (2000).

[Gro61] E. Gross, *Structure of a Quantized Vortex in Boson Systems*, Nuovo Cimento **20**, 454 (1961).

[Gro63] E. Gross, *Hydrodynamics of a Superfluid Condensate*, Journal of Mathematical Physics **4**, 199 (1963).

[Gro09] N. Gross, Z. Shotan, S. Kokkelmans, L. Khaykovich, *Observation of universality in ultracold ^{7}Li three-body recombination*, arXiv.org:0906.4731 (2009).

[Gup03] S. Gupta, Z. Hadzibabic, M. W. Zwierlein, C. A. Stan, K. Dieckmann, C. H. Schunck, E. G. M. van Kempen, B. J. Verhaar, W. Ketterle, *Radio-Frequency Spectroscopy of Ultracold Fermions*, Science **300**(5626), 1723–1726 (2003).

[Had02] Z. Hadzibabic, C. A. Stan, K. Dieckmann, S. Gupta, M. W. Zwierlein, A. Görlitz, W. Ketterle, *Two-Species Mixture of Quantum Degenerate Bose and Fermi Gases*, Phys. Rev. Lett. **88**(16), 160401 (Apr 2002).

[Hei01] H. Heiselberg, *Fermi systems with long scattering lengths*, Phys. Rev. A **63**(4), 043606 (Mar 2001).

[Hei03] H. Heiselberg, *Pairing of fermions in atomic traps and nuclei*, Phys. Rev. A **68**(5), 053616 (Nov 2003).

[Hon04] C. Honerkamp, W. Hofstetter, *BCS pairing in Fermi systems with N different hyperfine states*, Phys. Rev. B **70**(9), 094521 (Sep 2004).

[Hou98] M. Houbiers, H. T. C. Stoof, W. I. McAlexander, R. G. Hulet, *Elastic and inelastic collisions of ^{6}Li atoms in magnetic and optical traps*, Phys. Rev. A **57**(3), R1497–R1500 (Mar 1998).

[Huc09] J. H. Huckans, J. R. Williams, E. L. Hazlett, R. W. Stites, K. M. O'Hara, *Three-Body Recombination in a Three-State Fermi Gas with Widely Tunable Interactions*, Phys. Rev. Lett. **102**(16), 165302 (Apr 2009).

[Joc03a] S. Jochim, M. Bartenstein, A. Altmeyer, G. Hendl, C. Chin, J. Hecker Denschlag, R. Grimm, *Pure Gas of Optically Trapped Molecules Created from Fermionic Atoms*, Phys. Rev. Lett. **91**(24), 240402 (Dec 2003).

[Joc03b] S. Jochim, M. Bartenstein, A. Altmeyer, G. Hendl, S. Riedl, C. Chin, J. Hecker Denschlag, R. Grimm, *Bose-Einstein condensation of molecules*, Science **302**(5653), 2101–2103 (2003).

[Joc09] S. Jochim, *Ultracold Fermi gases: Properties and techniques* (2009), in: M. Weidemüller, C. Zimmermann (Eds.), Cold Atoms and Molecules, 2nd edition.

[Jul] P. Julienne, *Private Communications, Calculations done according to [Bar05].*

[Jul92] P. Julienne, A. Smith, K. Burnett, *Theory of Collisions between Laser Cooled Atoms*, Vol. 30 of *Advances In Atomic, Molecular, and Optical Physics*, 141 – 198 (Academic Press, 1992).

[Kan09] A. Kantian, M. Dalmonte, S. Diehl, W. Hofstetter, P. Zoller, A. J. Daley, *An atomic colour superfluid via three-body loss*, arXiv.org:0908.3235 (2009).

[Ket99] W. Ketterle, D. S. Durfee, D. M. Stamper-Kurn, *Making, probing and understanding Bose-Einstein condensates*, in: M. Inguscio, S.Stringari and C.Wiemann (Eds.); Bose-Einstein Condensation in Atomic Gases, IOS Press (1999).

[Ket08] W. Ketterle, M. W. Zwierlein, *Making, probing and understanding ultracold Fermi gases*, in: M. Inguscio, W.Ketterle, and C. Salomon (Eds.); Ultracold Fermi Gases, Proceedings of the International School of Physics - Enrico Fermi **Course CLXIV**, IOS Press (2008).

[Kno09] S. Knoop, F. Ferlaino, M. Mark, M. Berninger, H. Schoebel, H.-C. Naegerl, R. Grimm, *Observation of an Efimov-like trimer resonance in ultracold atom-dimer scattering*, Nature Physics **5**, 227–230 (2009).

[Koh08] M. Kohnen, *Ultracold Fermi Mixtures in an Optical Dipole Trap*, Diploma thesis (2008).

[Kra06] T. Kraemer, M. Mark, P. Waldburger, J. G. Danzl, B. Chin, C.and Engeser, A. D. Lange, K. Pilch, A. Jaakkola, H.-C. Naegerl, R. Grimm, *Evidence for Efimov quantum states in an ultracold gas of caesium atoms*, Nature **440**, 315–318 (2006).

[Lan81] L. D. Landau, L. M. Lifshitz, *Quantum Mechanics* (Butterworth Heinemann, 1981), 3rd Edn.

[Lim77] T. K. Lim, S. K. Duffy, W. C. Damer, *Efimov State in the ^{4}He Trimer*, Phys. Rev. Lett. **38**(7), 341–343 (Feb 1977).

[Lom08] T. Lompe, *An appartus for the production of molecular Bose-Einstein condensates*, Diploma thesis (2008).

[Luo06] L. Luo, B. Clancy, J. Joseph, J. Kinast, A. Turlapov, J. Thomas, *Evaporative cooling of unitary Fermi gas mixtures in optical traps*, New Journal of Physics **8**(9), 213 (2006).

[Luo09] L. Luo, J. E. Thomas, *Thermodynamic Measurements in a Strongly Interacting Fermi Gas*, Journal of Low Temperature Physics **154**, 1–29 (2009).

[Mer98] E. Merzbacher, *Quantum Mechanics* (John Wiley and Sons, Inc., 1998), 3rd Edn.

[Met99] H. J. Metcalf, P. van der Straten, *Laser Cooling and Trapping* (Springer-Verlag, New York, 1999).

[Mig59] A. Migdal, *Superfluidity and the moments of inertia of nuclei*, Nuclear Physics **13**, 655–674 (1959).

[Mig67] A. B. Migdal, *Theory of finite Fermi systems and applications to atomic nuclei* (Interscience Publishers, 1967).

[Moe95] A. J. Moerdijk, B. J. Verhaar, A. Axelsson, *Resonances in ultracold collisions of ^{6}Li, ^{7}Li, and ^{23}Na*, Phys. Rev. A **51**(6), 4852–4861 (Jun 1995).

[Mol09] R. A. Molina, J. Dukelsky, P. Schmitteckert, *Crystallization of trions in SU(3) cold-atom gases trapped in optical lattices*, Physical Review A (Atomic, Molecular, and Optical Physics) **80**(1), 013616 (2009).

[Nai09] P. Naidon, M. Ueda, *Possible Efimov Trimer State in a Three-Hyperfine-Component Lithium-6 Mixture*, Physical Review Letters **103**(7), 073203 (2009).

[Nie99] E. Nielsen, J. H. Macek, *Low-Energy Recombination of Identical Bosons by Three-Body Collisions*, Phys. Rev. Lett. **83**(8), 1566–1569 (Aug 1999).

[Nie01] E. Nielsen, D. V. Fedorov, A. S. Jensen, E. Garrido, *The three-body problem with short-range interactions*, Physics Reports **347**(5), 373 – 459 (2001).

[NIS] NIST, *http://physics.nist.gov/cuu/Constants/*.

[Nis09] Y. Nishida, S. Tan, *Confinement-induced Efimov resonances in Fermi-Fermi mixtures*, Physical Review A (Atomic, Molecular, and Optical Physics) **79**(6), 060701 (2009).

[O'H01] K. M. O'Hara, M. E. Gehm, S. R. Granade, J. E. Thomas, *Scaling laws for evaporative cooling in time-dependent optical traps*, Phys. Rev. A **64**(5), 051403 (Oct 2001).

[O'H02a] K. M. O'Hara, S. L. Hemmer, M. E. Gehm, S. R. Granade, J. E. Thomas, *Observation of a Strongly Interacting Degenerate Fermi Gas of Atoms*, Science **298**(5601), 2179–2182 (2002).

[O'H02b] K. M. O'Hara, S. L. Hemmer, M. E. Gehm, S. R. Granade, J. E. Thomas, *Observation of a Strongly Interacting Degenerate Fermi Gas of Atoms*, Science **298**(5601), 2179–2182 (2002).

[Orz01] C. Orzel, A. K. Tuchman, M. L. Fenselau, M. Yasuda, M. A. Kasevich, *Squeezed States in a Bose-Einstein Condensate*, Science **291**(5512), 2386–2389 (2001).

[Ott08] T. B. Ottenstein, T. Lompe, M. Kohnen, A. N. Wenz, S. Jochim, *Collisional Stability of a Three-Component Degenerate Fermi Gas*, Phys. Rev. Lett. **101**(20), 203202 (2008).

[Paa06] T. Paananen, J.-P. Martikainen, P. Törmä, *Pairing in a three-component Fermi gas*, Phys. Rev. A **73**(5), 053606 (2006).

[Paa07] T. Paananen, P. Törmä, J.-P. Martikainen, *Coexistence and shell structures of several superfluids in trapped three-component Fermi mixtures*, Phys. Rev. A **75**(2), 023622 (2007).

[Par06] G. B. Partridge, W. Li, Y. A. Liao, R. G. Hulet, M. Haque, H. T. C. Stoof, *Deformation of a Trapped Fermi Gas with Unequal Spin Populations*, Phys. Rev. Lett. **97**(19), 190407 (2006).

[Pet02] C. J. Pethick, H. Smith, *Bose-Einstein-Condensation in Dilute Gases* (Cambridge University Press, 2002).

[Pet03] D. S. Petrov, *Three-body problem in Fermi gases with short-range interparticle interaction*, Phys. Rev. A **67**(1), 010703 (Jan 2003).

[Pet04] D. S. Petrov, C. Salomon, G. V. Shlyapnikov, *Weakly Bound Dimers of Fermionic Atoms*, Phys. Rev. Lett. **93**(9), 090404 (Aug 2004).

[Pet05] D. S. Petrov, C. Salomon, G. V. Shlyapnikov, *Scattering properties of weakly bound dimers of fermionic atoms*, Phys. Rev. A **71**(1), 012708 (2005).

[Pin97] P. W. H. Pinkse, A. Mosk, M. Weidemüller, M. W. Reynolds, T. W. Hijmans, J. T. M. Walraven, *Adiabatically Changing the Phase-Space Density of a Trapped Bose Gas*, Phys. Rev. Lett. **78**(6), 990–993 (Feb 1997).

[Pit61] L. Pitaevskii, *Vortex Lines in an Imperfect Bose Gas*, Sov. Phys. JETP **13**, 451 (1961).

[Pit03] L. Pitaevskii, S. Stringari, *Bose-Einstein Condensation* (Oxford Science Publications, 2003).

[Pon09] M. Pons, A. del Campo, J. G. Muga, M. G. Raizen, *Preparation of atomic Fock states by trap reduction*, Physical Review A (Atomic, Molecular, and Optical Physics) **79**(3), 033629 (2009).

[Rai09] M. G. Raizen, S.-P. Wan, C. Zhang, Q. Niu, *Ultra-high fidelity qubits for quantum computing*, arXiv.org:0906.2114 (2009).

[Rap07] A. Rapp, G. Zarand, C. Honerkamp, W. Hofstetter, *Color Superfluidity and "Baryon" Formation in Ultracold Fermions*, Physical Review Letters **98**(16), 160405 (2007).

[Rap08] A. Rapp, W. Hofstetter, G. Zaránd, *Trionic phase of ultracold fermions in an optical lattice: A variational study*, Phys. Rev. B **77**(14), 144520 (2008).

[Reg03] C. A. Regal, C. Ticknor, J. L. Bohn, D. S. Jin, *Creation of ultracold molecules from a Fermi gas of atoms*, Nature **424**(6944), 47–50 (2003).

[Reg04a] C. A. Regal, M. Greiner, D. S. Jin, *Lifetime of Molecule-Atom Mixtures near a Feshbach Resonance in ^{40}K*, Phys. Rev. Lett. **92**(8), 083201 (Feb 2004).

[Reg04b] C. A. Regal, M. Greiner, D. S. Jin, *Observation of Resonance Condensation of Fermionic Atom Pairs*, Phys. Rev. Lett. **92**(4), 040403 (Jan 2004).

[Reg05] C. A. Regal, *Experimental realization of BCS-BEC crossover physics with a Fermi gas of atoms*, Ph.D. thesis, University of Colorado, Boulder (2005).

[Roa02] G. Roati, F. Riboli, G. Modugno, M. Inguscio, *Fermi-Bose Quantum Degenerate ^{40}K-^{87}Rb Mixture with Attractive Interaction*, Phys. Rev. Lett. **89**(15), 150403 (Sep 2002).

[Sal91] B. E. A. Saleh, M. C. Teich, *Fundamentals of Photonics* (John Wiley and Sons, Inc., 1991).

[Sch96] W. Schöllkopf, J. P. Tönnies, *The nondestructive detection of the helium dimer and trimer*, The Journal of Chemical Physics **104**(3), 1155–1158 (1996).

[Sch99] U. Schünemann, H. Engler, R. Grimm, M. Weidemüller, M. Zielonkowski, *Simple scheme for tunable frequency offset locking of two lasers*, Review of Scientific Instruments **70**(1), 242–243 (1999).

[Sch01] F. Schreck, L. Khaykovich, K. L. Corwin, G. Ferrari, T. Bourdel, J. Cubizolles, C. Salomon, *Quasipure Bose-Einstein Condensate Immersed in a Fermi Sea*, Phys. Rev. Lett. **87**(8), 080403 (Aug 2001).

[Sch08] C. H. Schunck, Y.-i. Shin, A. Schirotzek, W. Ketterle, *Determination of the fermion pair size in a resonantly interacting superfluid*, Nature **454**, 739–743 (2008).

[Ser07] F. Serwane, *The setup of a Magneto Optical Trap for the preparation of a mesoscopic degenerate Fermi gas*, Diploma thesis (2007).

[Shi06] Y. Shin, M. W. Zwierlein, C. H. Schunck, A. Schirotzek, W. Ketterle, *Observation of Phase Separation in a Strongly Interacting Imbalanced Fermi Gas*, Phys. Rev. Lett. **97**(3), 030401 (2006).

[Shi08a] Y. il Shin, *Determination of the equation of state of a polarized Fermi gas at unitarity*, Physical Review A (Atomic, Molecular, and Optical Physics) **77**(4), 041603 (2008).

[Shi08b] Y. il Shin, C. H. Schunck, A. Schirotzek, W. Ketterle, *Phase diagram of a two-component Fermi gas with resonant interactions*, Nature **451**, 689–693 (Feb 2008).

[Sil09] T. N. D. Silva, *Three-component fermion pairing in two dimensions*, Physical Review A (Atomic, Molecular, and Optical Physics) **80**(1), 013620 (2009).

[SK98] D. M. Stamper-Kurn, H.-J. Miesner, A. P. Chikkatur, S. Inouye, J. Stenger, W. Ketterle, *Reversible Formation of a Bose-Einstein Condensate*, Phys. Rev. Lett. **81**(11), 2194–2197 (sept 1998).

[Ste09] J. von Stecher, J. D'Incao, C. H. Greene, *Signatures of universal four-body phenomena and their relation to the Efimov effect*, Nature Physics **5**, 417–421 (2009).

[Str03] K. E. Strecker, G. B. Partridge, R. G. Hulet, *Conversion of an Atomic Fermi Gas to a Long-Lived Molecular Bose Gas*, Phys. Rev. Lett. **91**(8), 080406 (Aug 2003).

[Stü32] E. C. G. Stückelberg, *Theorie der unelastischen Stoesse zwischen Atomen*, Helv. Phys. Acta **5**(369) (1932).

[Tru01] A. G. Truscott, K. E. Strecker, W. I. McAlexander, G. B. Partridge, R. G. Hulet, *Observation of Fermi Pressure in a Gas of Trapped Atoms*, Science **291**(5513), 2570–2572 (2001).

[Web03a] T. Weber, *Bose-Einstein Condensation of Optically Trapped Cesium*, Dissertation, Universität Innsbruck (2003).

[Web03b] T. Weber, J. Herbig, M. Mark, H.-C. Nägerl, R. Grimm, *Three-Body Recombination at Large Scattering Lengths in an Ultracold Atomic Gas*, Phys. Rev. Lett. **91**(12), 123201 (Sep 2003).

[Wen09a] A. Wenz, T. Lompe, T. Ottenstein, F. Serwane, G. Zürn, S. Jochim, *Universal trimer in a three-component Fermi gas*, Physical Review A (Atomic, Molecular, and Optical Physics) **80**(4), 040702 (2009).

[Wen09b] A. N. Wenz, *Few-Body Physics in a Three-Component Fermi Gas*, Diploma thesis (2009).

[Wil07] F. Wilczek, *Quantum chromodynamics: Lifestyles of the small and simple*, Nature Physics **3**, 375–376 (2007).

[Wil09] J. R. Williams, E. L. Hazlett, J. H. Huckans, R. W. Stites, Y. Zhang, K. M. O'Hara, *Evidence for an Excited-State Efimov Trimer in a Three-Component Fermi Gas*, Physical Review Letters **103**(13), 130404 (2009).

[Zac09] M. Zaccanti, B. Deissler, C. D'Errico, M. Fattori, M. Jona-Lasinio, S. Mueller, G. Roati, M. Inguscio, G. Modugno, *Observation of an Efimov spectrum in an atomic system*, Nature Physics **5**, 586–591 (2009).

[Zha07] H. Zhai, *Superfluidity in three-species mixtures of Fermi gases across Feshbach resonances*, Phys. Rev. A **75**(3), 031603 (2007).

[Zin09] N. T. Zinner, K. Mølmer, C. Ozen, D. J. Dean, K. Langanke, *Shell-model Monte Carlo simulations of the BCS-BEC crossover in few-fermion systems*, Physical Review A (Atomic, Molecular, and Optical Physics) **80**(1), 013613 (2009).

[Zue09] G. Zuern, *Realization of an optical microtrap for the production of a finite Fermi gas*, Diploma thesis (2009).

[Zwi03] M. W. Zwierlein, C. A. Stan, C. H. Schunck, S. M. F. Raupach, S. Gupta, Z. Hadzibabic, W. Ketterle, *Observation of Bose-Einstein Condensation of Molecules*, Phys. Rev. Lett. **91**(25), 250401 (Dec 2003).

[Zwi05] M. W. Zwierlein, J. R. Abo-Shaeer, A. Schirotzek, C. H. Schunck, W. Ketterle, *Vortices and superfluidity in a strongly interacting Fermi gas*, Nature **435**, 1047–1051 (2005).

Danksagung

An dieser Stelle möchte ich mich bei allen bedanken, die das Gelingen dieser Arbeit ermöglicht haben:

- Mein erster Dank gilt meinem Betreuer Selim Jochim. Er hat mich vor drei Jahren in seine noch junge Gruppe, die zu diesem Zeitpunkt nur aus Friedhelm und ihm selbst bestand, aufgenommen und mir damit die Möglichkeit gegeben, zu der Entstehung eines neuen Experimentes beizutragen. Seine Erfahrung und unermüdliche Unterstützung haben wesentlich zum rapiden Fortschritt des Projektes beigetragen. Wann immer wir nicht weiter wussten, war Selim zur Stelle und das Problem war meist in wenigen Minuten gelöst. Auch wenn mal wieder was komplett schief ging, verlor er nicht die Geduld, sondern half das Missgeschick zu beheben. Er hat immer ein offenes Ohr für die Sorgen seiner Gruppe, auch wenn es um nichtphysikalische Dinge geht, und tut alles, um die Arbeitsatmosphäre so angenehm wie möglich zu gestalten. Dazu tragen natürlich auch die Gruppentreffen bei ihm zu Hause bei. Danke für das Vertrauen, das du uns entgegenbringst!

- Besonderer Dank gilt auch allen Mitgliedern unserer Gruppe: Friedhelm, Thomas, Matthias, Andre und Gerhard, vielen Dank für die schöne Zeit, die ich, nicht nur im Labor, mit euch verbringen durfte. Ohne euren Einsatz wäre alles, was wir in den letzten drei Jahren auf die Beine gestellt haben, nicht möglich gewesen.

  Matthias hat uns leider nach der Diplomarbeit verlassen, um nach London zu gehen und dort mit der Promotion zu beginnen. Ich hoffe, du hast dort jede Menge Spass und wünsche dir weiterhin viel Erfolg bei deiner Arbeit.

  Den neuen Mitgliedern unserer Gruppe, Martin und Philipp, wünsche ich viel Spass und gutes Gelingen für die Diplomarbeit. Ihr habt euch für die richtige Gruppe entschieden!

  Kirsten, die gerade für drei Monate bei uns zu Besuch ist, wünsche ich alles Gute für die Zukunft. Sei nicht traurig, dass wir keine blaue Falle in unser neues Experiment einbauen wollen ;-).

- Julia und Friedhelm möchte ich an dieser Stelle nochmals ganz herzlich zur Geburt ihres Sohnes Laurin Leander gratulieren. Alles, alles Gute!

- Ich danke allen, die diese Arbeit Korrektur gelesen haben!

- Danke an alle Mitglieder der Gruppe Ullrich, nicht nur für die Bereitschaft Labor-Equipment bereitzustellen, sondern auch für die vielen spannenden Tischkickerpartien, die wesentlich zur guten Stimmung beigetragen haben.
- Helga Krieger danke ich im Namen der gesamten Gruppe für ihre Hilfe in vielerlei, nicht nur technischen, Dingen.
- Den feinmechanischen Werkstätten, insbesondere Herrn Mallinger von der Hauptwerkstatt, sowie Herrn Flicker und Herrn Säubert von der Ausbildungswerkstatt, danke ich für die kooperative Zusammenarbeit und die stets hohe Qualität der angefertigen Werkstücke.
- Vielen Dank an die Gruppe von Matthias Weidemüller für die Bereitstellung ihres Lasers, mit dem die Experimente zur Mikrofalle durchgeführt wurden.
- Eric Braaten, Hans-Werner Hammer, Chris Greene, Stefan Flörchinger, Richard Schmidt und Sergej Moroz danke ich für die vielen ergiebigen Gespräche und Diskussionen.
- Besonderer Dank gilt meinen Eltern. Ihr habt mir alles ermöglicht und mich immer in meinen Entscheidungen unterstützt. Vielen, vielen Dank!